Permanent magnet bearing for axial rotor load compensation

Maxence Van Beneden

Ingénieur civil électromécanicien

Ph.D. thesis

6th September 2019

Examining committee

Prof.	T. Pardoen	UCLouvain - iMMC	*Chairman*
Prof.	B. Dehez	UCLouvain - iMMC	*Supervisor*
Prof.	F. Gillon	Centralelille - L2ep	
Prof.	J-P Yonnet	Grenoble - G2ELAB	
Dr.	V. Kluyskens	UCLouvain - iMMC	
Ir.	J. Bou Saada	ALSTOM	

Remerciements

Premièrement, je remercie mon promoteur Bruno Dehez qui a été un moteur et un guide.

Je tiens à adresser un merci particulier à Virginie Kluyskens qui a été un soutien constant tout au long de mon doctorat. Un énorme merci également pour toutes les relectures attentives.

Je désire également témoigner toute ma reconnaissance à Virginie Kluyskens et Johnny Bou Saada ainsi qu'aux Professeurs Thomas Pardoen, Bruno Dehez, Frédéric Gillon et Jean-Paul Yonnet pour l'intérêt qu'ils ont témoigné à ce travail en acceptant de faire partie du jury.

Je souhaite remercier les membres du consortium ECOPTINE pour leurs échanges constructifs lors des réunions qui ont permis d'enrichir le contenu de cette thèse.

Je tiens également à remercier tous les membres du pôle MEED qui rendent l'ambiance au travail très agréable.

Un grand merci à l'équipe technique de la plate-forme CREDEM et tout particulièrement à Axel Jottard pour ses conseils lors de la réalisation de mes pièces. Merci également à Alex Bertholet de la plate-forme LEMSC pour l'aide technique sur les capteurs de force.

Je tiens aussi à remercier Astrid et Catherine pour l'aide concernant les questions administratives mais encore plus pour le temps qu'elles m'ont consacré.

Pour terminer, je tiens à remercier chaleureusement ma famille et mes proches pour leur soutien et leurs encouragements.

Abstract

Magnetic bearings present the advantage to be contactless guiding devices. Most of current magnetic bearings are actively controlled. They reach high stiffness but are only stabilized at the expense of complex control systems. In opposition, permanent magnet (PM) bearings are simple but in accordance with Earnshaw theorem, levitation using only PM is impossible. As a result, at least one degree of freedom has to be stabilized by other means e.g. mechanical bearing. A significant characteristic of bearings is the guiding stiffness. Combining PM bearings with mechanical bearings enables a solution where the PM thrust bearing (PMTB) is only used to carry the load of the system, and the mechanical bearings are used to ensure the guiding function. This allows a high increase in the life time of the global system and a decrease of the losses. This combination is particularly a good solution to guide and carry high axially loaded rotors as in hydroelectric turbine, vertical axes wind turbine or flywheel system.

In this context, this thesis concerns the implementation of permanent magnet bearing for axial rotor load compensation in practical applications. To this end, this work proposes at first to compare different topologies of PMTB. The latter are made of PM rings axially or radially polarized and axially or radially stacked including classical polarization structure as well as Halbach array. In addition, ferromagnetic material is considered to increase the PMTB performances leading in two additional groups so-called back-iron and induced pole structures. The comparison highlights that Halbach array is a better solution in terms of force density than classical polarization when no-iron is considered. However, for classical polarization topology, the back-iron structure allows to equal or even outperform the Halbach array.

Then, the different possible PM materials that compose the PMTB are compared. The comparison is based (i) on the temperature stability of the PM and (ii) on its ability to withstand irreversible demagnetization effect. To this end, a finite element model that takes into account temperature and demagnetization effect is developed and experimentally validated. Then the behaviour of classical magnet (ferrite and alnico) as well as rare-earth magnet (neodymium and samarium) are studied. It is first highlighted that the samarium magnet is the most stable with temperature variation. In addition, the results also show that the maximum temperature recommended by PM manufacturer is not sufficient for safe design in applications with temperature variation. Designers need a more complete model as the one developed here. Secondly, irreversible demagnetization risk is predicted based on dimensionless quantities. The results show either that a PM material can be chosen judiciously according to temperature and selected topology, or that a given PM material can have an impact on the selection of the best topology.

Next, the PM properties can be degraded due to temperature variation or aging resulting in a decrease of the magnetic force. Therefore, the system lifetime as well as its efficiency is reduced. In order to solve this problem, a passive compensation system maintaining a constant magnetic force is developed. It is based on pressurized jack placed in series with the static part of the PMTB. Ideally, the pressure inside the jack remains constant and thus, the magnetic force. In practice, the jack can be implemented by pressurized bellows connected to an external fluid tank. This solution also allows to adapt the magnetic force by the choice of the pressure. However, this practical solution has a non-zero equivalent stiffness which impact badly the compensation solution. A design rule shows that if this stiffness is at least 10 times smaller than the magnetic stiffness, the compensation is correctly achieved.

Finally, two PMTB working as axial load relievers are implemented in the context of a flywheel energy storage system: one is linked to the electrical machine and the other to the flywheel itself. The selected topology is composed of radially stacked PM rings with axial polarization and back-iron as this solution offers good magnetic performances and ease for assembly. The temperature compensation solution is implemented for the PMTB associated to the flywheel. The experimental characterizations show very good correspondence with the intended performances.

Funding

The work presented into this thesis has been done in the context of the research project ECOPTINE (Logistics in Wallonia - Convention № 6977) funded by the "région wallonne".

The aim of the project is to develop a "low speed flywheel energy storage system" for an off-board railway application. The system gives the possibility to improve the energy recovered during the braking of railway vehicles and to reduce power peaks during acceleration and deceleration of trains. The energy available during the regenerative braking is stored into the low-speed flywheel. The combination of mechanical bearings and permanent magnet bearings is used and implemented in order to guide and carry the rotor.

Contents

Introduction

Context and motivation

General context

Nowadays electric energy storage (EES) has shown remarkable growth worldwide. Their interests are various and can be applied to many applications. They are defined as the process of converting electrical energy into a form that can be stored and reconverted into electrical energy when needed [1]. The ESS technologies are very divers and can be classified based on the nature of the storage system [2, 3] as shown in Fig. 1.

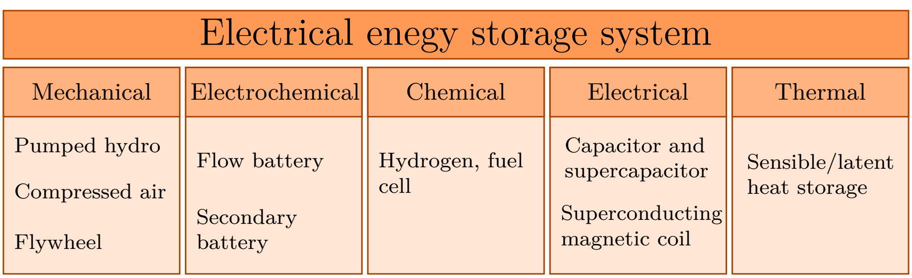

Figure 1: Classification of EES system by the form of stored energy [4, 5].

Each technology has its own benefits and drawbacks. A first comparison can be based on the energy density versus the power density and is typically represented in Ragone plots [6]. Some example of technologies are given in Fig. 2. In addition, the Ragone plot allows to highlight the charging/discharging time of the device. For instance, the fuel cells charging/discharging time is very high ($\approx 10h$), in comparison of the one of capacitors ($< 10s$).

This Ragone plot is used to compare EES but it is not comprehensive for a complete comparison. Other aspects like the operating cost, the investment cost and the potential economic benefit need also to be considered [8]. Actually for each application, an analyse of the storage technologies need to be performed in order to find the most suitable solution [9]. This analyse takes into consideration aspects like the lifetime, the self-discharge, the security issues or the impacts of

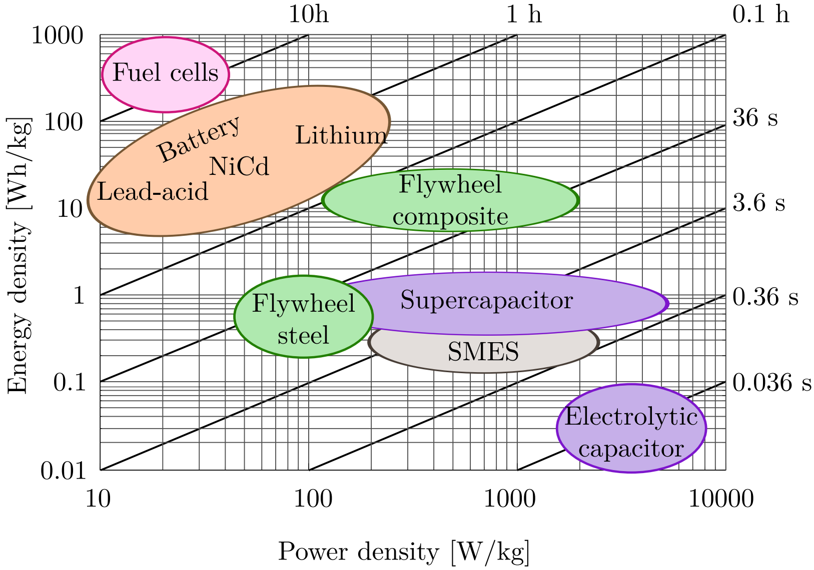

Figure 2: Ragone plot: Power density versus energy density of EES [4, 7].

the installation on the environment [2].

Consequently, EES system needs to be studied in parallel of their intended application. In the literature, authors compare and classify existing and promising uses of EES for a better electrical energy management [2, 4, 7, 10]. For the example, the classification proposed by Steeley [11] in Fig. 3 gives different applications in function of the power rating and the energy discharge time. As observed, these two characteristics can vary drastically depending on the application.

By comparing the EES technologies of Fig. 2 and the application requirements of Fig. 3, it appears clearly that the EES solution is dependent on the intended application.

Specific context of the project

This work was financed by the Walloon Region as part of the ECOPTINE project (adding Energy aCcumulation to OPtimize electrical Traction INfrastructure Efficiency). The context of this project is to reduce the electrical consumption of the railway network by recovering the energy of train braking and to store it in an EES system. The chosen technology is a low-speed flywheel energy storage system (FESS). This results in two main improvements.

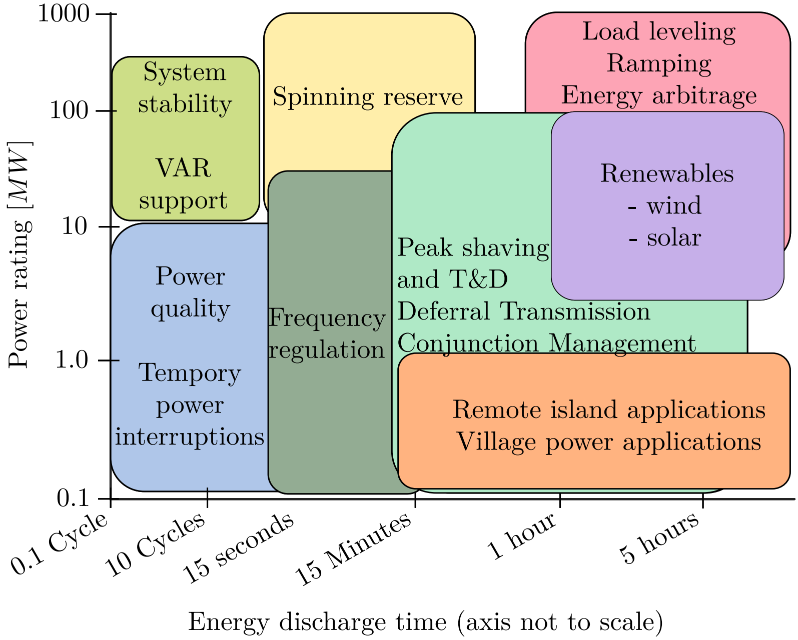

Figure 3: Overview of energy storage use cases [11].

A first improvement is done by saving energy from train braking and this principle is shown in Fig. 4.

In Fig. 4.a, the energy for the train acceleration is taken form the electrical grid. During the braking phase, two types can be used: mechanical (friction) braking and electrical (dynamic) braking [10]. The electrical energy generated during the electrical braking can either be regenerative and used by an other train, or be dissipated in resistors (rheostatic braking) as represented in Fig. 4.b. In most cases the electrical grid is not able to recover these electrical energy peaks because peaks are difficult to manage or because the sub-stations are not reversible.

In Belgium, the 42% of the energy absorbed by a train is consumed during the braking phase. 27% profits already of the regenerative braking and is used by other train. Nevertheless, 15% is still consumed in rheostat or in friction. In order to recover this energy, the latter could be stored in an FESS as shown in Fig. 4.c and used by the same train or an other train latter as shown in Fig. 4.d.

A second improvement is to limit power peaks absorbed by the railway network on the main grid. Indeed due to train acceleration and deceleration, the railway network is subject to unpredictable huge power peaks [12] as shown in Fig. 5.a. The latter correspond to a quite low energy quantity but are charged at very high price because exceed a reference power. Again, the use of EES systems can solve this problem with a good management of the railway network consumption as shown in Fig. 5.b for an ideal case.

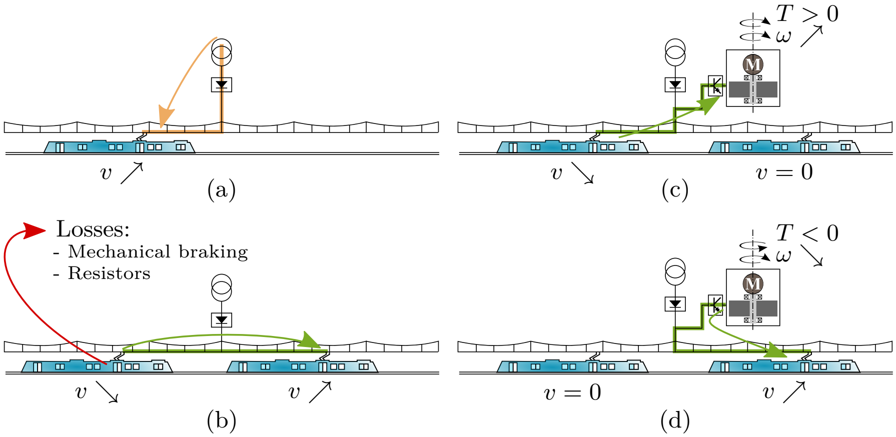

Figure 4: Principle of regenerative braking. In (a) conventional starting with energy given by the railway grid. In (b), regenerative braking possible only if another train start on the same line, otherwise the energy is consumed in resistors or by friction. In (c) and (d) regenerative braking saved and stored in the FESS.

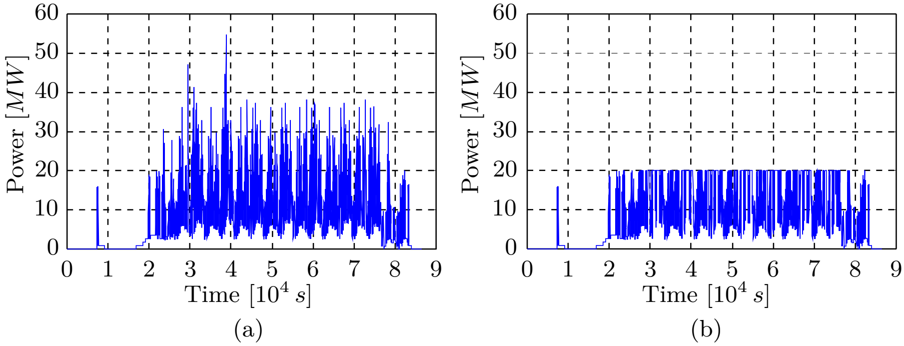

Figure 5: Peak shaving principle from [12]. (a) The normal consumption ; (b) Peak power elimination by means of installing energy storage units in ideal situation.

Additional use of the FESS in the Belgian rail network could be to stabilize the voltage level in remote area. Indeed, the Belgian railway grid is star-shaped with substation in the center. When too much trains absorb/regenerate electrical energy on the same line, the voltage level drops/increases leading to the disconnection of some trains for safety reasons. The obvious solution is to place substation at the end or in the middle of the line, nevertheless, it is an expensive solution in comparison of installing a FESS. This principle is shown in Fig. 6. In Fig. 6.a, too much current is absorbed from the same sub-station leading to a diminution of the catenary voltage. This diminution can be caused by too many trains accelerating on the same line and/or due to too large train to sub-station distance. In the worst case, trains can be disconnected from the catenary for security reason. Installing a FESS closed to the problem, allows to stabilize the catenary voltage as shown in Fig 6.b.

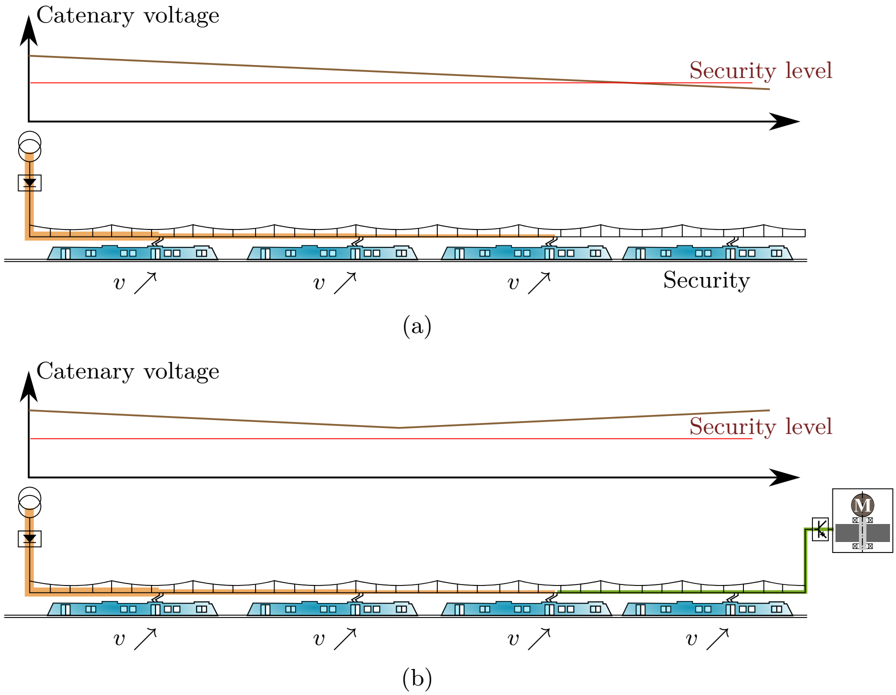

Figure 6: Principle of catenary voltage drop. In (a), too much current is absorbed on the catenary and caused voltage drop that can perturb the railway traffic. In (b), the FESS stabilizes the voltage level.

The FESS specifications developed for the ECOPTINE project are:

- to store an electrical energy of 25 kWh,
- for a maximal power of 3 MW,
- with a typical cycle of 30 s of charge, 5 min of storage and 30 s of discharge.

For safety, technical and commercial reasons, the speed range is between 2000 RPM and 4000 RPM corresponding to a moment of inertia of 1370 $kg\,m^2$. From these specifications and by comparing with the Ragone plots of Fig. 2, it is evident that low speed FESS is well suited for this particular application. The weight of the rotor is 52 kN.

In order to compare these values, in [13], a FESS was designed for the Spanish railway network. The objective was to save waste of regenerative braking energy that can can vary between 8% to 25% of the total consumption. Authors suggested to use a 55 kWh / 350 kW FESS with a maximum rotational speed of 6000 RPM and a moment of inertia of 895 $kg\,m^2$.

Objective of the project

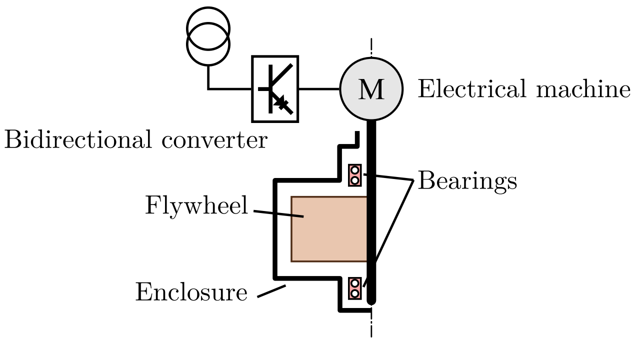

Figure 7: The different components of a FESS.

A FESS is composed of a rotating mass (the flywheel), bearings, an enclosure, an electrical machine and a bidirectional converters as shown in Fig 7. Flywheels can be classified into two groups which depends on the rotor speed: low and high speed flywheel system [14–16]. Table 1 gives a comparison of these two technologies [17].

Table 1: Comparison of low speed and high speed FESS [17].

	Low speed	High speed
Flywheel material	Steel	Composite materials
Electrical machine	Asynchronous, permanent magnet synchronous or reluctance machines	Permanent magnet synchronous or reluctance machines
Confinement atmosphere	Partial vacuum or light gas	Absolute vacuum
Enclosure weight	$2\times$ Flywheel weight	$\frac{1}{2}\times$ Flywheel weight
Bearings	Mechanical or mixed (Mechanical and magnetic)	Magnetic
Relative Price	1	2

In [18], Genta emphasizes three critical points in the design of FESS: the high mass of the rotor, the high aerodynamic drag and the high bearing drag. The aerodynamic drag can be reduced by placing the rotating part in a vacuum enclosure [17]. Additionally, the enclosure has to withstand the flywheel break and ensure the security. Genta asserts that magnetic bearings are a good solution in order to support the rotating mass and to reduce the magnetic bearing drag. He lists the different kind of bearing combinations:

- full 5-axis active suspensions,
- passive suspensions with at least one active axis,
- superconducting passive suspension,
- full passive suspensions stabilized by gyroscopic effect (Levitronstyle),
- electrodynamic passive suspensions,
- magnetic/mechanical hybrid suspensions.

Full active magnetic suspension can be considered as the most suitable system as it can generate both high stiffness and high damping. Another advantage of a controllable active solution is that it is possible to improve the self balancing and therefore to cross critical speeds thanks to the control system. However, it could reach a higher cost than can be accepted for an industrial application. This cost is explained by the addition of sensors, controller and power electronic system. Moreover in case of emergency events, a backup system like back-up bearing has to be installed increasing both price and mass.

Full passive solutions has the main advantage of low cost but generate low stiffness and damping making them stable only in some speed range and/or special conditions. One solution to have a full passive suspension is to use superconducting but even high temperature superconductors need heavy cooling system which increases the price.

A passive solution only based on permanent magnet (PM) can not be stable. Indeed in respect of the law developed by Earnshaw [19] and Braunbek [20, 21], the sum of the stiffness in all direction (K_r or K_z) is equal to zero if there is only PM material, and smaller than zero if there is ferromagnetic material:

$$\begin{aligned} K_z + 2K_r &= 0 \quad \text{for only PM material,} \\ K_z + 2K_r &< 0 \quad \text{for PM and ferromagnetic material.} \end{aligned} \tag{1}$$

This means that the stiffness is negative at least in one direction and the rotor cannot be supported stably. Therefore, at least one direction needs to be stabilized by another mean.

An interesting solution for axially loaded applications consists in combining mechanical bearings with a permanent magnet thrust bearing (PMTB). In that case, the PMTB acts as a load reliever for the mechanical bearings and the guidance system is ensured by the mechanical bearings only. Indeed, the stiffness related to the mechanical bearings is at least of an order of magnitude larger than the equivalent magnetic stiffness and therefore, the impact of PMTB on the stabilization can be neglected. As the PMTB is not used for its "stabilizing" behaviour but as a constant compensation, it should no longer be called "permanent magnet thrust bearing" but "permanent magnet load reliever". Nevertheless for convenience, the term "PMTB" is used during this thesis.

Whit this combination, there is still the drawbacks of traditional mechanical bearing like lubrication and bearing drag, however, the advantages are low cost and simple design. Technically, the improvements on the system are:

- an increase of the lifetime,
- a reduction of the total losses.

From mechanical bearing manufacturers [22, 23] and from the literature [24], technical informations on mechanical bearings can be found. The lifetime of mechanical bearings is evaluated by the basic rating life L_h. The latter is the life reached or exceeded by 90% of a sufficiently large group of apparently identical bearings before the first evidence of material fatigue develops and is expressed in number of operating hours:

$$L_h = \frac{10^6}{60n}\left(\frac{C}{P}\right)^p \tag{2}$$

with n the rotation speed, C the basic dynamic load rating, P the equivalent dynamic bearing load and p the life exponent with $p = 3$ for ball bearing and $p = 10/3$ for roller bearing. In the case of high axially loaded application, the basic dynamic load rating P corresponds to the high axial force. Relieving the axial load support by the bearings leads to a high increase of the lifetime. From (2), it can be supposed that a complete relieving of the load lead to an infinite lifetime. However for good operation, a pre-load needs to be maintained on the mechanical bearing to allow good rolling without slipping condition and thus, avoid premature wear.

The principle of relieving axial load on mechanical bearing by the action of magnetic force was already studied in the literature. In 1958, Nakata et al. proposed first to combine PMTB with mechanical bearing for hydropower application. Author main concern is to increase the lifetime of the system. Indeed, bearing failure is one of the principle causes of breakage in rotating machinery [25] and such failures can be catastrophic. It has been proved [26] that the lifetime limitation in hydro turbine are mainly due to mechanical bearing breakage and more precisely due to the thrust bearing. It can result in costly downtime with heavy failure analyses [27] and / or reparation [28] which can last more than a month. In hydropower plant, most of thrust bearings are made of fluid-film bearings [29] and, according to Ferguson et al., these bearings need new development in order to increase their performance and lifetime.

One solution is to support the axial load by means of magnetic force. In [30], authors proposed to add to the mechanical bearing, an axial active magnetic bearing. The latter adapts the magnetic force depending on the operating load and thus, compensates the axial force supported by the mechanical bearing. In [31] authors proposed to add a PMTB in order to carry a part of the constant axial load. The combination of magnetic and mechanical bearings reduces the thrust force in the mechanical bearing of about 20% of the total load and therefore, declines the frictional losses and reduces the failure rate.

In [32], Pérez-Loya et al. combine mechanical bearings with PMTB for an hydro turbine in order to increase the lifetime of the global system by relieving the axial load. They also demonstrate by experiment that the total losses are reduced during a spin-down test.

In [33], Kumbernuss et al. combine a PMTB with mechanical bearing for vertical axis wind turbines. Authors assert that this solution is cheaper than active magnetic bearings and high temperature superconductor bearings but has lower performance. However, the price is an important factor in making vertical axis wind turbines more attractive. In [34], Premkumar et al. also develop a PMTB combined with mechanical bearings for a small vertical axis wind turbine. They experimentally measure that the speed of the wind turbine increases by three to four times by using the PMTB than mechanical bearing alone. Beside, the time required to get zero RPM with a sudden disappearance of the wind is increased thanks to PMTB.

For the FESS designed for the Spanish railway network, [13] conventional ceramic bearings have been used but since the weight and speed level are too high for existing commercial bearings, a PMTB was used to relieve the high axial load.

For the ECOPTINE project, the chosen system is a combination of PMTB working as load reliever and ball bearings in charge of the guidance system. The aim of this thesis is to study permanent magnet load reliever specially designed for high axially loaded applications like in low speed flywheel system. The flywheel designed for the ECOPTINE project is composed of a vacuum enclosure, a rotating mass, ball bearings, a PMTB, seals and is shown in Fig 8. The electrical machine is placed outside the enclosure and has its own PMTB. A 3D view of the FESS is given in Fig. 9.

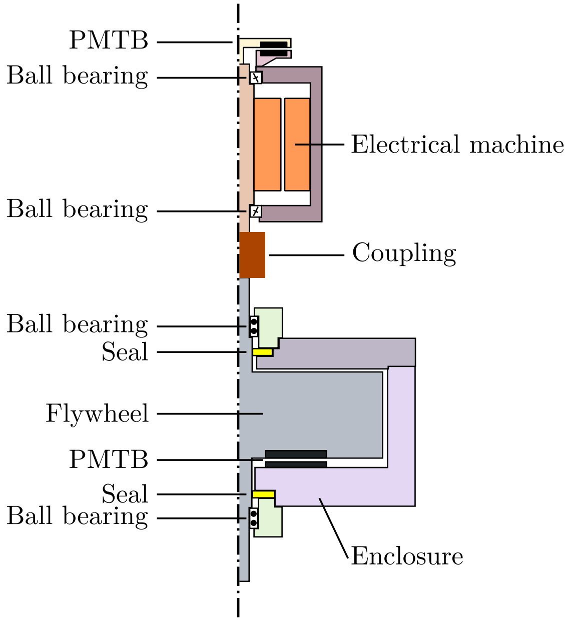

Figure 8: Component of the FESS developed during the ECOPTINE project.

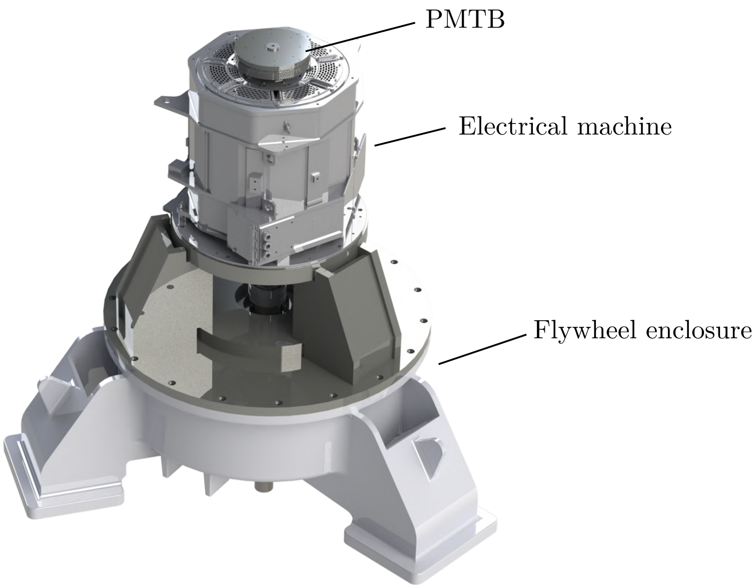

Figure 9: 3D view of the FESS developed during the ECOPTINE project.

Manuscript content and organization

This thesis concerns permanent magnet thrust bearing working as load reliever. The aim is to give some keys to designers in order to incorporate PMTB in practical device. First, the topologies of PMTB are compared based on the minimal amount of permanent magnet needed to generate a given axial force. Based on this comparison, the selection of PMTB for a given application is eased. Additionally, design formula for a fast sizing of optimal PMTB are given. Secondly, the permanent magnet material used in the realization of PMTB are compared. The latter can be subject to demagnetization or temperature effect that can dramatically decrease performance of the PMTB. A systematic approach is presented in order to evaluate this risk and to help designer in the selection of the material in function of the application but also in function of the selected topology. Thirdly, an novel passive compensation solution for load relieving application is introduced. The aim of this design is to passively compensate the negative effect of temperature variations on the PM properties which decrease the PMTB performance. This is done by placing in series with the static part of the PMTB a pneumatic jack. By this means, the magnetic force is maintained (quasi-)constant at the condition of having a constant pressure in the jack. Finally, two PMTB working as load reliever are designed for the particular case of the ECOPTINE project. One PMTB is designed for the flywheel and the other one for the electrical machine.

Specifically, this thesis aims to answer the following questions.

- How to objectively compare different PMTB topologies for axial rotor load compensation ?
- How to evaluate by a fast procedure, the optimal dimensions of PMTB ?
- How to predict the risk of irreversible demagnetization and what can be its impact on topologies ?
- How to compensate the negative impact of temperature and aging effects on the PMTB ?

The manuscript is organized in 4 chapters. Each chapter begins with a state of the art related to its own topics and finishes with a small conclusion.

Chapter 1 deals with the comparison of permanent magnet thrust bearing (PMTB) topology. A first section presents a state of the art in topology classification and comparison. It highlights that PMTB can be parametrized based on dimensionless quantities. Based on this principle, the next section introduces scaling laws able to size ideal PMTB. Afterwards, correction functions are presented. The latter adapts the PMTB dimensions in order to take into account the non-idealities. A next section gives an example of the use of the scaling laws and corrections function for purposes of design optimal and realisable PMTB. Finally based on the derived scaling laws, the topologies are compared based on the minimal amount of permanent magnet volume required to generate a given axial load.

Chapter 2 compares the different permanent magnet (PM) material that can be used in PMTB. A first section lists the main PM materials with their principal advantages and disadvantages. A state of the art shows the PM characteristics and behaviours for PMTB applications. It is highlighted that the PM material can have a large impact on the PMTB performance. The main critical points are the demagnetization risk and the temperature effect. The second section introduces a model able to take into consideration the demagnetization risk and the temperature effect. In the third section, the impact of PM material is discussed. First the temperature effect and its impact on the PMTB performance are given. Then, the risk of irreversible demagnetization effect is studied and the impact of the selected topologies as well as the operating temperature is considered.

Chapter 3 presents a passive compensation solution for load relieving application subject to magnetic force variation due to temperature effect. This problematic is introduced in a first section and then, a state of the art presents the other solutions developed in the literature. The proposed solution is described in the next section. It is based on placing a pressurized jack in series with the static part of the PMTB. Finally its impact on the magnetic force is discussed and some indications for good design of this pressurized jack are given.

Chapter 4 presents practical implementations of PMTB. A first section introduces the difficulties and solutions in the design, the assembly and the characterization of PMTB. Based on these observations, two PMTB are designed: one for the flywheel and one for the electrical machine that drives the latter. The passive compensation solution is implemented for the flywheel PMTB.

Topology comparison 1

This chapter presents different topologies of permanent magnet thrust bearing (PMTB). The topologies are optimized separately with the aim of minimizing the permanent magnet (PM) volume used to generate a given axial force. Based on this optimization, the topologies of PMTB are compared.

The first section introduces the state of the art in the field of comparison and classification of permanent magnet bearing (PMB). Then, the topologies are characterized and scaling laws for fast sizing ideal PMTB are derived. The next section, introduced correction functions in order to take into account practical limitations. Then, an example of sizing procedure is given. Finally, based on the scaling lows, the PMTB topologies are compared.

1.1 State of the art

In the literature different authors have classified and compared permanent magnet bearings (PMB). Most of the papers deal with generating high radial stiffness. The focus of this thesis is on the optimization and the comparison of thrust bearing acting as load reliever i.e. on the axial force generation. Nevertheless, the classification and the comparison follows similar procedure. The aim of this section is first, to introduce the different topologies existing in the literature and secondly, to present the criteria of optimization and classification of PMB's.

In 1981 [35], Yonnet introduced 10 basic arrangements of radial magnetic bearings and 10 arrangements of axial bearings. Each arrangement is only composed of two PM rings which can be axially or radially polarized. Authors classify the PMB into two groups [36]: the centering bearings (Fig. 1.1.a) and the thrust bearings (Fig. 1.1.b).

In 1995, Yonnet et al. have shown that pile-up PM rings increases the stiffness more than the PM volume increases [37]. In addition, authors proposed to pile-up PM rings such as to create a "rotating magnetization direction" (RMD) structure i.e. the direction of magnetization varies with 90 degree steps, from axial to radial and so on. Yonnet et al. showed that for the same PM volume,

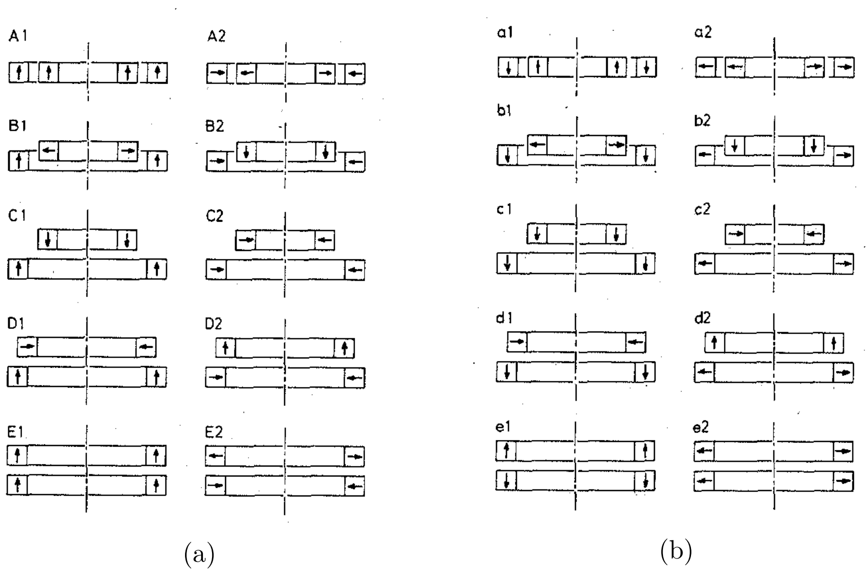

Figure 1.1: The 20 arrangements of radial (a) and axial (b) bearings proposed by Yonnet [35].

the RMD structure generates more stiffness than the axial polarization structure. These two stacks of PM rings are represented in Fig 1.2

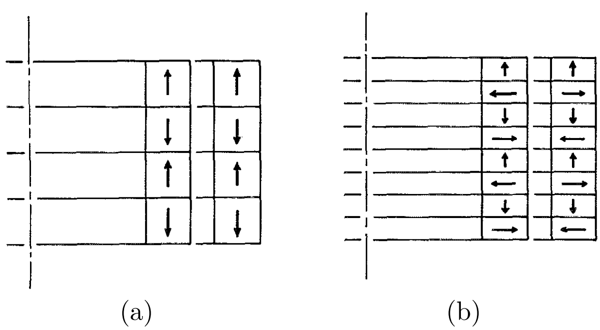

Figure 1.2: Stack of PM rings proposed by Yonnet [37] to form (a) the conventional PMB and (b) the RMD structure.

Actually, the RMD structure is a particular implementation of the ideal Halbach array [38, 39]. As shown in Fig. 1.3.c, the ideal Halbach array is a continuous rotating magnetization [40]. The latter is an arrangement of PM that increases the magnetic field on one side of the PM and cancels the magnetic field on the other side. This ideal Halbach structure can be approximated by the quasi-Halbach array composed of PM segments with different polarization directions as shown in Fig. 1.3.a and b.

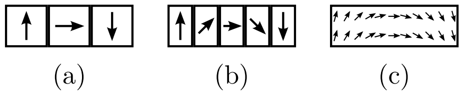

Figure 1.3: Two quasi-Halbach array (a) and (b) and one ideal Halbach array (c).

In 2003, Paden et al. performed optimization of stacked PMB to maximize the radial stiffness in a limited bearing volume [41]. Authors derived a set of design formulas to estimate the parameters of the conventional stacked PMB's i.e. axial stack with radial polarization and axial stack with axial polarization. These equations allows a fast design of PMB in a controlled volume with high radial stiffness. Authors also proposed formulas to obtain rapidly the corresponding axial force and axial stiffness. They suggested to stabilize the negative axial stiffness with the help of an active magnetic bearing. The latter can be easily sized based on these formulas.

In 2006, Moser et al. have developed same kind of formula [42] for topology with axial stack and axial polarization. Furthermore, they proposed a miniature low-friction bearing based on the design procedure. The bearing is represented in Fig. 1.4. It is composed of rotor and stator magnet arrays working as PM centering bearing. The problem of axial instability due to negative axial stiffness is solved by the combination of a small axial offset (spacers in Fig. 1.4) and a ruby single-ball thrust bearing. The axial offset generates an axial force proportional to this offset. The thrust bearing is composed of a jewel ball pressed against its jewel endstone. The global system forms a very low friction bearing with PM dimensions reaching very thin thicknesses. Authors investigated practical solution for the production of thin PM rings by the use of a special cutting process: cut by electric discharge machining. This technique allows to reach very thin layers of PM rings without losing its magnetization.

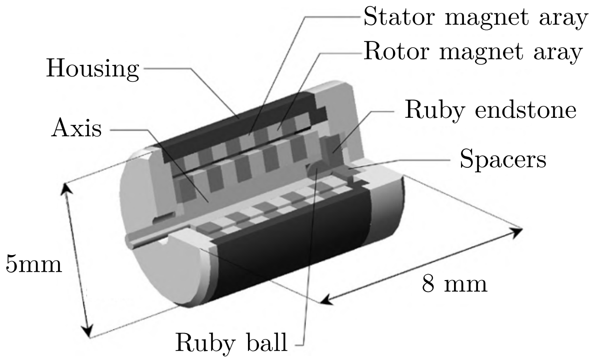

Figure 1.4: Miniature low friction bearing proposed by Moser et al. [42].

Bekinal et al. have extended the same kind of design formulas to other PMB topologies like the Halbach structure [43, 44] as well as for thrust bearings [45].

In 2011, Yoo et al. proposed to add a non magnetic gap between the PM rings in the topology with the axial stack and the axial polarization [46] as shown in Fig. 1.5.a. They compare the performance of this new device with the Halbach structure (see Fig 1.5.b) to generate the higher axial force. They show that the axial force is dependant on the axial offset Δz between the rotor and the stator and reaches a maximum value for a given offset. The optimisation was performed to find the number of PM superposition N, the height of the PM h, the gap between the PM ζ and the axial offset Δz that minimized the PM volume V with the constraint to carry the axial load $F_z \geq F_{load} = 2700\,N$. Other parameters affect the axial force like the inner and outer diameters of PM rings as well as the airgap thickness. Authors assume that they are fixed due to available PM sizes and other system constrains. The diameters are imposed at $d = 96\,mm$ and $D = 136\,mm$ for the inner rings and $d = 144\,mm$ and $D = 176\,mm$ for the outer rings leading in an airgap thickness of $g = 4, mm$. The PM material is a N35 grade NdFeB magnet. The results of the optimization are summarized in Table 1.1

Table 1.1: Optimization results performed by Yoo et al. [46].

Parameters	Axial array	Halbach array
$N\,[-]$	3	3
$h\,[mm]$	10.5	7.8
$\zeta\,[mm]$	6.3	–
$\Delta z\,[mm]$	8.3	7.4
$V\,[cm^3]$	2541	1882

They also concluded that even if the non-magnetic spacer increases the performance of the classical topology, the Halbach structure remains better of approximatively 26% on the PM volume. Nevertheless, authors point out that other aspect need to be considered like the cost or the mechanical strength. For this purpose, the non-magnetic spacer can help to increase the rigidity of the bearing.

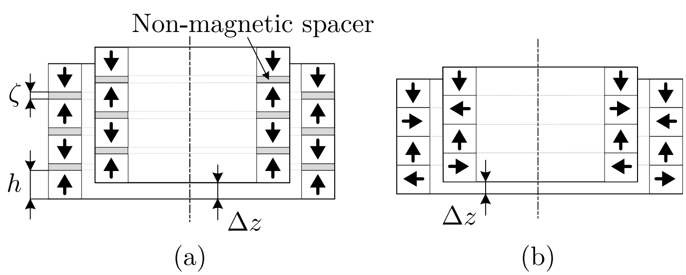

Figure 1.5: Presentation of the axial stacked topologies with (a) non-magnetic spacer between the PM rings and (b) with Halbach array proposed by Yoo et al. [46].

All these design formulas are used to obtain PMB with high axial or radial stiffness in a limited global volume. Their main advantage is to help machine designers to incorporate PMB in mechanical device where conventional ball bearing are classically used. Their interest is clearly limited for applications with high load and without strong limitation on the global volume for the bearing system e.g. in flywheel system.

In order to compare the PMB independently to the global volume dimensions, authors have developed dimensionless quantities to compare PMB on an objective basis.

In [47], Lang et al. compared PMB based on the stiffness-to-volume ratio. They highlight that this ratio can be predict by a dimensionless quantity called the normalized stiffness k^* defined by:

$$k^* = \frac{k\,g^2}{V\,P_m}\ [-] \tag{1.1}$$

with g the airgap thickness (see Fig. 1.6), V the PM volume, k the stiffness and P_m the magnetic pressure defined by:

$$P_m = \frac{B_r^2}{2\mu_0} \tag{1.2}$$

where μ_0 is the vacuum permeability and B_r the magnetic remanence of the PM. They shown that the normalized stiffness depends on the ratio of the the height h and the width w of the PM, and the airgap thickness g:

$$k^*\left(\frac{h}{g}, \frac{w}{g}\right) \tag{1.3}$$

The mean radius R_{mean} of the airgap has an impact on the normalized stiffness but can be neglected for radii greater than the airgap thickness $R_{mean} > g$.

Based on (1.3), the calculation procedure is simplified and allows the representation of the stiffness in a two-dimensional contour-line graph as shown in Fig 1.6 for a double PM rings superposition.

Finally, the same authors evaluated the influence of the number of rings superposition N on the maximum normalized stiffness. The results is summarized in Table 1.2. It is observed that the normalized stiffness converges to a constant value with an increasing number of rings N.

The normalized stiffness formulation have been taken by researchers from the Institute of Electrical Drives and Power Electronics in Johannes Kepler University Linz, Austria [48–50].

In 2012, Marth et al. studied PM centering bearings and compared three axially stacked topologies [48, 49]. The different topologies corresponds to the axial polarization array, the quasi-Halbach array and the ideal Halbach array. The ideal Halbach array can be realized based on special magnetization process [51]. The different topologies are represented in Fig. 1.7 for a number of poles $p = 2$.

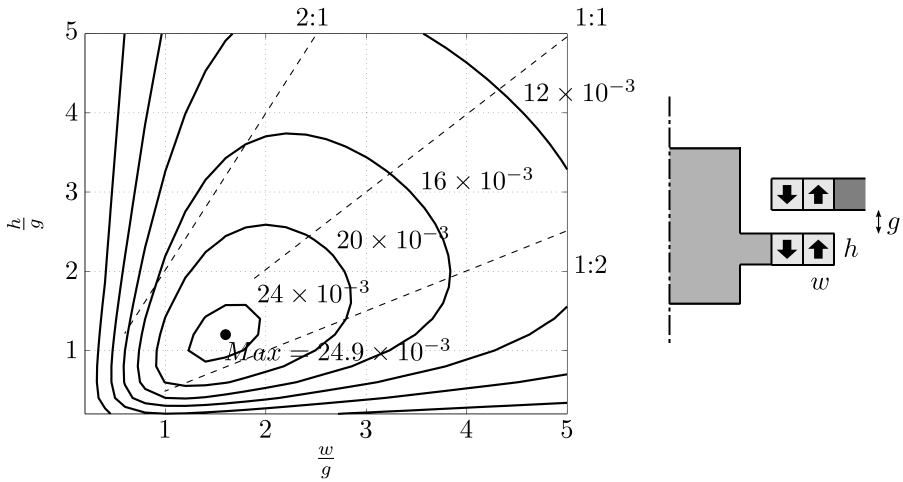

Figure 1.6: Contour line of the normalized radial stiffness k_r^* as a function of the ratio of the PM hight h and width w on the airgap thickness g developed by Lang et al. [47].

Table 1.2: Evolution of the maximum normalized stiffness with the number of rings obtained by Lang et al. [47].

Number of rings N	Normalized hight $\frac{h}{g}$	Normalized width $\frac{w}{g}$	Max(k_r^*) $[- \times 10^{-3}]$
1	1.2	1.2	19.1
2	1.2	1.6	24.9
3	1.2	1.8	25.7
4	1.2	1.8	26.3
5	1.2	1.8	26.7

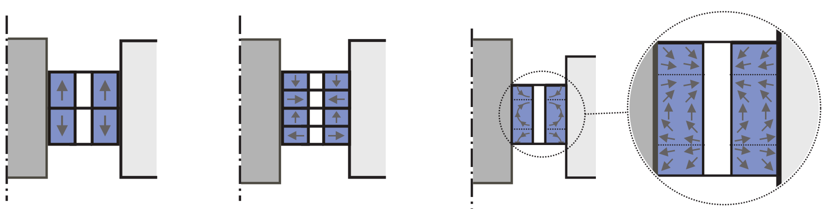

(a) (b) (c)

Figure 1.7: Double-poles repulsive centering bearing with (a) axial polarization array, (b) quasi-Halbach array and (c) ideal Halbach array proposed by Marth et al. [48].

The authors point out that in this configuration i.e. axial stack for centering bearing, the magnetic forces acts mainly in repulsive mode.

In order to compare these three different topologies, Marth et al. calculated the normalized translational stiffness k_x^* based on a planar $x-y$ model. The latter must be divided by two to obtain the radial normalized stiffness of the rotationally symmetric configuration [47, 50]: $k_r^* = \frac{k_x^*}{2}$. The results are summarized in Table 1.3.

Table 1.3: Comparison based on the normalized stiffness k^* of the different topologies of double-poles repulsive centering bearing by Marth et al. [48].

	With axial polarization array	With quasi-Halbach array	With ideal Halbach array
k_x^* from planar model	77.9×10^{-3}	138.4×10^{-3}	172.5×10^{-3}
$k_r^* = \frac{k_x^*}{2}$	38.9×10^{-3}	69.2×10^{-3}	86.3×10^{-3}

Authors also studied the influence on the number of rings in the stack. They prove that the normalized stiffness converges to a constant value for an increasing number of rings N. This result is shown in Fig 1.8 for axially stacked topology with axial polarization, quasi-Halbach array and ideal Halbach array. The result show that for a number of rings larger than 10, the convergence is approximatively reached.

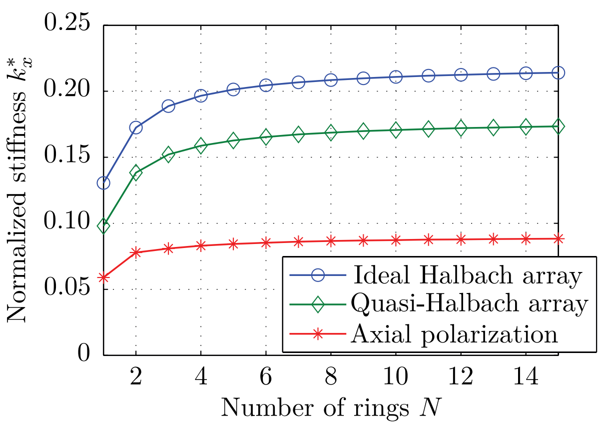

Figure 1.8: Evolution of the translational normalized stiffness with the number of superposed rings obtained by Marth et al.[49].

In 2014, Jungmayr et al. [50] studied the influence of the addition of an iron frame at the back of the PM structures. They compare three topologies of radially stacked centering bearing represented in Fig. 1.9 for a number of poles $p = 2$. The principal magnetic force acting on the PM is an attractive force. The topologies are the classical axial polarization array, the axial polarization array with back-iron and the ideal Halbach array. Based on the normalized stiffness, they compare the three different topologies. The results are summarized in Table 1.4.

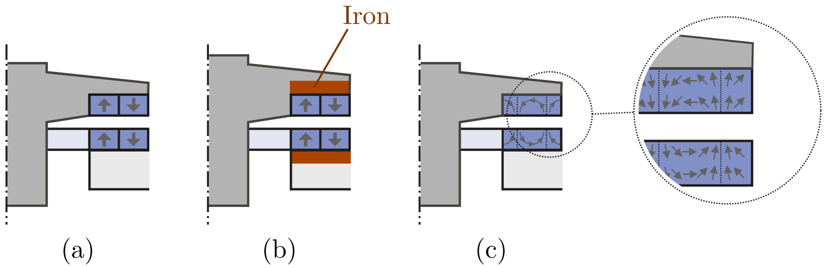

Figure 1.9: Double-poles attractive centering bearing (a) without iron, (b) with back-iron and with an ideal Halbach array (c) [50].

From Table 1.3 and 1.4, the comparison shows that there is a reciprocity between the results of radial (attractive) and axial (repulsive) stacked topologies. Besides, authors established that the ideal Halbach array gives the best results. They also proved that the back-iron increases the performance of classical topology of attractive centering bearing.

Table 1.4: Comparison of the different topologies of double-poles attractive centering bearing based on the normalized radial stiffness k_r^* by Jungmayr et al. [50].

With axial polarization and without iron	With axial polarization and with back-iron	With ideal Halbach array
38.9×10^{-3}	78.5×10^{-3}	86×10^{-3}

Additionally, Jungmayer et al. [50] evaluated the influence of the back-iron on the negative axial stiffness as explained by Earnshaw (1): $\frac{K_z}{K_r} \leq -2$. As shown in Fig. 1.10, the PM dimensions have an impact on the radial stiffness k_r^* and on the ratio of the axial stiffness on the radial stiffness $\frac{k_z^*}{k_r^*}$. Therefore, the choice of PM dimensions could be not only based on the maximization of the radial stiffness but could result from a trade-off between high radial stiffness and stability issue.

Jungmayer et al. also extended the normalized stiffness theory to the normalized force f^* defined by:

$$f^* = \frac{f\,g}{V\,P_m}\ [-] \tag{1.4}$$

As illustrated in Fig. 1.11 for the double-poles attractive centering bearings, the addition of back-iron increases 3.9 times the maximal axial force. Nevertheless at this point, the positive radial stiffness is very low and the negative axial stiffness is comparatively very high.

Safaeian et al. [52] have also used the normalized stiffness k^* in order to compare PMB. They extended the comparison to axially stacked centering and thrust bearing topologies. These topologies include:

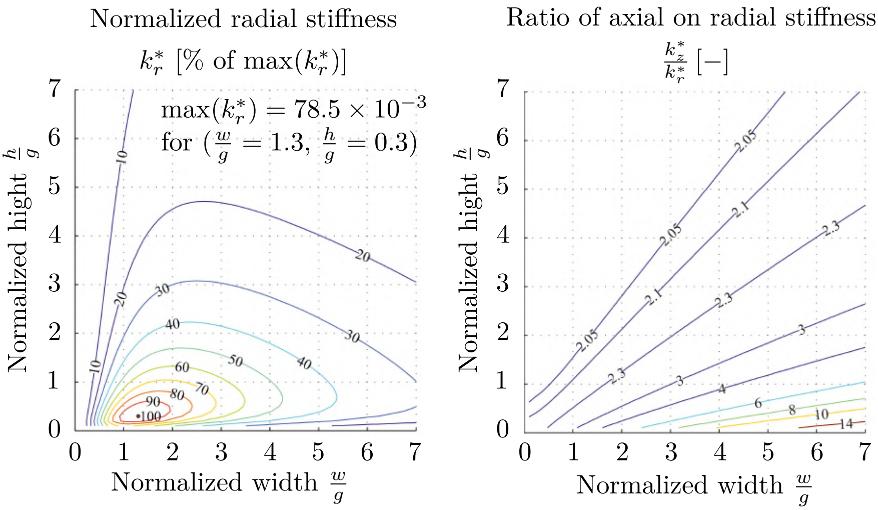

Figure 1.10: Normalized radial stiffness k_r^* in % of max k_r^* in comparison of the ratio of the normalized axial stiffness on the radial stiffness $\frac{k_z^*}{k_r^*}$ developped by Jungmayr et al. [50].

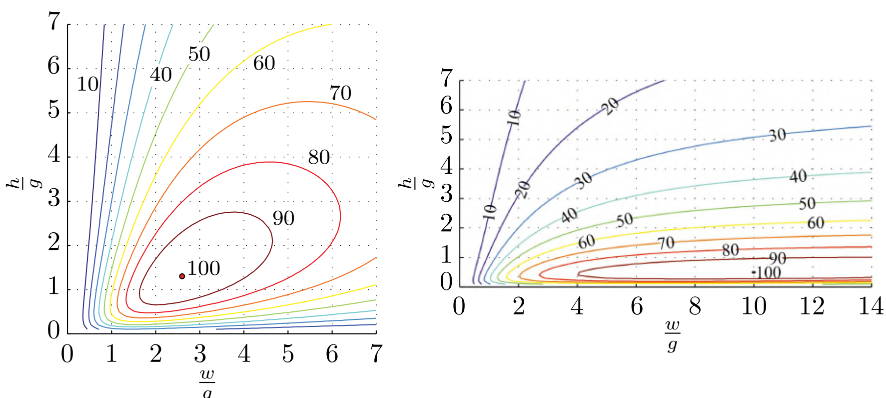

(a) (b)

Figure 1.11: Normalized axial force f_z^* in % of max (f_z^*) for double-poles attractive centering bearing (a) without iron and (b) with back-iron developed by Jungmayr et al. [50]. The maximum normalized axial force is equal to (a) $f_z^*(\frac{w}{g} = 2.6, \frac{h}{g} = 1.3) = 56.8 \times 10^{-3}$. and (b) $f_z^*(\frac{w}{g} = 10, \frac{h}{g} = 0.5) = 221 \times 10^{-3}$.

- the standard axial and radial polarization,
- the quasi-Halbach array,
- the standard polarization with back-iron,
- the standard polarization with iron intervals.

These topologies are shown in Fig 1.12. As observed, a non-magnetic gap between PM superposition is also considered for the quasi-Halbach array, the standard polarization with and without back-iron. They assumed that their analyse can be extended to radially stacked topologies.

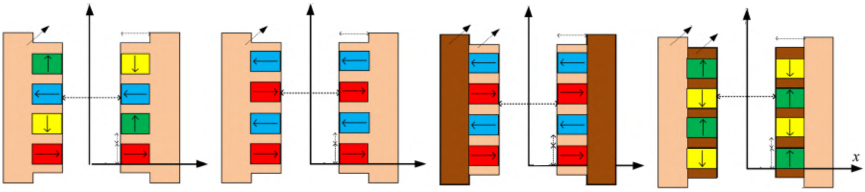

Figure 1.12: Different topologies of axial stacked structure compared by Safaeian et al. [52] with (a) the quasi-Halbach array, (b) the standard polarization, (c) the back-iron structure and (d) the standard axial polarization with iron core intervals.

They proved that the interest of back-iron is also valid for topologies with axial (repulsive) stack.

Besides, the authors have investigated the comparison of topologies for non-optimal PMB. Indeed, as already shown by other authors, the optimal PMB size corresponds generally to PM rings dimensions difficult to realize in practice. It is highlighted that the best topology depends on the PM dimensions. For instance, they compare topology with back-iron and topology with iron-core intervals with the aim of having a positive axial stiffness. Results are shown in Fig. 1.13 and demonstrate that for some dimensions, topology with back-iron is the best but for others, it is the topology with iron core interval.

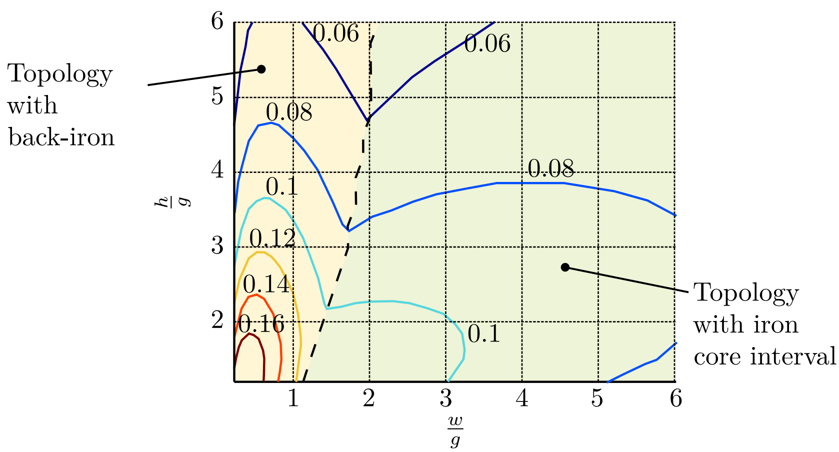

Figure 1.13: Evolution of the normalized axial stiffness k_z^* with the PM dimensions [52].

To conclude the state of the art, we showed that authors have developed different design formulas for a fast sizing of PMB. The latter has also proved that maximizing the stiffness is not the only criterion: stability issues as well as practical PM dimensions need to be considered. All these different characterization have lead to the comparison of different kind on PMB with or without iron. However, the main focus of these comparisons are based on the radial stiffness and their is a lack of comparison based on obtaining a given axial force for a minimum PM volume.

1.2 Topology description and parametrization

Different topologies of PM bearings were studied in the literature and showed in the previous section. In the present work, topologies of PM thrust bearing (PMTB) working as load reliever are compared. That means that the comparison is based on the capability of topologies to generate a given axial force for a minimum PM volume. This section presents the different topologies considered in this work and their parametrization.

1.2.1 Topology description

PM bearings are made of PM rings with axial or radial polarization [53]. It was shown that, for a same PM volume, structure with alternate polarization gives bigger forces than structure with only one polarization [37]. This superposition of PM rings can be axial or radial. Combinations of the axial and radial polarizations are also possible in the same structure, such as to form a perpendicular [54] or a Halbach structure [38, 55]. All these eight topologies are summarized in Fig. 1.14.

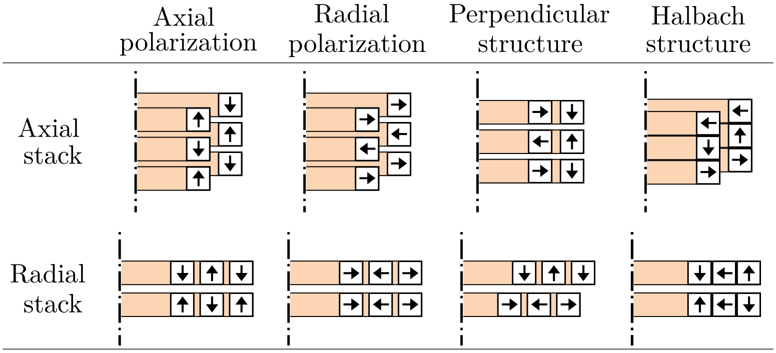

Figure 1.14: 2D sectional view of the different considered topologies of PM thrust bearing without iron (WoI).

The superposition of PM rings lead to two concentric structures where magnetic forces appear. These magnetic forces are repulsive or attractive. For each topology, a lot of these combinations are involved but some combinations are predominant.

- For the radial stack, the main forces are repulsive. Figures 1.15.a and 1.15.c show the evolution of the axial force with the axial offset for a pair of rings and a triple pair of rings respectively.
- For the axial stack, the type of force varies with the relative axial position of the inner rings with the outer rings as shown in Fig 1.15.b and 1.15.d, for a pair of rings and a triple pair of rings respectively. In the position of the maximum axial force, their is no predominance between repulsive and attractive force.

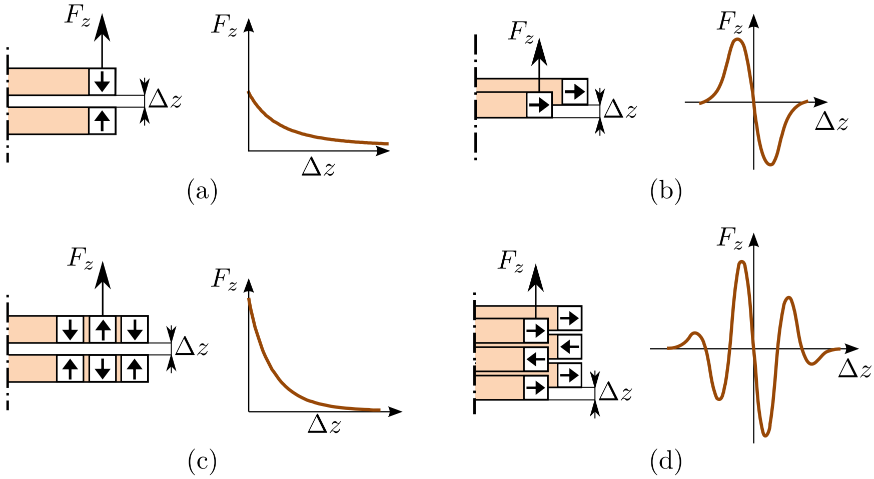

Figure 1.15: Evolution of the axial force F_z with the axial offset Δz for a pair of rings (a and b) and a triple pair of rings (c and d) for axial stack (a and c) and radial stack (b and c).

The magnetic flux lines are given in Fig. 1.16 for topologies without iron. As observed, their distribution is clearly different for radially and axially stacked topologies which explain the difference in the force evolution as shown in Fig. 1.15.

The use of ferromagnetic materiel allows for certain topologies to increase the axial force with the same PM volume [52]. This additional ferromagnetic material leads to two additional structures: the *back-iron structure* [50] and the *induced-pole structure* [56]. For the *back-iron structure*, an iron frame is placed at the back of the structure. This leads to the eight additional topologies with back-iron (BI) illustrated in Fig. 1.17. For the *induced-pole structure*, iron rings are placed between the PM rings. This leads to the eight different topologies with induced-pole (IP) illustrated in Fig. 1.18.

To conclude, the topologies can be classified in different types:

- without iron (WhoI), with back-iron (BI) or with induced pole (IP),
- with axial stack (Ax. S) or radial stack (Rad. S),

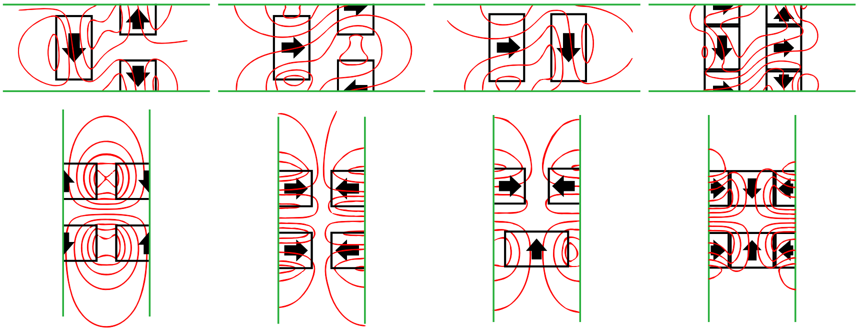

Figure 1.16: Magnetic flux lines (in red) for the axially and radially stacked topologies. The anty-periodicity of the structure is represented in green line.

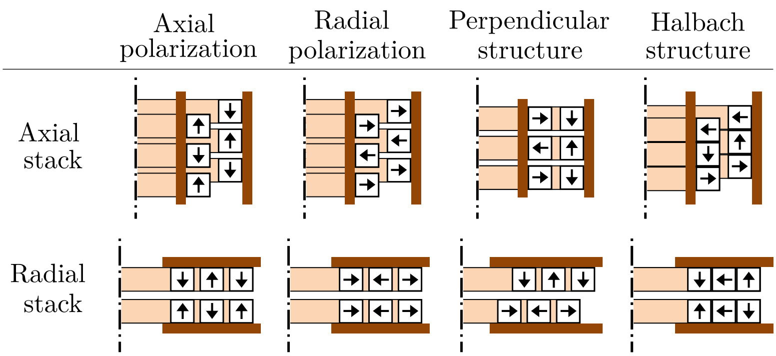

Figure 1.17: 2D sectional view of the different considered topologies of PM thrust bearing with back-iron (BI)

.

- with axial polarization (Ax. P), radial polarization (Rad. P), perpendicular polarization (Perp. P) or Halback array (Hal. P).

A 3D sectional view of some of these topologies are represented in Fig 1.19.

1.2.2 Parametrization

The characteristic dimensions of the topologies are introduced in Fig. 1.20. The ring section is defined by its height h and its width w. The parameter ζ, representing the gap between two adjacent magnets is also considered as it has been shown that for the classical topologies, it allows an increase of the axial force [46].

For the Halbach array, the ring section can be adapted depending on the polarization direction. This leads to 2 different cases.

- For the axial stacked structure, the PM section height can be adapted

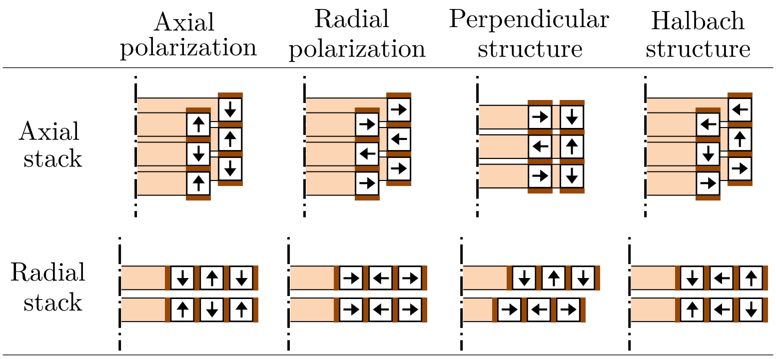

Figure 1.18: 2D sectional view of the different considered topologies of PM thrust bearing with induced-pole (IP)

.

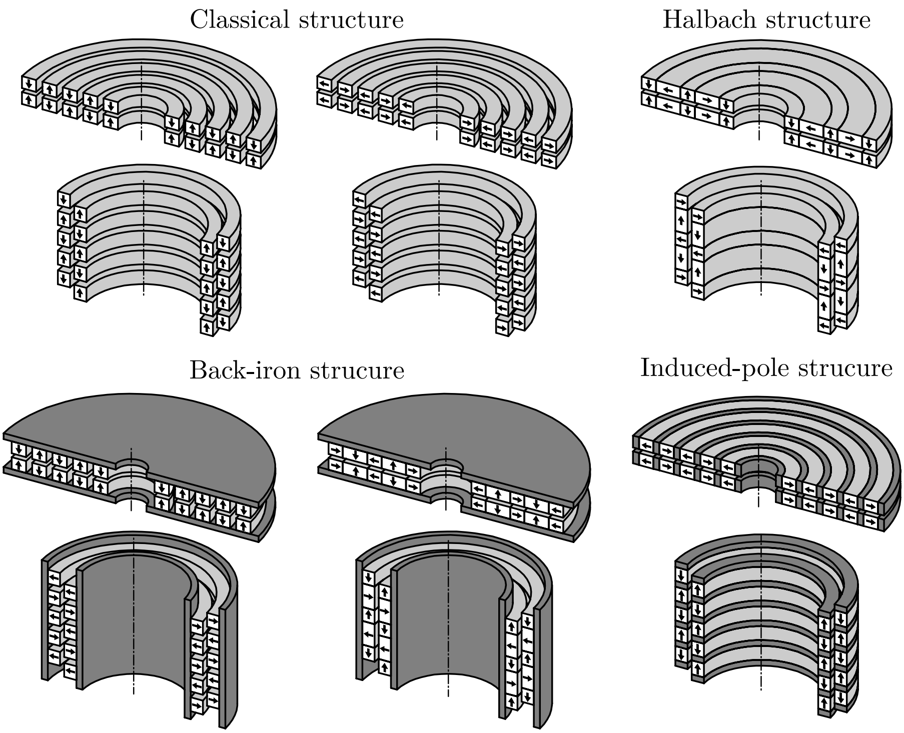

Figure 1.19: 3D sectional view of some considered topologies of PM thrust bearing with in light grey, the PM material and in dark grey, the ferromagnetic material.

with h_{ax} corresponding to the axial polarization direction and h_{rad} to the radial polarization direction.

- For the radial stacked structure, the PM section width can be adapted with w_{ax} corresponding to the axial polarization direction and w_{rad} to the radial polarization direction.

For the Halbach array, no gap is considered because of its negative impact on the axial force [52].

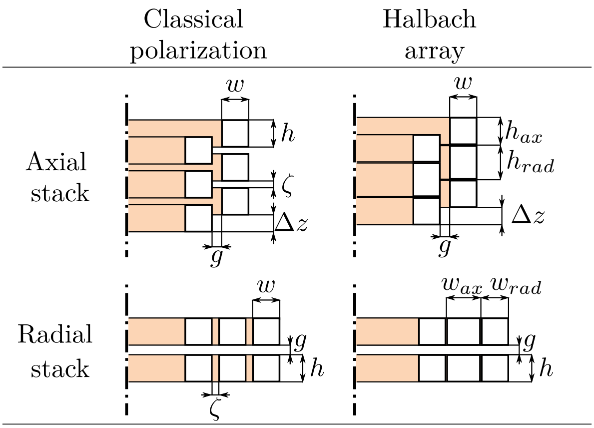

Figure 1.20: Parameters : h height of the ring section ; w width of the ring section ; ζ gap between rings ; g airgap thickness ; Δz axial offset.

The arithmetic mean radius R_{mean} of all rings is also a parameter:

$$R_{mean} = \frac{1}{2N}\left(\sum_{i=1}^{N} R_{s,i} + \sum_{i=1}^{N} R_{r,i}\right) \tag{1.5}$$

where $R_{s,i}$ and $R_{r,i}$ are the mean radius of PM rings from 1 to N of the stator and the rotor respectively. For the axial stacked topologies, it corresponds to radius of the airgap. The remaining parameters are the airgap thickness g, the number of rings in each stack N and the remanence B_r of the PM.

For the topologies with induced pole an additional optimization parameter is considered. It consists of adapting the thickness T_{IP} of the ferromagnetic piece placed between the PM rings. The thickness T_{IP} is represented in Fig. 1.21.

An interesting parameter is the total length L of PM. This parameters depends on the others. It represents, when unrolled and placed side-by-side, the total length of all the PM rings of the thrust bearing. It can be calculated by :

$$L = 2\pi\left(\sum_{i=1}^{N} R_{s,i} + \sum_{i=1}^{N} R_{r,i}\right) \tag{1.6}$$

From (1.5) and (1.6), it is deduced that:

$$L = 4\pi\, N\, R_{mean} \tag{1.7}$$

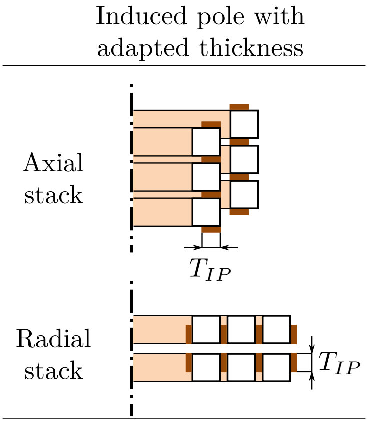

Figure 1.21: Additional parameter for the induced pole topologies: the thickness T_{IP} of the ferromagnetic pieces.

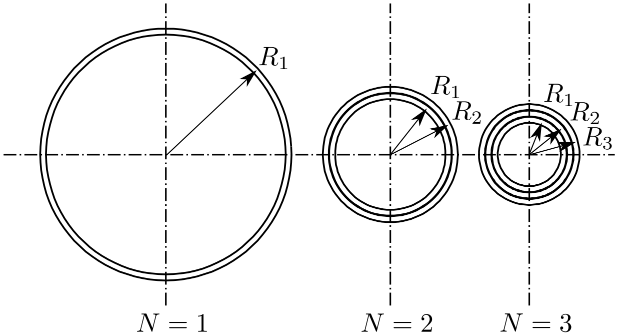

Figure 1.22: Top view of of PMTB with radial polarization with the same total length L but different number of rings N.

The impact of the number of rings N for the same total length L is illustrated in Fig. 1.22 for different PMTB with radial stack.

The volume of PM is easily obtained from the parameters:

$$V = h\, w\, L \tag{1.8}$$

for the axial, radial and perpendicular polarization. For the Halbach array, the volume is obtained by:

$$\begin{aligned} V &= L\, h\, \frac{w_{ax} + w_{rad}}{2}\, F(w_{ax}, w_{rad}, N) && \text{For radial stack} \\ V &= L\, \frac{h_{rad} + h_{ax}}{2}\, w\, G(h_{ax}, h_{rad}, N) && \text{For axial stack} \end{aligned} \tag{1.9}$$

with $F(w_{ax}, w_{rad}, N)$ and $G(h_{ax}, h_{rad}, N)$:

$$\begin{aligned} F(w_{ax}, w_{rad}, N) = &\quad 1 + \frac{1}{2}\frac{w_{ax} - w_{rad}}{w_{ax} + w_{rad}} \\ &\left(\frac{1-(-1)^N}{N} - \frac{4\pi N}{L}\frac{w_{ax} + w_{rad}}{4}\left(1 + (-1)^N\right)\right) \\ G(h_{ax}, h_{rad}, N) = &\quad 1 + \left(\frac{h_{rad} - h_{ax}}{h_{rad} + h_{ax}}\frac{1 + (-1)^{N+1}}{2N}\right) \end{aligned} \tag{1.10}$$

It can be noted that for a number of rings which approaches infinity, the functions $F(w_{ax}, w_{rad}, N \to \infty)$ and $G(h_{ax}, h_{rad}, N \to \infty)$ tend to 1.

1.3 Modelling

In order to evaluate the axial force exerted on the rotor by the stator, different models can be found in the literature [57]:

- equivalent source models
  - method of the equivalent magnetizing currents (Amperian approach),
  - method of the equivalent magnetic charges (Coulombian approach),
- Maxwell's stress tensor method,
- virtual work method.

This section summarizes the different models used in this work to evaluate the axial force for the topology without iron (WoI), with back-iron (BI) and with induced pole (IP). The choice of the models is based on a trade-off between accuracy and computation time since the model is used in an optimization process.

1.3.1 Topology without iron

To evaluate the axial force for topology without iron (WoI), we opted for models based on the Coulombian approach. The following hypotheses are made to derive the magnetic force:

- the magnetic permeability of the PM is the same as the vacuum permeability $\mu_{PM} = \mu_0$;
- the PM polarization is rigid and uniform.

The Coulombian approach uses fictitious magnetic surface charge density $\sigma = B_r$ to model the magnetic field of the PMs as shown in Fig. 1.23. The studied topologies are a construction of the four possible combinations of polarizations: axial-axial, radial-radial, radial-axial and axial-radial. The total axial force F_z exerted on the rotor is obtained from the double sum of the axial forces $f_z^{r,s}$ exerted on rotor ring r by stator ring s through:

$$F_z = \sum_{r=1}^{N}\sum_{s=1}^{N} f_z^{r,s}. \tag{1.11}$$

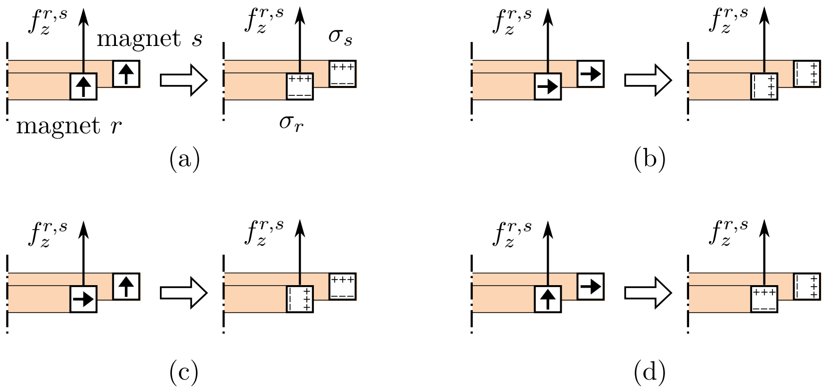

Figure 1.23: Equivalent magnetic charge density for the four possible combinations of polarization.

Different models based on the Coulombian approach can be found in the literature. A 2D plane approach was developed by Yonnet [53]. The complete resolution is analytical but the curvature effect is not considered. In [55, 58], Ravaud et al. use a 2D axisymmetric model to take the curvature effect into account. However, they necessitate one or more numerical integrations that increases noticeably the computation time.

With the 2D axisymmetric model proposed by Ravaud et al. the force between rings is calculated using:

$$\vec{f}_{r,s} = \int_{S_r} \int_{S_s} \frac{\sigma_r \sigma_s}{4\pi\mu_0} \frac{\vec{r}_r - \vec{r}_s}{|\vec{r}_r - \vec{r}_s|^3} dS_s dS_r, \tag{1.12}$$

where σ_r and σ_s are the magnetic surface densities of the rotor and the stator respectively, dS_r and dS_s the surface elements of the densities, $\vec{r}_r$ and $\vec{r}_s$ the position vectors of elements dS_r and dS_s and μ_0 the vacuum magnetic permeability.

With the 2D plane model proposed by Yonnet, the force between two rings is calculated using:

$$\vec{f}_{r,s} = 2\pi R_{mean} \int_{l_r} \int_{l_s} \frac{\sigma_r \sigma_s}{2\pi\mu_0} \frac{\vec{r}_r - \vec{r}_s}{|\vec{r}_r - \vec{r}_s|^2} dl_s dl_r, \tag{1.13}$$

where dl_r and dl_s are the length elements of the charge densities, and $\vec{r}_r$ and $\vec{r}_s$ the position vectors of elements dl_r and dl_s. Contrary to (1.12), the resolution of (1.13) is completely analytical and the solution for axial-axial polarization is:

$$
\begin{aligned}
\frac{f_z^{r,s}}{2\pi R_{mean}} =& \frac{\sigma_r \sigma_s}{2\pi\mu_0} \Big[\mathrm{f}(y_r = y_1, y_s = y_3) \\
& \quad - \mathrm{f}(y_r = y_1, y_s = y_4) \\
& \quad + \mathrm{f}(y_r = y_2, y_s = y_4) \\
& \quad - \mathrm{f}(y_r = y_2, y_s = y_3) \Big] \\
\mathrm{f}(y_r, y_s) =& \mathrm{g}(y_r, x_s = x_4, y_s) \\
& - \mathrm{g}(y_r, x_s = x_3, y_s) \\
\mathrm{g}(y_r, x_s, y_s) =& \mathrm{h}(x_r = x_2, y_r, x_s, y_s) \\
& - \mathrm{h}(x_r = x_1, y_r, x_s, y_s) \\
\mathrm{h}(x_r, y_r, x_s, y_s) =& -(x_r - x_s) \arctan\left(\frac{x_r - x_s}{y_r - y_s}\right) \\
& + \frac{1}{2}(y_r - y_s) \ln\left((x_r - x_s)^2 + (y_r - y_s)^2\right),
\end{aligned}
\tag{1.14}
$$

with (x_1, x_2, x_3, x_4) ; (y_1, y_2, y_3, y_4) described in Fig. 1.24. The resolutions for the other combinations of polarization can be found based on [53] and the results are similar to (1.14).

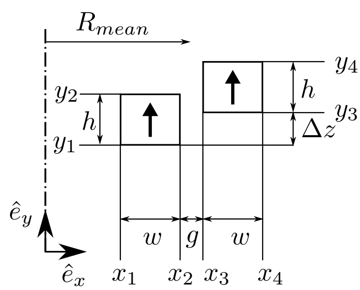

Figure 1.24: Parameters of one pair of rings.

To choose the most appropriate model, the influence of the curvature on the axial force is given in Fig. 1.25 for the case of axial-axial polarization. The error is calculated for the axial displacement Δz corresponding to the maximum axial force. The force calculated by the 2D axisymmetric model is taken as the reference. The curvature is defined as the ratio between the total thickness $2w + g$ and the radius of the airgap R_{mean}. In [48], Marth et al. showed similar results as well as Lang et al. [47].

In the case of a thrust magnetic bearing with high load capacity ($R_{mean} \gg 2w + g \Leftrightarrow (2w + g)/R_{mean} \ll 1$), the curvature effect is negligible and the relative error stays below 1%. The computation time of the axial force exerted between two PM rings on a Intel(R) Xeon(R) CPU ES-2667 v3 3.20GHz (2 processors) with Matlab is 1.4×10^{-4} seconds for the 2D plane model and 3.2×10^{-2} seconds for the 2D axisymmetric model. Even if none of the model implementation on Matlab is optimized, the certainty of having a very small relative error when working with the 2D plane model, and the importance of

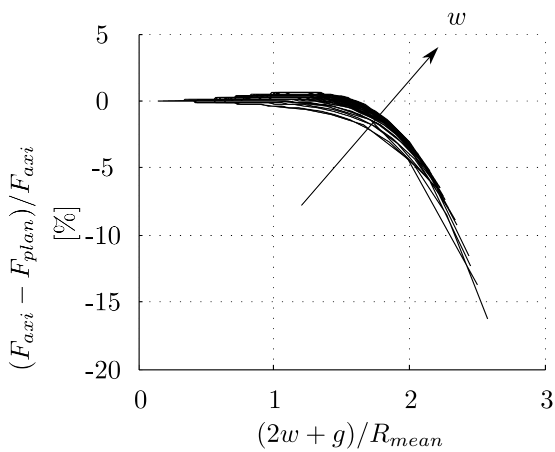

Figure 1.25: Effect of the curvature on the axial force for different magnet thicknesses $w = (5.0\,;13.3\,;21.7\,;30.0\,[mm])$ and airgap thicknesses $g = (1.0\,;2.5\,;5.0\,[mm])$ with $h = w$.

computation time when carrying optimizations, led us to the decision of working with the 2D plane model.

Finally, the axial stiffness K_z can be calculated by the analytical or numerical derivation of (1.14) [37]. Due to Earnshaw's theorem [19], the sum of the stiffness in the three dimensions is:

$$K_z + 2K_r = 0 \tag{1.15}$$

Then the radial stiffness K_r may be derived from (1.15). For axially stacked topologies, working at the maximum axial force leads to an axial stiffness K_z which is substantially equal to zero. The radial stiffness K_r is consequently equal to zero. For radially stacked topologies, the axial stiffness is positive and contributes to the axial stability. The radial stiffness is consequently negative. Thus a correct centering will be required in the complete system, by means of mechanical bearings or active magnetic bearings.

Maximal force for axial stacked topologies

The axial force depends on the axial offset Δz for axial stacked topologies. In this work, the axial offset is chosen to correspond to the maximal axial force.

$$\Delta z|_{F_z=\max(F_z)} = \Delta z_{opt} \tag{1.16}$$

For topology with perpendicular polarization, the maximal force is rigorously reached for $\Delta z_{opt} = 0$. For the other topologies, the maximal force is reached for an axial displacement of approximatively the half of a structure and a baseline estimation Δz^0_{opt} can be obtained by:

$$\Delta z^0_{opt} = -\frac{h+\zeta}{2} \tag{1.17}$$

for topology with standard polarization and:

$$\Delta z^0_{opt} = -\frac{h_{rad}+h_{ax}}{2} \tag{1.18}$$

for Halbach topologies. For the determination of the Δz_{opt} corresponding to the maximal axial force, the Newton's method is used on the axial stiffness $K_z = -\frac{\partial F_z}{\partial z}$. The latter is obtained by numerical derivation of the axial force. Assuming that the stiffness depends linearly on the axial position around the first estimation Δz^0_{opt} obtained from (1.17) or (1.18), the convergence is good enough in only one iteration. Consequently, the axial force need to be evaluated 4 times:

- 3 times to evaluate 2 axial stiffnesses at 2 different axial positions,
- once to evaluate the axial force after the first Newton iteration.

The topologies with axial stack is therefore 4 times more calculation time-consuming than topologies with radial stack except for the perpendicular polarization where the axial offset is equal to zero.

1.3.2 Topology with back-iron

In order to evaluate the force of topology with back-iron (BI), the Coulombian approach is also used and is combined with the method of image charges. The back-iron is modelled by considering infinite the magnetic permeability of the back-iron [50, 59]. This is illustrated in Fig. 1.26 for the radial stack and in Fig 1.27 for the axial stack. On this basis, the axial force $f_{r,s}$ exerted on the ring r by the ring s is calculated by the double sum of the forces exerted on the rotor rings r_i by the stator rings s_j (real for $i;j=0$ and virtual $i;j \geq 1$):

$$f_{r,s} = \sum_{i=0}^{N_{mirror}=\infty} \sum_{j=0}^{N_{mirror}=\infty} f_{r_i,s_j}, \tag{1.19}$$

The convergence of the sum is studied by comparing the results for different values of N_{mirror}. The convergence is shown in Fig. 1.28 for one example case. The example is for one pair of PM rings. The polarization is axial and the PM are placed in repulsion. The PM dimensions are given in Table 1.5. As shown, the axial force calculation converges for $N_{mirror} \geq 3$.

The total axial force F_z of the topologies with back-iron made of stacks of N PM rings is calculated by (1.11) as for the topologies without iron. The axial stiffness K_z can be calculated by the numerical derivation of the axial force.

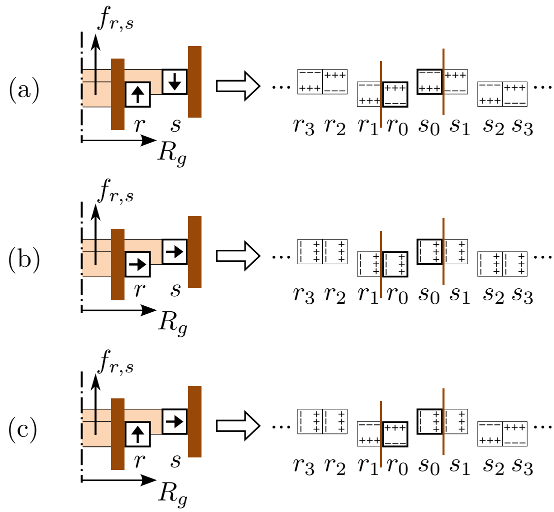

Figure 1.26: Equivalent magnetic charge density for topologies with axial stack and for the four possible combinations of polarization: (a) for the axial-axial, (b) for the radial-radial and (c) for the axial-radial and radial-axial.

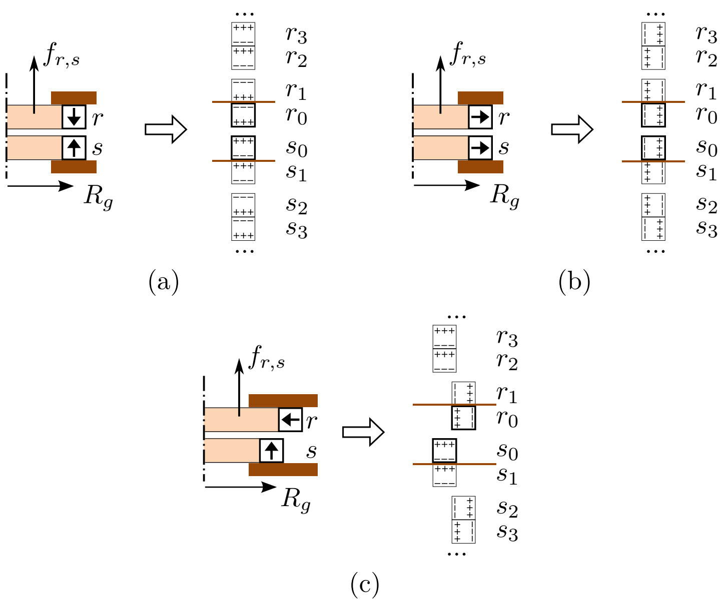

Figure 1.27: Equivalent magnetic charge density for the radial stack and for the four possible combinations of polarization: (a) for the axial-axial, (b) for the radial-radial and (c) for the axial-radial and radial-axial.

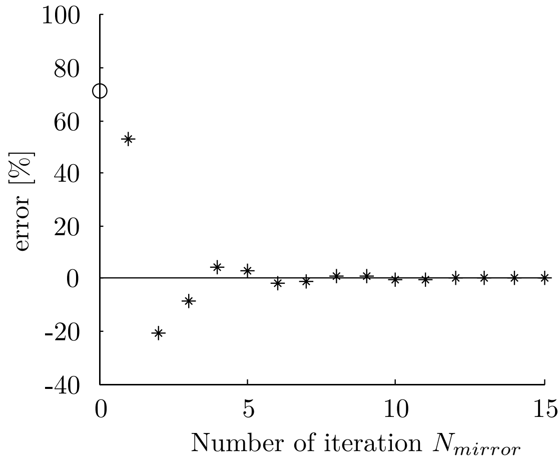

Figure 1.28: Convergence of the axial force F_z with the number on partial sum N_{mirror} in % of the relative error : $error = \frac{F_z^{N_{mirror}=15} - F_z^{N_{mirror}}}{F_z^{N_{mirror}=15}}$. The value of the parameters is given in Table 1.5.

Table 1.5: The value of the parameters for Fig. 1.28 for one pair of PM rings ($N = 1$) with axial polarization and in repulsion.

	Parameter	Value
h	Magnet section height	7.5 mm
w	Magnet section width	15 mm
R_{mean}	Mean radius	392.5 mm
B_r	Remanence	1 T
g	Airgap thickness	2 mm
N	Number of rings	1

For the axial stacked topologies, the axial force also varies with the axial offset and reach a maximum for a specific value of this axial offset. The same procedure as for topology without iron is used to evaluate the maximal axial force and the corresponding axial offset.

1.3.3 Topology with induced pole

The model used to evaluate the magnetic force for topology with induced-pole is based on a finite element model (FEM). The same hypotheses and parameters are considered than for the Coulombian approach model. This model increases the computation time in comparison of the Coulombian approach but the latter is not adapted for this topology. For consistence with the models used for the other topologies, a 2D plane model is also used.

The FEM is implemented in COMSOL Multiphysics. The axial force per unit length f_z is evaluated by the Maxwell stress tensor. The axial force is deduced by:

$$F_z = 2\pi R_{mean} f_z \tag{1.20}$$

1.4 Scaling laws and topology comparison

The aim of this section is to give a systematic comparison between the PMTB. This comparison is based on scaling laws able to size optimal PMTB able to:

- generate a reference axial force: $F_{z,ref}$,
- for a given airgap thickness g,
- and for given PM material corresponding to a remanence B_r.

The scaling laws predict the minimal PM volume needed to meet these criteria as well as the corresponding optimal PM dimensions.

This section first describes the method followed to derive the scaling laws. Then, the scaling law predictions are compared to an independent optimization in order to validate the results.

1.4.1 Scaling law derivation

As shown in the state of the art, the topologies can be characterized based on dimensionless quantities defined in (1.1) for the stiffness k^* and in (1.4) for the force f^*. Based on this principle, the minimum amount of PM volume needed to generate a given axial force for a given airgap thickness and remanence can be obtained with:

$$V_{opt} = \hat{V}_{opt} \frac{g\, F_{z,ref}}{P_m} \; \left[m^3\right] \tag{1.21}$$

with $\hat{V}_{opt}$ the scaling law coefficient corresponding to the minimal value of dimensionless coefficient $\hat{V} = \frac{1}{f^*}$ and P_m the magnetic pressure obtained by:

$$P_m = \frac{B_r^2}{2\mu_0} \; \left[Pa = \frac{N}{m^2} = \frac{J}{m^3}\right] \tag{1.22}$$

As shown in the state of the art, dimensionless coefficient $\hat{V}$ is only dependent on the ratio between the PM section dimensions and the airgap thickness: $\hat{V}\left(\frac{h}{g}, \frac{w}{g}, \frac{\zeta}{g}\right)$ with h the PM section height, w the PM section width and ζ the gap between the PM. At the optimum, these ratio are therefore constant and the optimal PM section dimensions can be predicted:

$$\begin{aligned} h_{opt} &= \hat{h}_{opt}\, g \; [m] \\ w_{opt} &= \hat{w}_{opt}\, g \; [m] \\ \zeta_{opt} &= \hat{\zeta}_{opt}\, g \; [m] \end{aligned} \tag{1.23}$$

with for the Halbach array topologies, the possibility to adapt the section size in function of the polarization direction leading in $\hat{h}_{ax,opt}$ and $\hat{h}_{rad,opt}$ for the axial stack and in $\hat{w}_{ax,opt}$ and $\hat{w}_{rad,opt}$ for the radial stack.

As shown in Section 1.2, the PM volume and the PM dimensions are linked by:

$$\begin{aligned} V &= h\, w\, L && \text{for standard polarization,} \\ V &= (h_{ax} + h_{rad}) w \frac{L}{2} && \text{for Halbach with axial stack,} \\ V &= h(w_{ax} + w_{rad}) \frac{L}{2} && \text{for Halbach with radial stack.} \end{aligned} \tag{1.24}$$

Combining (1.21), (1.23) and (1.24), the optimum total length of PM can be obtained:

$$L_{opt} = \hat{L}_{opt} \frac{F_z}{g P_m} \; [m] \tag{1.25}$$

with

$$\begin{aligned} \hat{L}_{opt} &= \frac{\hat{V}_{opt}}{\hat{h}_{opt}\, \hat{w}_{opt}} && \text{for standard polarization,} \\ \hat{L}_{opt} &= \frac{2\, \hat{V}_{opt}}{(\hat{h}_{ax,opt} + \hat{h}_{rad,opt})\, \hat{w}_{opt}} && \text{for Halbach with axial stack,} \\ \hat{L}_{opt} &= \frac{2\, \hat{V}_{opt}}{\hat{h}_{opt}\, (\hat{w}_{ax,opt} + \hat{w}_{rad,opt})} && \text{for Halbach with radial stack.} \end{aligned} \tag{1.26}$$

The state of the art also shows the impact of the number of rings N on the optimal PM volume and dimensions and proves that the latter converge to a constant value for an increasing N. Therefore, the global optimum is reached for a hypothetical infinite number of rings. In order to objectively compare the PMTB topologies, the optimal scaling law coefficients are obtained for this theoretical infinite number of rings.

In order to evaluate the scaling law coefficients, an optimization of each topology is performed. The objective function is to minimize the ratio of the PM volume on the axial force. The optimization parameters are the PM section height h, width w and gap ζ. The optimization is performed for an airgap thickness g of $2\,mm$ and a remanence B_r of $1\,T$. The optimization can be expressed:

$$\min_{h,w,\zeta} \left(\frac{V}{F_z} \right) \Bigg|_{g=2\,mm, B_r=1\,T,\, N=\infty} \tag{1.27}$$

The ratio between the PM volume and the axial force is evaluated by a 2D plane FE model. The model profits of the anty-periodicity of the magnetic field and therefore corresponds to evaluate the force for topology with an infinite number of rings. The principle of the FE model is shown on Fig 1.29. A 2D plane FE model evaluates the axial force by unit length f_z and then, the ratio $\frac{V}{F_z}$ is obtained:

$$\begin{aligned} \frac{V}{F_z} &= \frac{2hw}{f_z} && \text{for standard polarization,} \\ \frac{V}{F_z} &= \frac{(h_{ax}+h_{rad})w}{f_z} && \text{for Halbach with axial stack,} \\ \frac{V}{F_z} &= h\frac{(w_{ax}+w_{rad})}{f_z} && \text{for Halbach with radial stack.} \end{aligned} \tag{1.28}$$

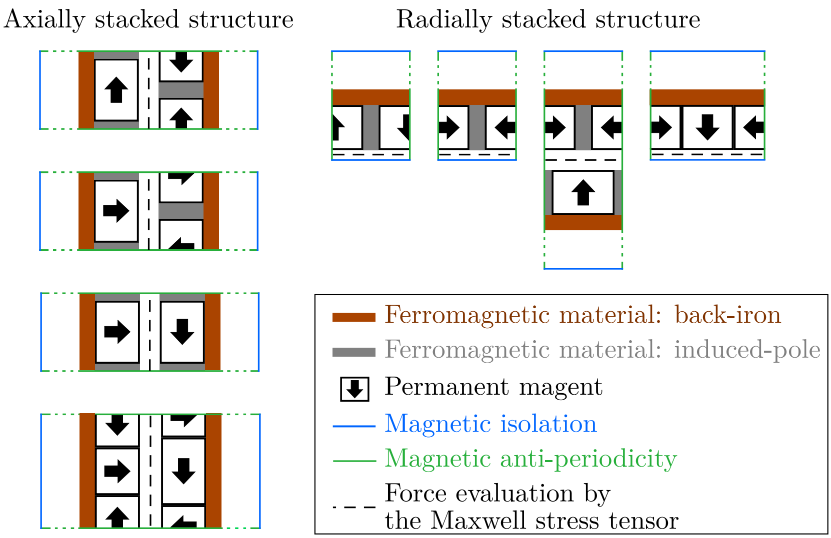

Figure 1.29: Finite element model with infinite N.

Table 1.6 and Table 1.7 summarized the scaling law coefficients obtained by the optimization of each topology. The scaling law coefficients are derived by the optimization of only one set of airgap thickness $g = 2\,mm$ and remanence $B_r = 1\,T$ and for the number of rings $N = \infty$. The coefficient are deduced using (1.21), (1.23) and (1.25).

It is observed that for the induced-pole topologies, the optimization tends to delete the iron pieces placed between the PM except for two topologies. For the Halbach arrays, the possibility to adapt the section dimensions depending on the polarization direction is not used for topology without iron and leads to $\hat{h}_{ax,opt} = \hat{h}_{rad,opt}$ and $\hat{w}_{ax,opt} = \hat{w}_{rad,opt}$. For topology with back-iron, this adaptation is used.

An Additional observation shows that for all the topologies, the PM dimensions are between 0.72 and 2.45 times the airgap thickness, which means very small magnets sections as observed in the literature.

Table 1.6: Scaling law coefficients $\hat{V}_{opt}$ of the optimal PM volume for topology without iron (WhoI), with back-iron (BI) and with induced pole (IP).

	Axial stack with polarization:				Radial stack with polarization:			
	Axial	Radial	Perp.	Hal.	Axial	Radial	Perp.	Hal.
	PM Volume $\hat{V}_{opt}$							
WhoI	14.53	14.53	14.41	8.24	14.38	14.38	14.51	8.22
BI	20.77	7.18	15.36	7.52	8.43	20.72	15.94	7.91
IP	11.06	×	×	×	×	14.81	×	×

Table 1.7: Scaling law coefficients of the optimal PM dimensions for topology without iron (WhoI), with back-iron (BI) and with induced pole (IP).

	Axial stack with polarization:				Radial stack with polarization:			
	Axial	Radial	Perp.	Hal.	Axial	Radial	Perp.	Hal.
	PM section height $\hat{h}_{opt}$							
WhoI	2.26	2.24	2.47	1.59	1.26	1.26	1.26	1.28
BI	2.27	2.32	2.49	0.87^{ax} 2.08^{rad}	0.72	2.39	1.63	1.05
IP	2.02	×	×	×	×	1.15	×	×
	PM section width $\hat{w}_{opt}$							
WhoI	1.26	1.25	1.28	1.25	2.45	2.45	2.26	1.61
BI	2.37	0.62	1.55	0.86	2.13	2.40	2.22	0.84^{rad} 2.19^{ax}
IP	2.05	×	×	×	×	1.78	×	×
	Space between PM rings $\hat{\zeta}_{opt}$							
WhoI	0.88	0.89	0.74	0	0.73	0.73	0.88	0
BI	0.86	0.91	0.72	0	0.67	0.76	0.85	0
IP	1.61	×	×	×	×	0.79	×	×
	Total length of PM rings $\hat{L}_{opt}$							
WhoI	5.10	5.18	4.55	3.64	4.67	4.64	5.08	4.02
BI	3.86	4.98	3.99	4.18	5.54	3.61	4.41	4.97
IP	2.67	×	×	×	×	7.23	×	×

1.4.2 Scaling law validation

In order to validate the scaling laws, the predicted optimal PM volume and dimensions are compared to the results of an independent optimization for a wide range of reference axial loads, airgap thicknesses and remanences. As demonstrated in the state of the art, the optimal PM volume and dimensions tends to constant values with an infinite number of rings. Nevertheless as shown in the literature, the convergence is good enough for a number of rings larger than 10. Therefore, the validation is done for a number of rings of 20.

The optimum volume is calculated for the topologies without iron and with back-iron for $F_{z,ref} = (10, 20, ... 50)\,[kN]$, $g = (0.5, 1.0, ... 2.5)\,[mm]$ and for $B_r = (0.8, 1.0, 1.2)[T]$. The number of rings is set to $N = 20$. The optimization can be expressed:

$$\min_{h,w,\zeta,L} (V)|_{F_z \geq F_{z,ref},\, g,\, B_r,\, N=20} \tag{1.29}$$

The magnetic force is evaluated by the 2D analytical model based on the Coulombian approach presented in Section 1.3.

The results for the optimal PM volume for the axially stacked Halbach array without iron are shown in Fig. 1.30. It shows the evolution of the optimal PM volume with the axial force in Fig. 1.30.a and with the remanence in Fig. 1.30.b for different airgap thicknesses. The corresponding optimum PM dimensions are shown in Fig. 1.31. The optimal PM volume predicted by the scaling laws derived in this section are the lines and the optimal PM volume obtained by independent optimisations are the stars.

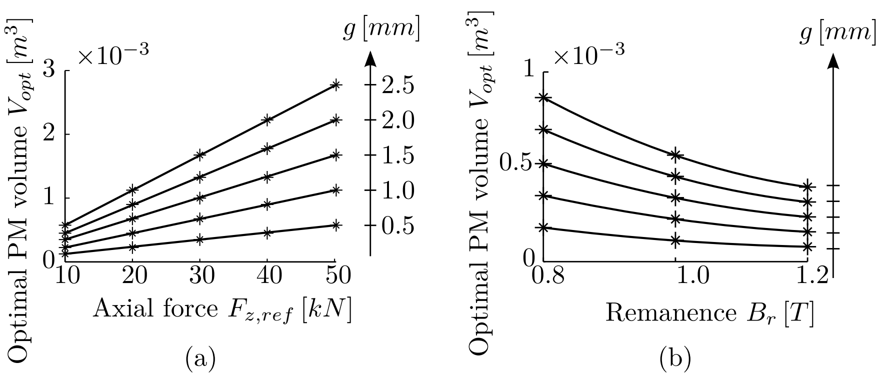

Figure 1.30: Evolution of the optimal PM volume with (a) the axial load $F_{z,ref} = (10, 20, ... 50)\,[kN]$ ($B_r = 1\,[T]$) and with (b) the remanence $B_r = (0.8, 1, 1.2)\,[T]$ ($F_{z,ref} = 10\,kN$) for the axially stacked Halbach array without iron for different airgap thickness $g = (0.5, 1.0, ... 2.5)\,[mm]$. Points: values calculated by the optimization algorithm, continuous lines: values predicted by the scaling laws.

The results show very good correspondence between the prediction and the independent optimization. The results for the other topologies without iron and with back-iron give similar outcomes but are not presented here. For the

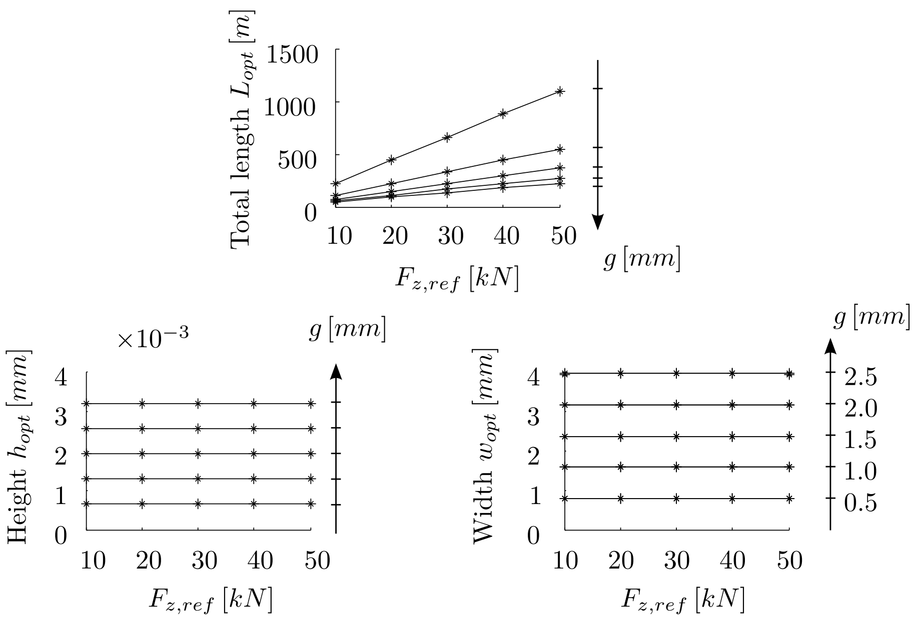

Figure 1.31: Evolution of the optimal PM dimensions with the axial load $F_{z,ref} = (10, 20, ... 50)\,[kN]$ $(B_r = 1\,[T])$ for the axially stacked Halbach array without iron for different airgap thickness $g = (0.5, 1.0, ... 2.5)\,[mm]$. Points: values calculated by the optimization algorithm, continuous lines: values predicted by the scaling laws.

induced pole topologies, the results are not verified due to computation time but are supposed to be similar.

1.5 Correction functions

The scaling laws developed in Section 1.4 allow to size optimal PMTB. Nevertheless, the optimal dimensions can be reach only in an ideal configuration with:

- an infinite number of rings or at least a very high value,
- and without constraint on the PM dimensions.

As shown in the state of the art and from scaling law observation, the optimal dimensions are quite difficult to realize as observed in the previous section. This section proposed to add to the scaling laws, corrections functions able to adjust the optimal dimensions in order to take into account, first, the influence of a limited number of rings and, then, a limited total PM length.

1.5.1 Limited number of rings

The influence of a limited number of rings N is studied and characterized. In order to help designer with the impact of the limited number of rings, correction functions are derived. This influence is studied for one set of axial load $F_{z,ref} = 50\,kN$, airgap thickness $g = 1\,mm$ and remanence $B_r = 1\,T$. Each topology is optimized separately for different values of the number of rings N.

The optimization objective is to minimize the PM volume, the optimization parameters are the PM section height h, width w and gap ζ as well as the total PM length L. The magnetic axial force is constrained to be larger or equal to the reference force $F_{z,ref}$. The magnetic force is evaluated by the analytical model based on the Coulombian approach presented in Section 1.3 for topologies without iron and with back-iron, and with the FE model for topologies with induced pole. The optimization can be expressed:

$$\min_{h,w,\zeta,L} (V)|_{g=1\,mm, B_r=1\,T,\, N,\, F_z \geq F_{z,ref}} \tag{1.30}$$

with the number of rings N varying from 1 to 30 for topologies without iron and with back-iron and from 3 to 15 for induced pole topologies.

Optimal PM volume

Firstly in Fig. 1.32, Fig. 1.33 and Fig. 1.34, the value of the optimal PM volume for a given number of rings V_{opt}^{N} is given for topologies without iron, with back-iron and with induced pole respectively. As observed, this optimal PM volume decreases with the increase of number of rings N which is consistent with the literature [37, 47, 49, 50, 52].

This evolution is explained by the contribution of the PM rings placed at the edge of the structure to the total axial force. Indeed, these PM rings have less interactions with the others than PM rings placed inside the structure. This leads to a lower contribution to the total axial load. By increasing the number of rings, their relative contribution to the axial load decrease and this negative effect is mitigated. Therefore, the PM volume converges asymptotically towards a minimum value V_{opt}. This optimum corresponds to the ideal case with an infinite number of rings.

Secondly, the topologies without iron can be divided into four groups (see arrows in Fig. 1.32):

- Standard topologies with shift (in blue) ;
- Standard topologies without shift (in green) ;
- Halbach topology with shift (in red) ;
- Halbach topology without shift (in black).

The shift can be axial or radial. It ensures that the relative position between the rotor and the stator allows to have the maximum axial force. It is observed

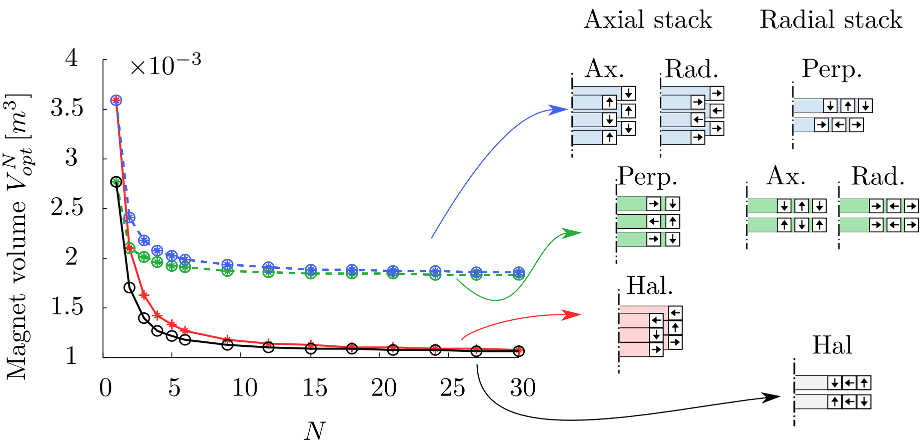

Figure 1.32: Minimum magnet volume V_{opt}^N for the topologies without iron as a function of the number of rings N with: $F_{z,ref} = 50\,kN$, $g = 1\,mm$ and $Br = 1\,T$.

that the Halbach structures need less PM volume than standard structures. This result is consistent with the literature [46]. The axial offset has a slight negative impact explained by an increase of the negative effect of the two rings placed at the ends of the stacks and therefore, contribute a little less to the force than the other rings.

As observed by Yonnet [53], their is a reciprocity between the axial and the radial polarization for a same kind of superposition. The reciprocity is also observed between the axial and radial stack but with a small difference due to the axial shift.

Thirdly, Fig. 1.33 also shows the impact of the back-iron (BI) on the optimal PM volume for each topology. Depending on the kind of topology, the impact of the BI can be positive or negative. Its impact can be divided into four groups.

- For topology with axial stack / axial polarization and topology with radial stack / radial polarization, the BI deviates the magnetic flux produced by PM out of the air gap. This leads to a high negative impact of the BI ;
- For topology with perpendicular polarization, the BI deviates the magnetic flux produced by PM out of the air gap but only on one side. This leads to a low negative impact of the BI ;
- For the Halback arrays, the BI closes the magnetic circuit followed by the magnetic flux behind the PM but with a little effect due to the natural tendency of Halbach array to condensate the magnetic flux inside the airgap. This leads to a low positive impact of the BI ;
- For topology with axial stack / radial polarization and topology with radial stack / axial popularization, the BI closes the magnetic circuit followed by the magnetic flux behind the PM. This leads to a high positive impact of the BI.

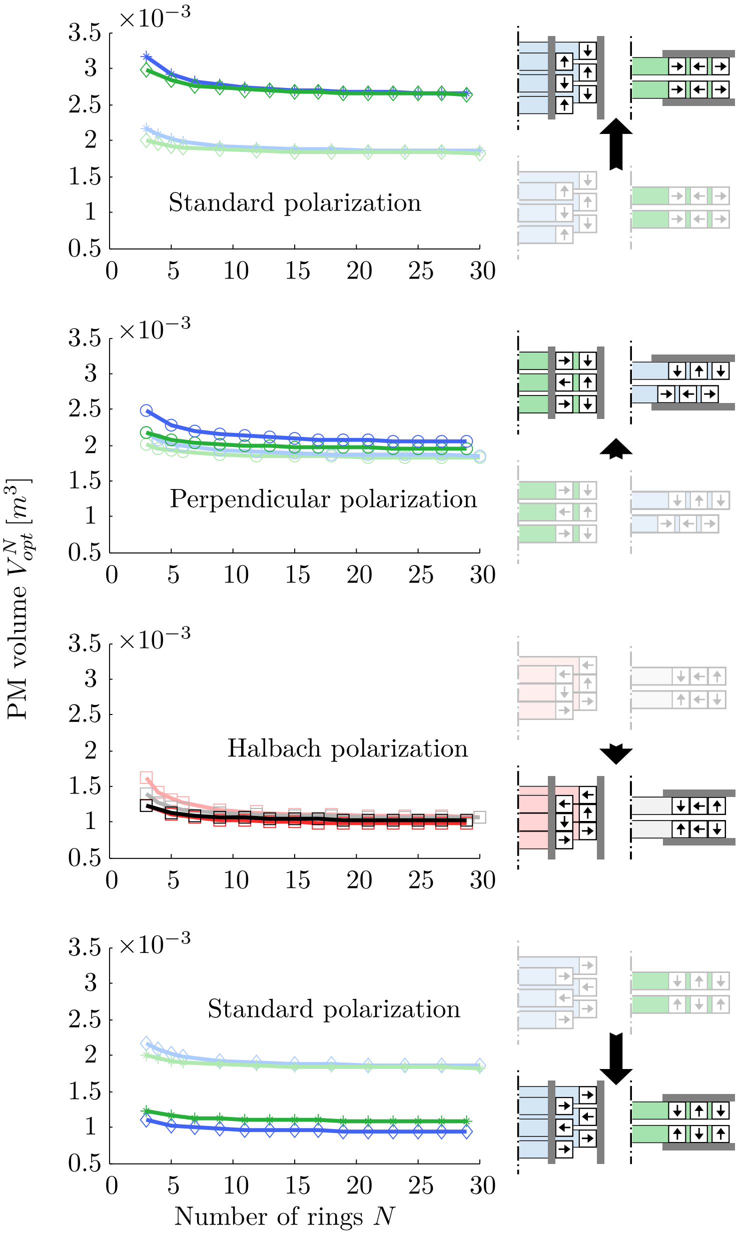

Figure 1.33: Minimum magnet volume V_{opt}^N for the topologies with back-iron as a function of the number of rings N with: $F_{z,ref} = 50\,kN$, $g = 1\,mm$ and $Br = 1\,T$.

Finally, Fig. 1.34 shows the impact of the induced pole (IP) on the optimal PM volume for two topologies. Radially stacked topology with radial polarization suffers a low negative impact of the addition of IP. By contrast, the axially stacked topology with axial polarization profits of a high positive impact. For the both topologies, the IP guide the magnetic field in the airgap and therefore, has a positive impact on the magnetic field repartition. However for the radially stacked topology, the iron pieces of one structure are attracted by the PM rings of the other one leading to a diminution of the axial force.

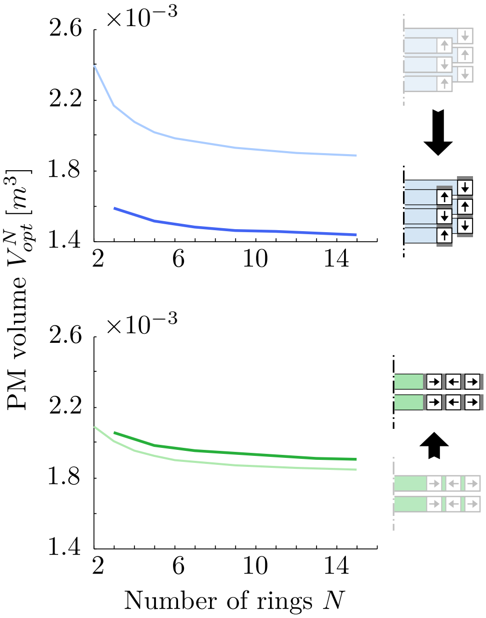

Figure 1.34: Minimum magnet volume V_{opt}^N for the topologies with induced pole as a function of the number of rings N with: $F_{z,ref} = 50\,kN$, $g = 1\,mm$ and $Br = 1\,T$.

Optimal PM dimensions

In Fig. 1.35, Fig. 1.36 and Fig. 1.37, the influence of the number of rings N on the optimal PM dimensions is shown for topology without iron, with back-iron and with induced pole. As observed, all the parameters converge with the number of rings N in the same way than the optimal PM volume except for the induced pole topologies. This is explained by lower quality of convergence in the optimization process due to the use of a FE model.

Figure 1.35 shows that there is a reciprocity between the results in the axial and radial stacked topology without iron: in Fig. 1.35.a and Fig. 1.35.b the values of the PM height h in one structure are equivalent to the values of PM width w in the other. In the cases of Halbach arrays, the possibilities to change the section dimensions (h_{ax}/h_{rad} and w_{rad}/w_{ax}) for each polarization is not useful as illustrated in Fig. 1.35.a and 1.35.b. The total length L is represented in Fig. 1.35.d

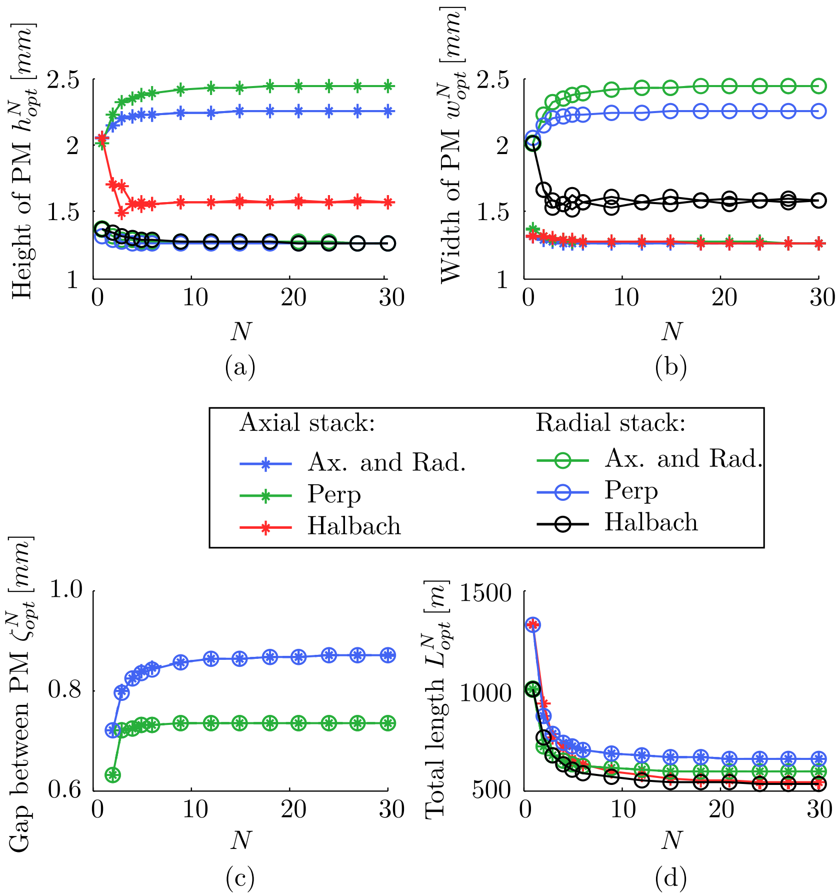

Figure 1.35: Evolution of PM rings dimensions with the number of rings N in the optimal configuration with : $F_{z,ref} = 50\,kN$, $g = 1\,mm$ and $B_r = 1\,T$ for topology without iron.

As observed for topology with back-iron, the reciprocity is no longer observed due to the presence of iron structure. Another observation is that the Halbach arrays profit of the adaptation of the PM section with the direction of polarization.

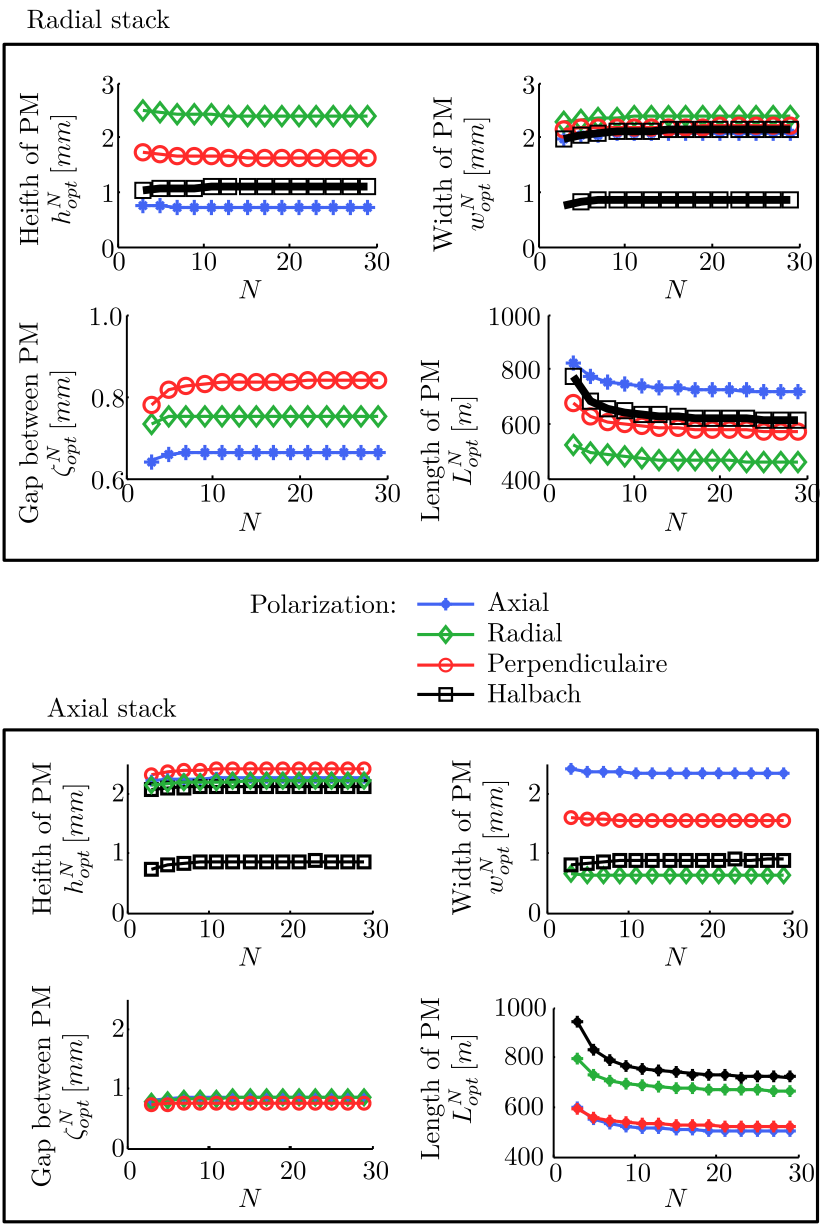

Figure 1.36: Evolution of PM rings dimensions with the number of rings N in the optimal configuration with : $F_{z,ref} = 50\,kN$, $g = 1\,mm$ and $B_r = 1\,T$ for topology with back-iron.

Figure 1.37 shows similar result for induced pole topology than for the other one but with a lower convergence. Nevertheless, it is also observed that there is no reciprocity.

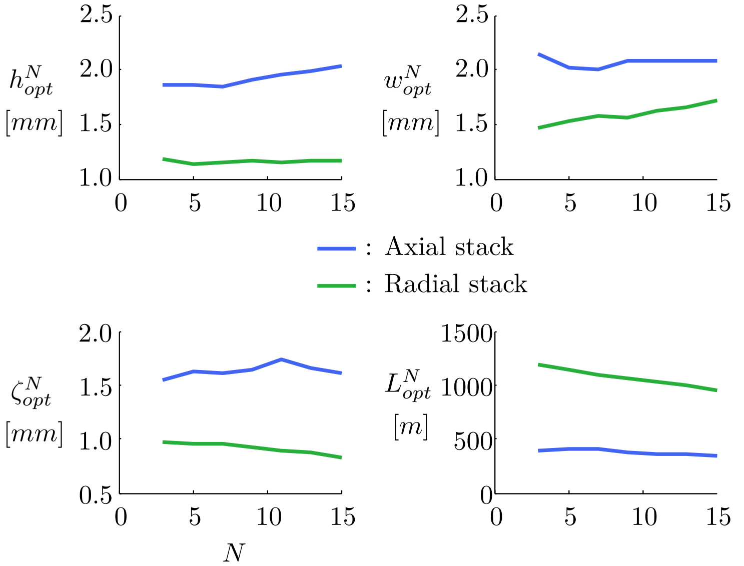

Figure 1.37: Evolution of PM rings dimensions with the number of rings N in the optimal configuration with : $F_{z,ref} = 50\,kN$, $g = 1\,mm$ and $B_r = 1\,T$ for topology with induced pole.

Optimal axial offset

As shown in Fig. 1.15 and explained in (1.17) and (1.18), there is an optimal axial offset Δz_{opt} that maximizes the magnetic force for axially stacked topology. This axial offset depends on the number of rings N except for the topology with perpendicular polarization where the axial offset is equal to zero. The evolution of the axial offset with the number of rings is given in Fig. 1.38 in relative quantity.

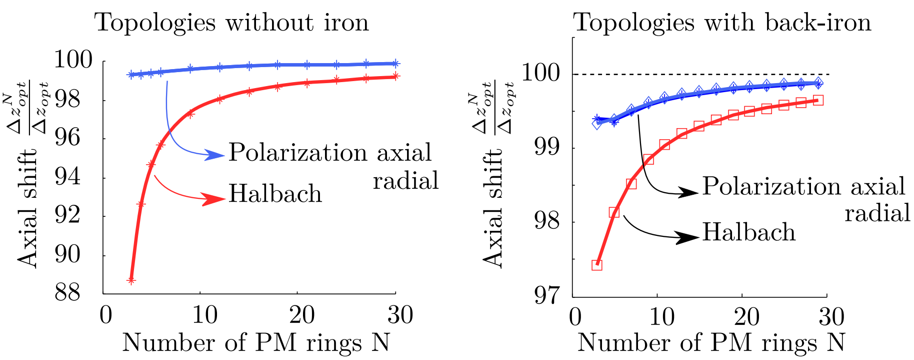

Figure 1.38: Correction functions of the axial shift $f_{\Delta z}(N)$ as a function of the number of rings N with: $F_{z,ref} = 50\,kN$, $g = 1\,mm$ and $B_r = 1\,T$.

It is observed that topologies without iron are more sensitive to this influence than topologies with back-iron. For topology with induced pole, this influence is not studied due to computation time problem.

Correction function derivation

In order to model the influence of a limited number of rings, correction functions on the optimal PM dimensions can be used, such that:

$$\begin{aligned} h_{opt}^N &= h_{opt}\, f_h(N) \\ w_{opt}^N &= w_{opt}\, f_w(N) \\ \zeta_{opt}^N &= \zeta_{opt}\, f_\zeta(N) \\ L_{opt}^N &= L_{opt}\, f_L(N) \\ \Delta z_{opt}(N) &= \Delta z_{opt}\, f_{\Delta z}(N) \end{aligned} \tag{1.31}$$

where h_{opt}^N, w_{opt}^N, ζ_{opt}^N, L_{opt}^N and $\Delta z_{opt}(N)$ are the optimal PM dimensions for a given number of rings N and $f_h(N)$, $f_w(N)$, $f_\zeta(N)$, $f_L(N)$ and $f_{\Delta z}(N)$ are the corrections functions to take into account the influence of the number of rings N:

$$f_i(N) = 1 + \alpha_i \frac{1}{N} + \beta_i \frac{1}{N^2}, \tag{1.32}$$

with $i = h$, w, ζ, L or Δz. For the Halbach array, additional correction functions are considered in order to take into account the adaptation with the direction of polarization.

These correction functions $f_i(N)$ are non physics based and are chosen to fit with the results of Fig. 1.35, Fig. 1.36 and Fig. 1.37. Nevertheless, they converge to 1 for increasing values of N. The value of the coefficients α_i and β_i is calculated by the root mean squared error (RMSE) method. The RMSE is calculated by taking into account the error on the parameters but also on the PM volume (with a weight of 10):

$$RMSE = \sqrt{\sum (10\epsilon_V^2 + \epsilon_h^2 + \epsilon_w^2 + \epsilon_L^2)}, \tag{1.33}$$

where ϵ_V, ϵ_h, ϵ_w and ϵ_L are the relative error of the volume, the section height, the section width and the total length respectively. The weight of 10 on the volume is set because of its importance to guarantee the axial force $F_{z,ref}$. For the gap between PM ζ, the RMSE is calculated independently.

The optimal results, the value of the constants α_i and β_i and the RMSE are given in Appendix A.

1.5.2 Limited total length of PM

The results obtained in section 1.4 give the optimal dimensions of PM rings to carry the load $F_{z,ref}$ for a given airgap thickness g, remanence B_r. In most cases, however, these dimensions are such that realizing thrust bearings based on the latter is not realistic.

This problem can be illustrated by taking the dimensions obtained in Table A.3. The total length L and the characteristic dimensions of the PM section are around 500 m and 2 mm respectively. The manufacture and the manipulation of PM rings of such dimensions is not possible because of their brittle nature. One solution could consists in segmenting the rings into parts of limited length, for instance 15 mm. In this case, the number of manipulations during the assembly, would be around 33000.

With the aim of sizing feasible thrust bearing, a geometrical constraint on the total length L can be added in the optimization process. This additional constraint will obviously lead to a higher PM volume, but it will have a positive impact on the number of manipulations necessary for realization of the bearing. Indeed, for a given length of the segments, their number is directly proportional to the total length L. In addition, a constrain on the total length L will result in PMs having larger cross section, allowing for longer, and therefore fewer, segments. However, reducing the total length of PM too much leads to large PM section. The attractive/repulsive force generated by one single segment is consequently higher and the manipulation of this segment becomes more difficult. The optimal size is therefore a trade-off between:

- the PM volume,
- the PM dimensions (neither too big nor too small)
- the number of segments,
- the magnetic force generated by one segment and the facility of manipulation for the assembly.

More specifically, the impact of a limited total length of PM is studied for each topology. The latter are optimized with the objective to minimize the PM volume. The optimization parameters are the PM section: the height h, the width w and the gap ζ. The optimization is performed for a given axial load $F_{z,ref}$, airgap thickness g and remanence B_r. Imposing a limited total PM length L leads to impose an axial force by unit length $f_{z,ref} = \frac{F_{z,ref}}{L/2}$.

The optimization follows the same process described in section 1.4, with the major difference of adding one constraint on the axial force per unit length:

$$\min_{h,w,\zeta} (V)|_{g=2\,mm, B_r=1\,T,\, N=\infty,\, f_z \geq f_{z,ref}} \tag{1.34}$$

The optimization is done for an airgap thicknesses $g = 2\,mm$ and a remanence of $B_r = 1\,T$.

Optimal PM volume

The evolution of the optimal PM volume is analysed with regard to the deviation of the total length from its optimal value in dimension less quantities $\frac{L}{L_{opt}}$. The PM volume is also expressed in dimensionless quantities $\frac{V_{opt}^{L}}{V_{opt}}$ and shown in Fig. 1.39.

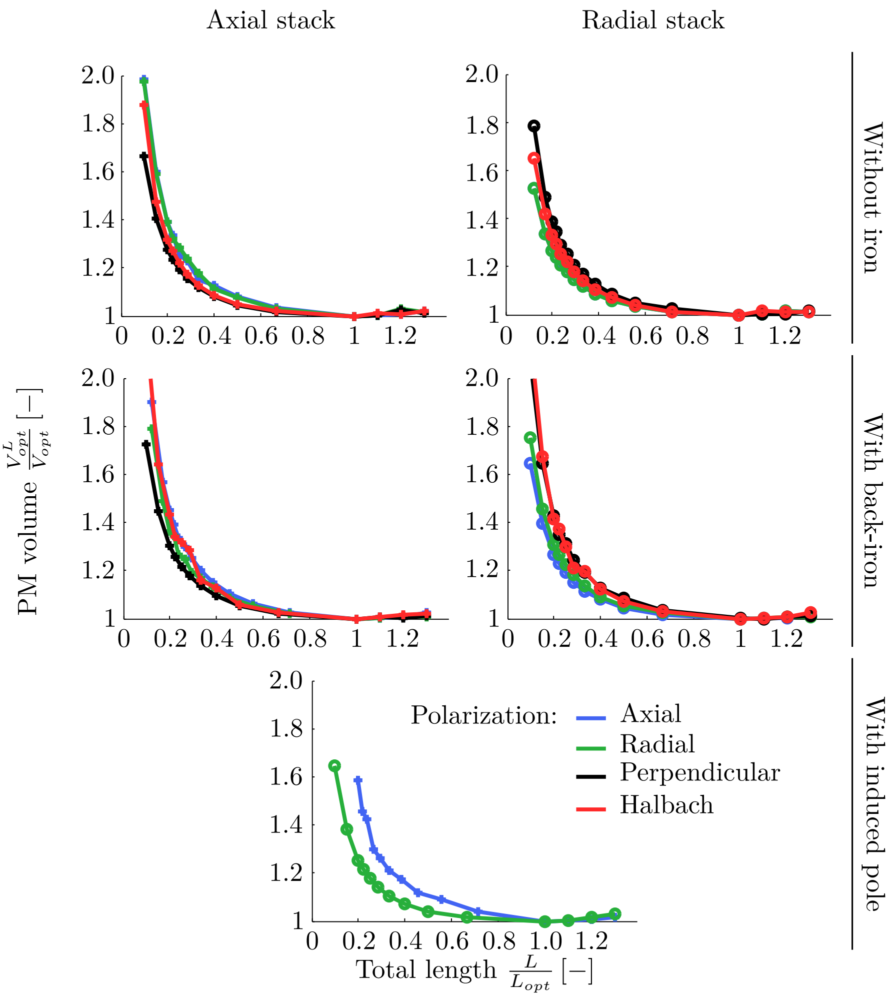

Figure 1.39: Evolution of PM volume with a limited PM length L in dimensionless quantities.

As expected, the PM volume increases when the total length diverges from its optimal value. For example, when the total PM length is reduced by 90% of its optimal values, the PM volume increases approximatively of 1.8 to more than 2 times from its optimal value.

Optimal PM dimensions

The evolution of the optimal PM dimensions with the limited total PM length is shown in Fig. 1.40.

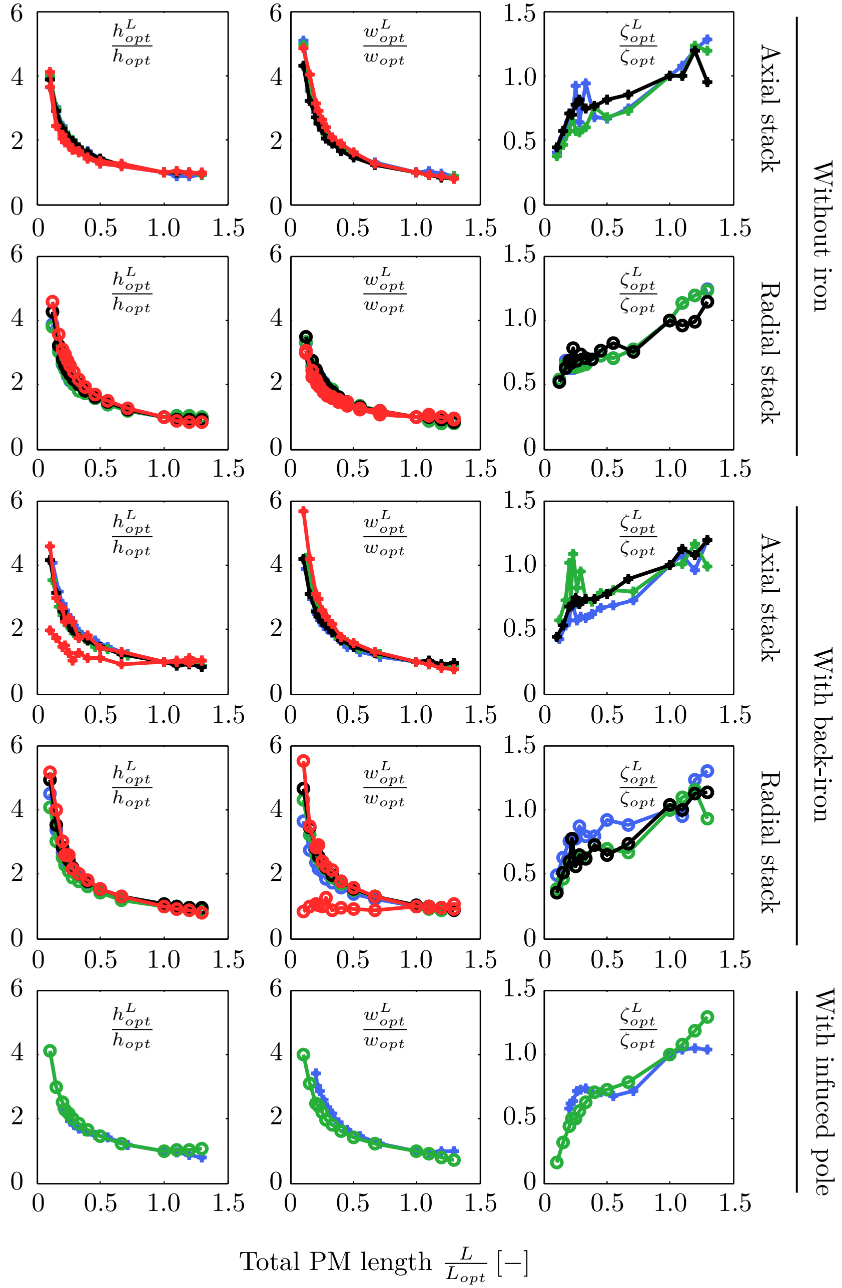

Figure 1.40: Evolution of PM dimensions with a limited PM length L in dimensionless quantities. The legend is the same than in Fig. 1.39.

The PM section increases with a diminution of the PM length and vice versa. The results for the PM section height h and width w are "very good", in opposite of the results for the gap between the PM rings ζ. There is a problem of convergence in the optimization process that could be explained due to bad numeric precision in the force per unit length evaluation by of the finite element model. In order to improve the accuracy, another optimization is perform with the evaluation of the force by unit length done with the analytical model based on the Coulombian approach. The number of rings is imposed to 12, as it has been shown before that such a high N gives approximatively the same results as N infinite. To save computation time, this optimization is performed only for topologies without iron. Additionally, this optimization is done for a wide range of axial loads ($5\,kN$, $25\,kN$, $50\,kN$), airgap thicknesses ($0.5\,mm$, $2.5\,mm$, $5\,mm$) and remanences ($1\,T$, $1.3\,T$). For all combinations of these parameters, the solution is exactly the same and is shown in Fig. 1.41.

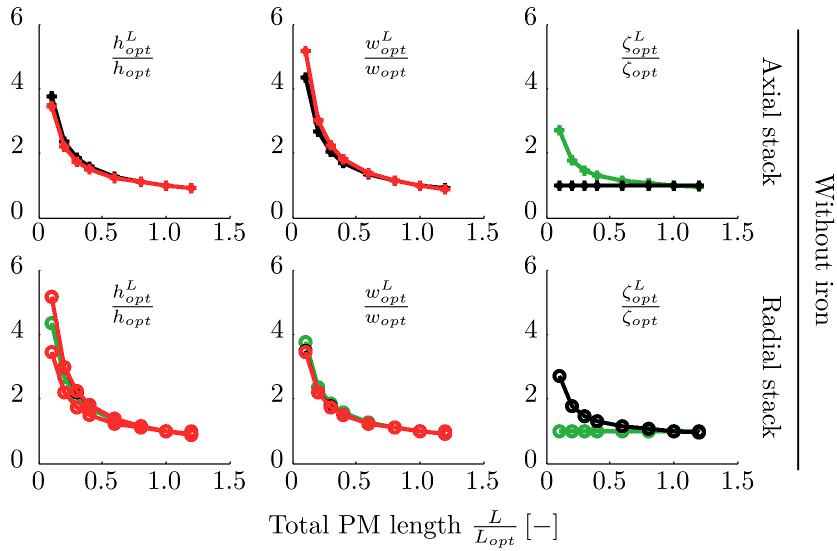

Figure 1.41: Evolution of PM dimensions with a limited PM length L in dimensionless quantities with the force by unit length evaluated with the analytical model based on the Coulombian approach. The legend is the same than in Fig. 1.39. The results are evaluated for different axial loads ($5\,kN$, $25\,kN$, $50\,kN$), airgap thicknesses ($0.5\,mm$, $2.5\,mm$, $5\,mm$) and remanences ($1\,T$, $1.3\,T$)

The results of Fig. 1.41 are equivalent than the results of Fig. 1.40 for the PM height and width. The difference is a better convergence in the optimization process for the gap between the rings.

Correction function derivation

In order to model the influence of a limited PM length L, correction functions on the optimal PM dimensions can be used, such that:

$$\begin{aligned} h_{opt}^{L} &= g_{h}\left(\frac{L}{L_{opt}}\right) \times h_{opt} \\ w_{opt}^{L} &= g_{w}\left(\frac{L}{L_{opt}}\right) \times w_{opt} \\ \zeta_{opt}^{L} &= g_{\zeta}\left(\frac{L}{L_{opt}}\right) \times \zeta_{opt}, \end{aligned} \tag{1.35}$$

where h_{opt}^{L}, w_{opt}^{L}, ζ_{opt}^{L} are the optimal dimensions of the PM for a limited total PM length L and $g_{h}\left(\frac{L}{L_{opt}}\right)$, $g_{w}\left(\frac{L}{L_{opt}}\right)$ and $g_{\zeta}\left(\frac{L}{L_{opt}}\right)$ are correction functions. This relation is approximated by non physic based functions:

$$g_{i}(x) = A_{i} + B_{i}x^{-0.5} + C_{i}x^{-0.75} + D_{i}x^{-1} \tag{1.36}$$

for i equal to h, w and ζ. The value of the constant coefficients A_i, B_i, C_i and D_i (with $i = h$, w, or ζ) are calculated by the same RMSE method than the one presented for the correction function for a limited number of ring.

The value of the coefficients and the RMSE are given in Appendix A. As expected, if no constraint on the total length is considered ($L/L_{opt} = 1$), the parameters remain the same and give $A_i + B_i + C_i + D_i \cong 1$.

1.6 Example of design procedure

This section illustrates how to use the scaling laws and the correction functions for the design of an optimal PMTB for a particular application case. The different steps are to use:

1. the scaling laws to predict the optimal PM dimensions,
2. the correction functions $f_i(N)$ in order to limit the number of rings,
3. the correction functions $g_i\left(\frac{L}{L_{opt}^{N}}\right)$ in order to limit total PM length.

For the example, we consider a thrust bearing with axial polarization and axial stack without iron. It does not correspond to the best topology from the PM volume point of view, but it is not detrimental to the aim of this part. The load is $F_{z,ref} = 13\,kN$, the airgap thickness $g = 3\,mm$ and the remanence $B_r = 1.22\,T$. The optimal PM volume and dimensions are obtained with the scaling laws (1.21), (1.23) and (1.25), with the coefficient of Table 1.6 and Table 1.7. Those optimal theoretical results are given in Table 1.8.

Table 1.8: Optimal dimensions

h_{opt}	w_{opt}	ζ_{opt}	L_{opt}	V_{opt}
$6.77\,[mm]$	$3.77\,[mm]$	$2.62\,[mm]$	$37.5\,[m]$	$0.96\,[dm^3]$

However, as it is impossible in practice to have an infinite number of ring, we choose to limit: $N = 6$. The number of rings is chosen to be $N = 6$. For such a low number of rings, the dimensions of Table 1.8 need to be adapted by using the correction coefficients (1.31) of Section 1.5. The new obtained values are given in Table 1.9. The optimal dimensions for $N = 6$ are shown in Fig. 1.42. The radii reach values difficult to implement in practice.

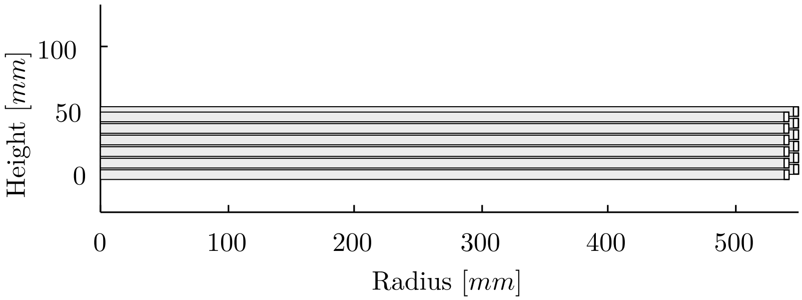

Figure 1.42: Dimensions of the bearing for the minimal magnet volume for $N = 6$, $F_{z,ref} = 13\,kN$, $g = 3\,mm$, $B_r = 1.22\,T$ and without constraint on the dimensions.

Table 1.9: Optimal dimensions with N=6

$h_{opt}^{N=6}$	$w_{opt}^{N=6}$	$\zeta_{opt}^{N=6}$	$L_{opt}^{N=6}$	$V_{opt}^{N=6}$
6.69 [mm]	3.79 [mm]	2.53 [mm]	41.1 [m]	1.04 [dm^3]

Finally, a constraint on the total length L is imposed to reach acceptable dimensions. By using (1.35) and Table B.1, geometries for the PM are found. The choice of the value for the total length would be a trade-off between the material and the assembly costs. For this example, the total length is arbitrary forced at $L = 0.15L_{opt}^{N}$. The final dimensions are summarized in Table 1.10. The dimensions of the bearing are shown in Fig. 1.43.

Table 1.10: Comparison between results obtained with the scaling laws and correction functions (SCL) and an independent optimization (IO)

	$h_{opt}^{N,L}$ [mm]	$w_{opt}^{N,L}$ [mm]	$\zeta_{opt}^{N,L}$ [mm]	L [m]	$V_{opt}^{N,L}$ [dm^3]	$\Delta z_{opt}^{N,L}$ [mm]
SCL	17.76	14.06	5.31	6.16	1.538	-11.47
IO	17.75	14.06	5.29	6.16	1.537	-11.53

To validate these results and, at the same time, the use of the scaling laws and the correction functions, they are compared, in Table 1.10, with those obtained with the constrained optimization process used in Section 1.5, considering the same fixed parameters $F_{z,ref} = 13\,kN$, $g = 3\,mm$, $B_r = 1.22\,T$ and the same constraint on $L = 6.16\,m$.

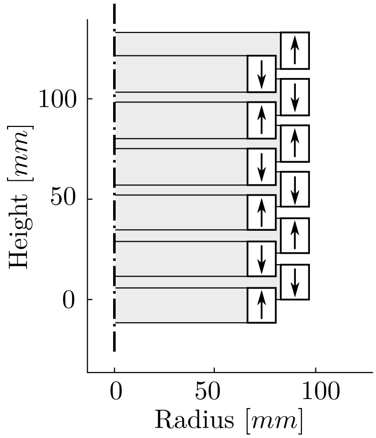

Figure 1.43: Dimensions of the bearing for the minimal magnet volume for $N = 6$, $F_{z,ref} = 13\,kN$, $g = 3\,mm$, $B_r = 1.22\,T$ with constraint on the total length $L = 6.16\,m$.

The use of the scaling laws and corrections functions needs to be mitigated and adapted in function of the application case. Indeed for some cases, the minimum radius can reach value smaller than zero or smaller than a reference minimum radius. Some iterations between the limitation of the number of rings and the PM length need to be performed in order to converge until dimensions that satisfy practical constraints.

1.7 Comparison

Based on the derived scaling laws, topologies without iron, with back-iron and with induced pole are compared based on the minimum PM volume. For this purpose, the optimal PM volume of each topology V_{opt}^{Top} is expressed in percentage of the optimal PM volume of the Halbach array without iron V_{opt}^{ref}. By considering the scaling laws (1.21), the ratio of the PM volumes gives:

$$\frac{V_{opt}^{Top}}{V_{opt}^{ref}} = \frac{\hat{V}_{Top}\frac{gF_{z;ref}}{Pm}}{\hat{V}_{ref}\frac{gF_{z;ref}}{Pm}} = \frac{\hat{V}_{Top}}{\hat{V}_{ref}} \tag{1.37}$$

The ratio between the optimal volume is independent on the axial load, the airgap thickness and the remanence. This allows to compare the different topologies in a very general way, independently to a particular application.

Firstly, the results synthesized in Fig. 1.44 show that the Halbach array are the optimal choice for achieving a given thrust-bearing design with the minimum PM volume for topologies without iron. This is consistent with the literature [37, 46]. The Halbach arrays are around 75% better than the classical polarizations.

Topology	Without iron	With back-iron	With induced pole	With adapted induced pole
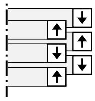	176%	252%	134%	118%
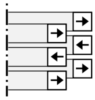	176%	87%		
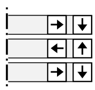	175%	186%		
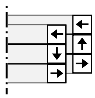	100%	91%		
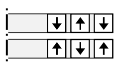	175%	102%		
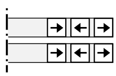	175%	251%	180%	148%
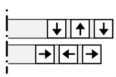	176%	194%		
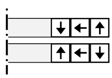	100%	96%		

Figure 1.44: Optimal PM volume ratio in % with the Halbach array without iron as reference $\frac{\hat{V}_{Top}}{\hat{V}_{ref}}$ [%]. The table highlights the performance between the different topologies as well as the influence of the back-iron and the induced pole.

These results also confirms the reciprocity between axial and radial polarization but also, between axially and radially stacked topologies.

Secondly, the addition of the back-iron increases the performance of the classical topologies where the magnetic flux closes behind the PM i.e. the axial stack with radial polarization and the radial stack with axial polarization. This improvement allows classical topology to equal or even to outperform the Halbach array.

The back-iron also increases the performance of the Halbach array but only slightly. As explained in section 1.3, the optimization allows the Halbach arrays to adapt the section of the PM rings with the direction of the polarization. These results are presented in Table 1.7. It is observed that for the topologies without iron, the section of the PM rings is not adapted with the direction of the polarization. But for the topology with back-iron, this section is adapted. Actually, the PM where back-iron closes the magnetic circuit followed by the magnetic flux, increases its section. In opposite, the PM where back-iron deviates the magnetic flux out of the airgap, reduces its section.

Thirdly, the impact of the induced-pole is shown. An additional optimization is performed with an additional optimization parameter. This parameter is the thickness of the induced pole as shown in Fig. 1.21. This additional degree of freedom allows the induced pole to have a width (height) different than the width (height) of the magnet for the radially (axially) stacked topology , and is called "adapted induced pole" in Fig. 1.44.

Fourthly, the addition of soft magnetic material (back-iron and induced pole) have a better impact on the axial stack than on the radial stack. Indeed in the radially stacked structure, the back-iron linked to the rotor (resp. stator) are attracted by the PM linked to the stator (resp. rotor) leading to a diminution of the performance. This effect is more predominant for induced pole topology than for back-iron.

Fifthly, one independent optimization is performed and presented in Appendix C. The aim is to show the impact of the adaptation:

- for classical topology: to have a gap between the rings ζ,
- for Halbach array: to adapt the PM section in function of the polarization direction.

Comparing the values of the dimensionless optimal PM volume of topology with and without adaptation, highlight its impact. The comparison is based on the relative variation of PM volume:

$$\frac{\hat{V}_{opt,i}^{adapt} - \hat{V}_{opt,i}^{simpler}}{\hat{V}_{opt,i}^{adapt}} \; [\%] \tag{1.38}$$

with i the topologies without iron and with back-iron. The results are summarized in Table C.3. It is observed that:

- for classical topologies, the gain is of 16% for topology with shift (see Section 1.5), and of 11.5% for topology without shift,
- for Halbach array, their is no gain for topology without iron as in this case, the optimal results do not adapt the section in function of the polarization direction, and is of 9% for Halbach array with back-iron.

Finally, the global comparison shows that the best topologies are (from the best to the worst):

1. Axial stack with radial polarization and with back-iron (87%)
2. Axial stack with Halbach array and with back-iron (91%)
3. Radial stack with Halbach array and with back-iron (96%)

4–5. Axial and radial stack with Halbach array and without iron (100%)

6. Radial stack with axial polarization and with back-iron (102%)
7. Axial stack with axial polarization and with induced pole (134% or 118%)
8. Radial stack with radial polarization and with induced pole (180% or 148%)

9–12. Classical topologies without iron (175% - 176%)

Figure 1.45 summarizes the twelve different considered topologies.

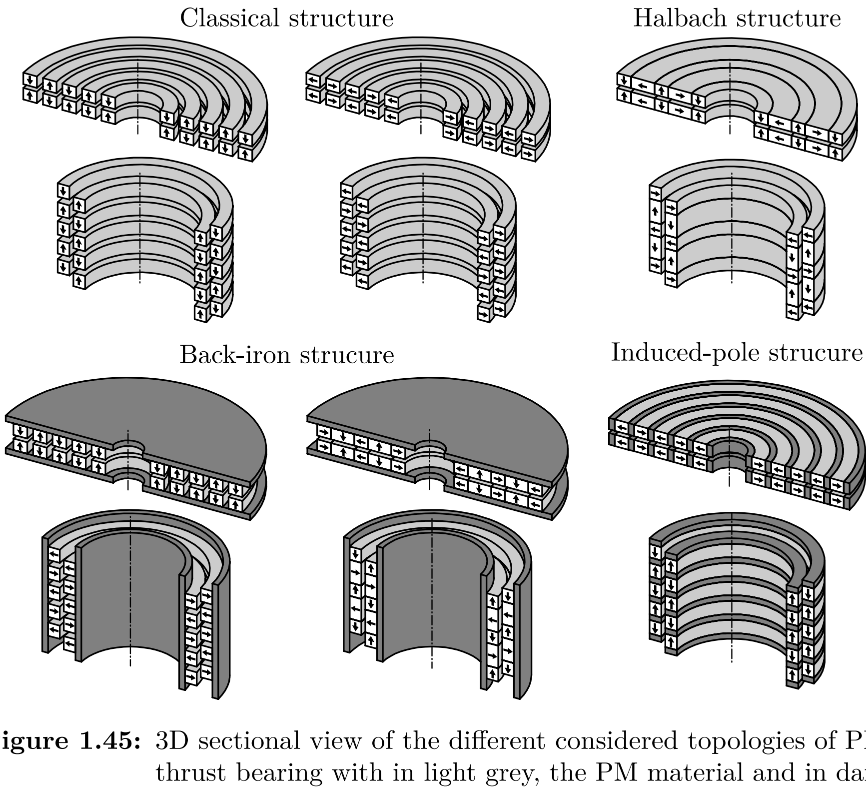

Figure 1.45: 3D sectional view of the different considered topologies of PM thrust bearing with in light grey, the PM material and in dark grey, the ferromagnetic material.

1.8 Conclusion

This chapter presents the characterization and comparison of different permanent magnet (PM) thrust bearing (PMTB). The PMTB's are used as load compensators and therefore are designed to compensate a static axial force e.g.

the weight. The comparison of the topologies is based on the minimization of the PM volume with the constrain to carry a given axial load. The different topologies are:

- axial or radial stack
- with axial, radial, perpendicular or Halbach polarization.

These eight topologies can be improved by the addition of a soft magnetic material leading to two additional groups of topologies: the back-iron and the induced pole topology.

A design procedure for a very fast sizing of a PMTB using a minimum PM volume is described. The procedure can be divided in tree steps. First, scaling laws given the optimal PM rings dimensions for a given axial load, airgap thickness and remanence are derived. These scaling laws consider that the stack of PM rings is infinite. Secondly, correction functions are used to consider the impact of a given number of rings and consequently take in consideration the edge effect. Thirdly, correction function to take the influence of an additional geometrical constraint (the total length) on the dimensions are derived. The procedure to size a permanent magnet thrust bearing is illustrated. The dimensions obtained by the scaling laws and the correction functions are compared to the dimensions obtained by an independent optimization. It shows a very good agreement. Although the study made in this chapter focuses on magnetic thrust bearings, the same approach can be made for permanent magnet centering bearings.

Based on the scaling laws, the topologies are compared on an objective basis. The comparison highlight that for topologies without iron, the Halbach array is basically the most effective. Nevertheless, these topologies are equalized or even outperformed by the topologies with classical polarization when they are combined with back-iron. The addition of ferromagnetic material between the PM rings (induced pole) leads also to interesting performance for classical topologies.

Nevertheless, other characteristics like the stiffness and the stability must be taken into account. This depends on each application and of its complete design, namely the other guiding devices present in the system, the load, and so on. The assembly issues of the Halbach arrays (internal stresses and the need for axially and radially polarized PM) can also influence the choice. Another aspect is the problem of magnetic interference with other equipments due to the magnetic field located out of the airgap. This problem can be limited thanks to the use of Halbach array or back-iron structure.

Publications related to this chapter:

[60] Van Beneden M, Kluyskens V and Dehez B. "Optimal sizing and comparison of permanent magnet thrust bearings". IEEE Transactions on Magnetics, vol. 53, no. 2, 2017, pp. 1–10.

[61] Van Beneden M, Kluyskens V and Dehez B. "Comparison between optimized topologies of permanent magnet thrust bearings with back-iron". Mechanical Engineering Journal, vol. 4, no. 5, 2017, pp. 17–00061–17–00061.

Material comparison 2

This chapter presents the permanent magnet (PM) material comparison used in permanent magnet thrust bearing (PMTB). In a first section, a review of PM material is presented with their man advantage and disadvantage. A state of the art on the influence of the PM material on the PMTB is given. The second section presents the model used to evaluate the force generated by the PMTB taking into account the non-ideal characteristics of the PM material. This model is validated thanks to experimental results. The third section discusses the impact of PM materials on the performances of PMTB. The discussion is divided in two parts. First, the impact of the temperature and demagnetization effect on the PM material working as PMTB is shown. Secondly, the risk of having irreversible demagnetization is studied and this study takes into consideration the choice of the topology.

2.1 State of the art

The main component of PMTB is the PM material as it is at the origin of the repulsive and attractive magnetic force. The comparison of PMTB topology presented in Chapter 1 supposes that this magnetic field is constant and rigid i.e., the polarization remains uniform and oriented in the main direction. Unfortunately, the PM material can be subject to demagnetization or temperature effect which can alter the magnetization of the PM. The performance of the PMTB can no more be predicted based on model presented in Chapter 1. These effects are clearly dependent on the choice of PM material. The aim of this section is to give an overview of the main PM materials and to summarize their principal characteristics. Then, a state of the art dealing with the use of PM in the generation of magnetic force is presented.

As shown in [62], different criteria allowing to compare and select a PM material for a given application can be listed:

- Flux density, remanence – B_r
- Energy Product – $(BH)_{max}$
- Resistance to demagnetization, coercivity – H_c
- Usable temperature range

- Magnetization change with temperature – Reversible Temperature Coefficient
- Demagnetization (2nd quadrant) curve shape
- Recoil permeability – minimal, slightly greater than 1
- Corrosion resistance
- Physical strength – tensile strength, bending strength, chip resistance
- Electrical resistivity – minimizes eddy currents
- Magnetizing field requirement
- Available sizes, shapes, and manufacturability
- Raw material cost and availability

A variety of PM materials can be found in the literature [63] and in the industry [64–66]. Each PM has its own advantages and disadvantages [67]. The main different types of PM material are listed bellow.

Ferrites (ceramics) magnets have been in production since the 1950's. They are mainly made of iron oxide with small proportions of metallic element like barium (Ba) or strontium (Sr). The raw materials are mixed and calcined. They are the least expensive and most common of all magnet materials. They also have excellent corrosion resistance. Their main application fields are for instance in small electric motors and sensors.

Alnico magnets are one of the oldest commercially available magnets (around 1930). They are mainly composed of iron with in addition aluminum (Al), nickel (Ni) and cobalt (Co) material in different proportions. They have a high remanent induction but due to their easy of demagnetization, they have a low resistance to demagnetization, which results in relatively low magnetic performance. However, they present good resistance to temperature variation and to mechanical strength. They resist corrosion properly. Common applications are in measuring instruments and high temperature processes such as holding devices in heat treat furnaces.

Samarium Cobalt magnets are in the rare earth family and are divided in two grades: $SmCo_5$ and Sm_2Co_{17}. They were first developed in 1972. They have high magnetic properties, good resistance to demagnetization and good temperature characteristics. These magnets show excellent corrosion resistance but are very brittle. They are also more expensive than the other magnet materials because of the high concentration of costly samarium. Common uses are in applications with high expectations for both temperature and performance criteria.

Neodymium iron boron magnets are in the rare earth family because of the neodymium (Nd) and boron (B) elements. First developed in 1982, they are the strongest magnets available on the market. They are strongly vulnerable to corrosion and are brittle and get break/crack due to collisions. They have bad temperature stability and are moderately expensive. The addition of dysprosium (Dy) allows to increase their temperature stability but increases significantly their prices. Nevertheless, they have the highest energy density and good resistance to demagnetization, making them one of the most used PM in high performance applications.

Comparison of PM properties can be found classically on PM manufacturer website. Table 2.1 shows a typical comparison.

Table 2.1: PM material criteria classification in ascending order [68, 69].

	Low →			High
Typical cost	Ferrite	Alnico	NdFeB	SmCo
Maximal energy product BHmax	Ferrite	Alnico	SmCo	NdFeB
Typical recommended maximum working temperature	NdFeB	Ferrite	SmCo	Alnico
Temperature stability	Ferrite	NdFeB	SmCo	Alnico
Corrosion resistance	NdFeB	SmCo	Alnico	Ferrite
Demagnetizing field resistance	Alnico	Ferrite	NdFeB	SmCo
Mechanical Strength	Ferrite	SmCo	NdFeB	Alnico

In addition to their material properties, the manufacturing process have an impact on the final PM properties. The different process of compacting and forming a solid PM are listed bellow.

Casted magnets are obtained by liquefaction of the raw material and then by its solidification in a hollow cavity of the desired shape. The material is then magnetized.

Sintered magnets are formed by compacting fine powders at high pressures in an aligning magnetic field. The powders are heated without reaching the melting point. The complexity of shapes using this process is limited. The compression of the powders can be isostatic. The latter allows to reach the highest density and consequently highest magnetic properties. In opposition, the compression can be imposed in only one direction: in the direction of the magnetization or perpendicular to this direction. The perpendicular direction gives better results than the parallel.

Bonded magnets are created either by compression molding or injection molding. In compression molding, the epoxy performs the binding function and in injection molding, it is the polyamides. The magnetic properties are lower because they are not fully dense due to the introduction of resins or epoxies. The main advantage is the possibility to reach complex shapes. The bonded grades are also available by either extrusion or calendaring.

The different PM material are compared in Fig 2.1 based on their remanence B_r and their coercivity H_c. As observed, their performance are dependent on the PM material but also on the manufacturing process. Sintered magnets give better performance than bonded magnets due to their higher density. As already mentioned, the main advantage of bonded magnets is that their manufacturing process reaches complex shapes. In PM bearings, the shapes of PM are quite simple, allowing to work with sintered magnet.

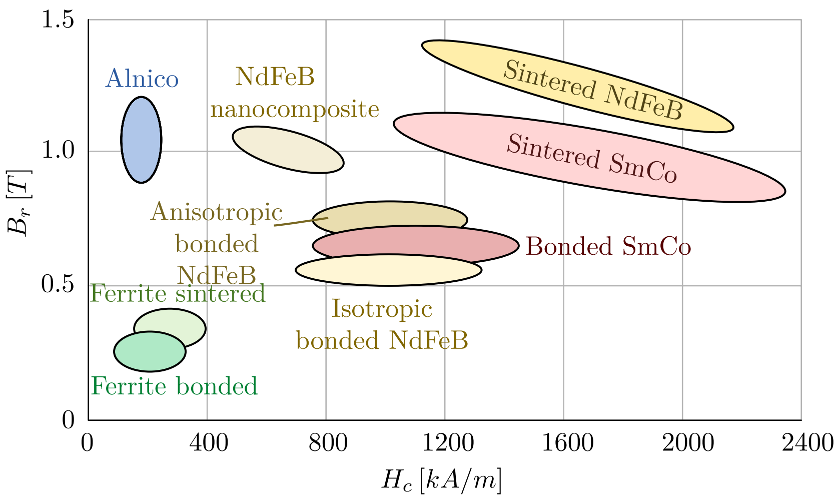

Figure 2.1: Comparison of the main PM materials [70] based on two criteria: the remanence B_r and the coercivity H_c.

Figure 2.1 also shows that neodymium magnet gives the best performances. Nevertheless, the impact of the temperature on the PM properties need to be considered. Figure 2.2 shows the evolution of the maximum energy product with the temperature for different PM material. As observed, all the PM materials have a declining performance with temperature except the alnico magnet which is quite stable. For the rare-earth magnet, the samarium cobalt magnet ($SmCo_5$ and Sm_2Co_{17}) is more stable than the neodymium magnet ($NdFeB$). Nevertheless, the substitution of neodymium by dysprosium component stabilizes the PM performance with the temperature [71]. The disadvantage of this process is the reduction in the energy density. An other disadvantage of PM material based on dysprosium component is the large increase of its price due to the scarcity of this material.

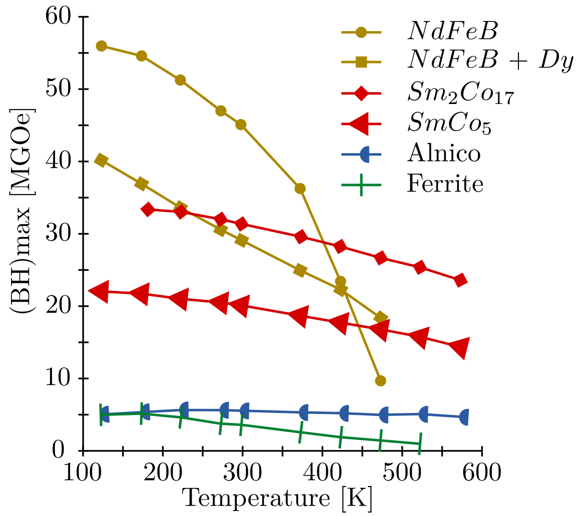

Figure 2.2: Evolution of the maximal energy product with the temperature [72].

In order to reduce the negative impact of dysprosium material on the energy density, authors developed a new step in the manufacturing of neodymium magnet [73]: the grain boundary diffusion (GBD) process. The neodymium iron boron magnets ($NdFeB$) are coated with metal containing dysprosium and then heat-treated. In this situation, the dysprosium is diffused from the surface of $NdFeB$ magnet along the grain boundaries. The $NdFeB$ show very high coercivity without a reduction of the energy density. In [74], authors develop a PM electrical machine based on GBD $NdFeB$ magnets and show that the machine gains significant torque and energy efficiency. Another advantage of this process is that the amount of dysprosium material needed to obtained the same coercivity than with the classic substitution, is 10 times smaller. This process allows to decrease the dependence on the high and volatile cost of rare-earth elements. The drawback of this process is that the thickness of diffusion is limited [64, 75] to around $5\,mm$ and thus the thickness of PM magnet is limited. Nevertheless as shown in Chapter 1, the optimal dimensions of PMTB converges to thin thickness.

In [76], Weickhmann et al. assert that most magnetic bearings are currently made of $SmCo$ magnets. They suggest that with the recent progress on $NdFeB$ magnets and more precisely with the GDB process, the share of $NdFeB$ magnets in magnetic bearings may increase when a higher operating temperature and/or coercivity is needed.

In [77], Pérez-Loya et al. have optimized the force between cylindrical PM made off different materials:

- Neodymium iron boron: sintered $NdFeB$ N45,
- Samarium cobalt: sintered $SmCo_5$ and $Sm(Co, Cu, Fe, Zr)_{7,4}$ and bounded $SmCo_5$,
- Alnico 8,
- Ferrite: sintered and bonded,
- Mn-Al-C.

The B-H curves of the different PM materials are presented in Fig. 2.3. These curves take into consideration the non-homogeneity of the PM magnetization. The figure also shows in dashed-line the equivalent model for a homogeneous magnetization. These curves are implemented in finite element model in order to evaluate the magnetic force.

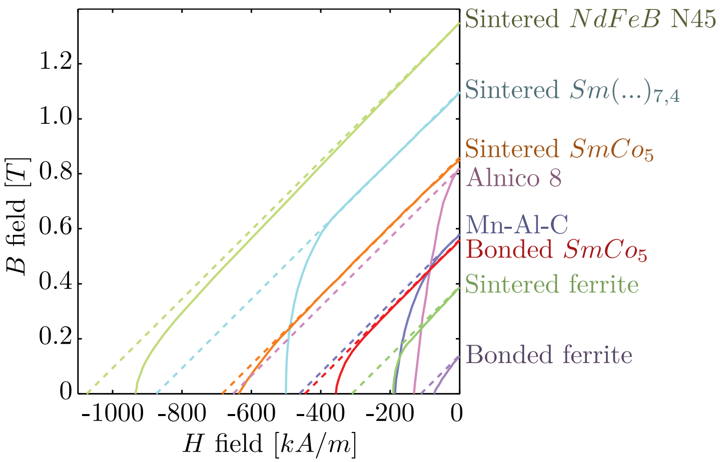

Figure 2.3: $B - H$ curve of the different PM material considered in [77]. Solid line: non-homogeneous magnetization, Dashed line: homogeneous magnetization.

The authors seek to adjust the PM height to diameter ratio to find the maximum magnetic force for a given PM volume of $1000\pi\, mm^3$. The evolution of the magnetic force as function of the aspect ratio and for different airgap thicknesses is given in Fig. 2.4. As reference, an ideal PM is given with a rigid and uniform magnetization for a remanence of $B_r = 1\,T$. For each PM material, the attractive and repulsive force are given in light and dark solid lines respectively for which non-homogeneous B-H curves are considered. The dashed line corresponds to the results with homogeneous magnetization. For the ideal PM, the attraction and repulsion forces are superposed due to the reciprocity principle.

It is observed that for all the PM material the non-homogeneity, decreases the performance and even more in repulsion than in attraction. For sintered rare-earth PM, the curves are quite similar and on the contrary, alnico PM are highly impacted by the magnetization non-homogeneity.

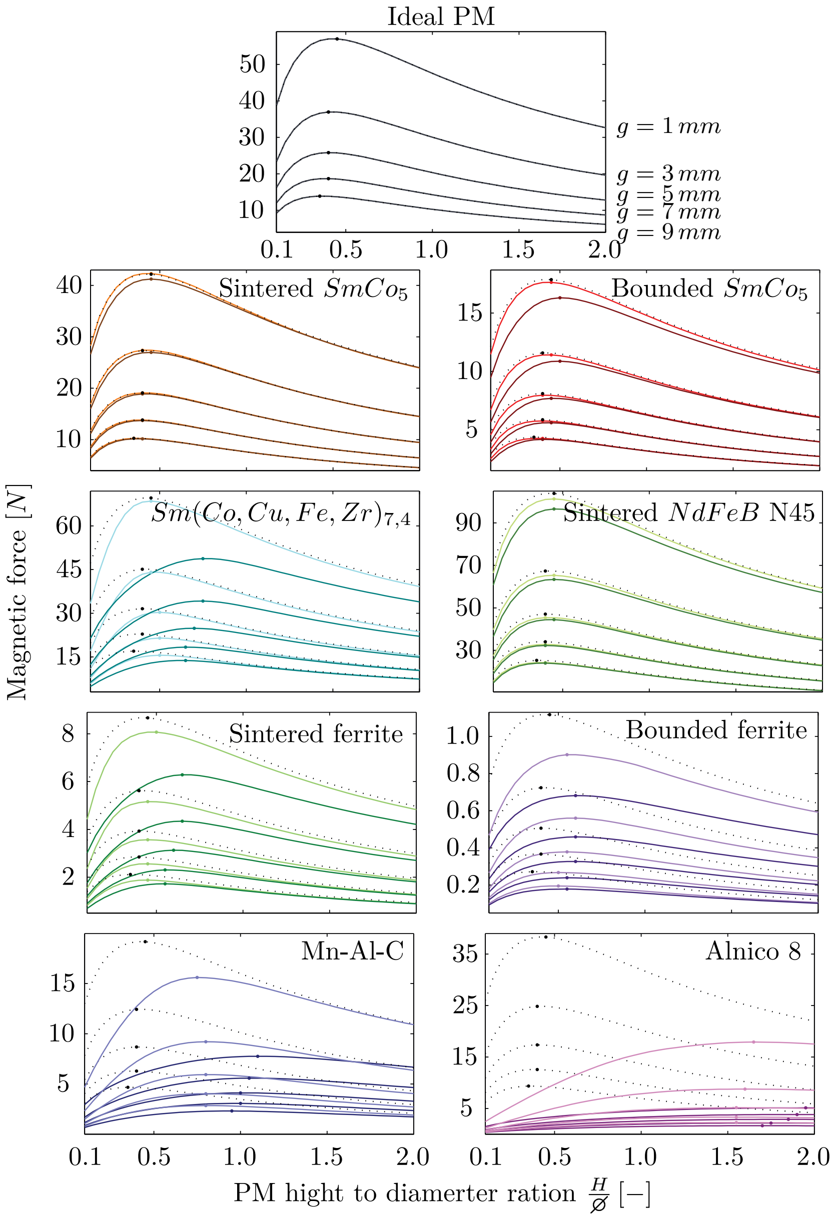

Figure 2.4: Evolution of the force with the aspect ratio for the different PM material and for different values of airgap thickness g [77]. The "ideal PM" has a uniform and rigid magnetization with a value of remanence of $B_r = 1\,T$. For each PM material, the dashed-line corresponds to the results with the hypotheses of a rigid and uniform magnetization but with the nominal value of remanence ; the light and dark solid lines correspond to the force in attraction and repulsion respectively.

The difference between homogeneous and non-homogeneous magnetization is accentuated with the diminution of the airgap thickness. For the sintered ferrite PM, the solid and dashed line are more similar for an airgap thickness of $g = 9\,mm$ than for $g = 1\,mm$. This effect is explained by the increase of the reverse H field with the airgap diminution.

From these results, it is highlighted that the choice of PM material has an impact:

- on the magnetic performances and,
- on the optimal PM dimensions.

Additionally, it appears clearly that sintered rare-earth magnets give the highest force and that neodymium magnet are the best in term of force density. Nevertheless, this studies do not take into consideration other aspects like the temperature effect.

From this state of the art, it arises that the neodymium magnets are the most effective magnets to use in PMTB due to their high energy density and are replaced by samarium magnets in applications with temperature variation. However, this ending can be mitigated if different criteria are combined. For example in [78], Chen et al. compare PM material based on cost-effectiveness ratio for a coaxial magnetic gears applications and examine the impact of the temperature variation. They compare alnico, ferrite, $SmCo$ and $NdFeB$ magnet. It appears than in this case, alnico magnet is the most appropriate PM material.

2.2 Modelling demagnetization and temperature effect

In order to compare the different PM material, a finite element (FE) model taking into account the non-homogeneous polarization and consequently the demagnetization curve of a PM material, is described in this section. It is divided into four parts. First, the reversible and irreversible demagnetization curves are given. Secondly, the temperature effect on the PM properties is described. Thirdly, the PM properties are implemented in a FE model. Finally, the model is experimentally validated.

2.2.1 Reversible and irreversible demagnetization

PM materials are usually characterized by their polarization curve $J - H$ or their magnetic flux density curve $B - H$, linking respectively the evolution of the polarization $\vec{J}$ and the magnetic flux density $\vec{B}$ to the magnetic field $\vec{H}$. In [79], the authors model the polarization $\vec{J}$ in PM as solely due to the magnetic field parallel to the polarization. In [80, 81], they prove that the perpendicular field needs, in some cases, to be considered. However most of authors [82, 83] neglect this influence, leading to:

$$\begin{aligned} \vec{B}_{\parallel} &= \mu_0 \mu_{r,\parallel} \vec{H}_{\parallel} + \vec{J}(\vec{H}_{\parallel}) \\ \vec{B}_{\perp} &= \mu_0 \mu_{r,\perp} \vec{H}_{\perp} \end{aligned} \tag{2.1}$$

with μ_0 the vacuum permeability and $\mu_{r,\parallel}$ and $\mu_{r,\perp}$ the reversible permeability of the PM in the direction parallel and perpendicular to the PM polarization respectively. In [81], Katter shows that these both reversible permeabilities are different and reach for sintered $NdFeB$ magnets, values of 1.03 to 1.05 for $\mu_{r,\parallel}$ and 1.12 to 1.17 for $\mu_{r,\perp}$. The former is dependent on the compression technique and the latter is dependent on the coercivity. From PM manufacturers, most of the time only the information about $\mu_{r,\parallel}$ are communicated and is called the relative permeability μ_r. For convenience in this thesis, the reversible permeabilities $\mu_{r,\parallel}$ and $\mu_{r,\perp}$ are supposed to be equal to this relative permeability.

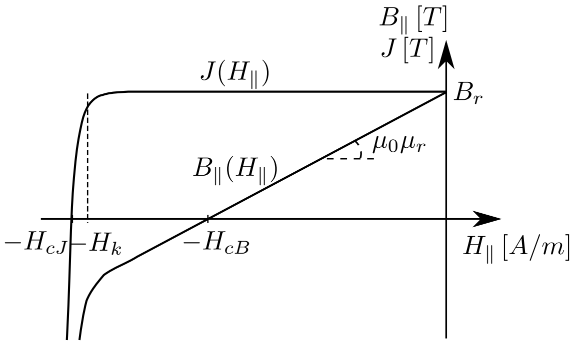

Figure 2.5: $B-H$ and $J-H$ curve of PM material. B_r: the remanence, H_{cJ}: the coercivity of the polarization J, H_k the knee point of the demagnetization and H_{cB} the coerivity of the magnetic flux density.

Figure 2.5 shows the evolution of the $J-H$ and $B-H$ curves. They are characterized by some specific points, i.e. the remanence B_r, the coercivity of the polarization H_{cJ} and the coercivity of the magnetic flux density H_{cB}. In addition, they can be divided in two domains [84]:

- a domain of reversible demagnetization, in which the magnetic flux density decreases slowly for magnetic field $H_{\parallel}$ higher than $-H_k$;
- a domain of irreversible demagnetization, in which the magnetic flux density decreases drastically for magnetic field $H_{\parallel}$ lower than $-H_k$.

Different approximations of the $J-H$ curve can be found in the literature [82, 83]. In these papers, a piecewise linear curve is used. The linear interpolation of the polarization norm $J = \left|\vec{J}\right|$ is represented in Fig. 2.6 and expressed by:

$$\left|\vec{J}\right| = \begin{cases} B_r & \text{for} \quad -H_k \leq H_{\|} \\ \frac{B_r}{H_{cJ}-H_k}(H_{cJ}+H_{\|}) & \text{for} \quad -(2H_{cJ}-H_k) < H_{\|} < -H_k \\ -B_r & \text{for} \quad H_{\|} \leq -(2H_{cJ}-H_k) \end{cases} \tag{2.2}$$

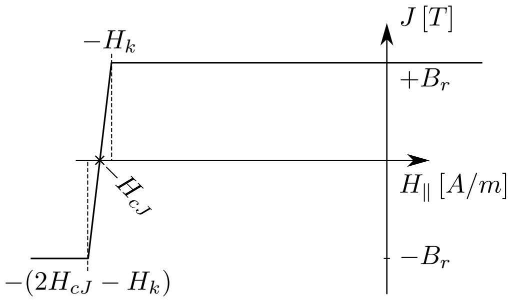

Figure 2.6: The piecewise linear curve of the $J-H$ curve.

No hysteresis model is implemented. Consequently, the recoil curve cannot be estimated.

2.2.2 Temperature effect

The remanence B_r and coercivity H_{cJ-B} of PM decrease with an increasing temperature as illustrated in Fig. 2.7. In [85], authors show that both quantities are dependent on temperature and can be represented using a second order polynomial equation. From PM manufacturer [65], only a linear coefficient is given and expressed in $[\%/K]$:

- the temperature coefficient of the remanence α_{B_r};
- the temperature coefficient of the coercivity α_H, identical for both the coercivity of the polarization and the coercivity of the magnetic flux density.

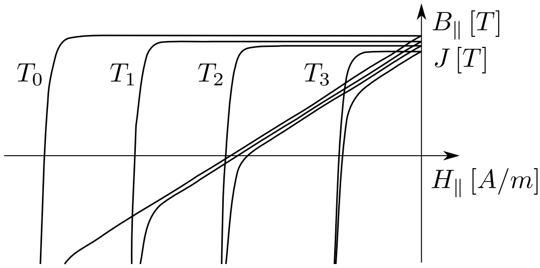

Figure 2.7: $B-H$ and $B-J$ curve of PM material subject to different temperatures: $T_0 < T_1 < T_2 < T_3$.

Finally the evolution with the temperature of the remanence and coercivity can be expressed by:

$$\begin{aligned} B_r =& B_{r,20\,^\circ C}\left(1-\alpha_{B_r}\frac{T-20\,^\circ C}{100}\right) \\ H_k =& H_{k,20\,^\circ C}\left(1-\alpha_{H}\frac{T-20\,^\circ C}{100}\right) \\ H_{cJ} =& H_{cJ,20\,^\circ C}\left(1-\alpha_{H}\frac{T-20\,^\circ C}{100}\right) \end{aligned} \tag{2.3}$$

2.2.3 Finite element model implementation

In order to evaluate the impact of the demagnetization and the temperature on the performance of a PM bearing, constitutive equations (2.1), (2.2) and (2.3) are implemented into a FE software. In addition, the model also considers:

- an isotropic relative permeability for all the materials,
- a linear ferromagnetic material.

Practically, the FE model is implemented in COMSOL, the magnetic field is solved by the scalar magnetic potential and the axial force is evaluated by integration of the Maxwell stress tensor. To reduce the computation time, the model benefits from the axial and plane symmetries of the system.

Table 2.2: Dimensions and properties of the PM rings (N38H grade)

	Parameter	Value
D	Outer PM diameter	$50\,mm$
d	Inner PM diameter	$30\,mm$
h	PM height	$5\,mm$
$B_{r,20\,^\circ C}$	Remanence	$1.24\,T$
$H_{k,20\,^\circ C}$	Coercivity: knee point	$1380\,kA/m$
$H_{cJ,20\,^\circ C}$	Polarization coercivity	$1420\,kA/m$
$\mu_{r_{PM}}$	PM relative permeability	1.0588
α_{B_r}	Temperature coefficient of remanence	$0.115\,\%/K$
α_H	Temperature coefficient of coercivity	$0.58\,\%/K$
T_{max}	Maximal working temperature	$120\,^\circ C$

To illustrate the model, an application case is presented with two opposed PM rings with axial polarization mounted with a soft magnetic material on the back. The dimensions of the iron core are given in Fig. 2.8.a and the dimensions and properties of the PM rings are in Table 2.2. Figure 2.8.b shows the FE model with its symmetries, the contour used to perform the Maxwell stress integration, and the mesh for an airgap of $2.6\,mm$. The relative permeability of iron is supposed to be isotropic and equal to 5000.

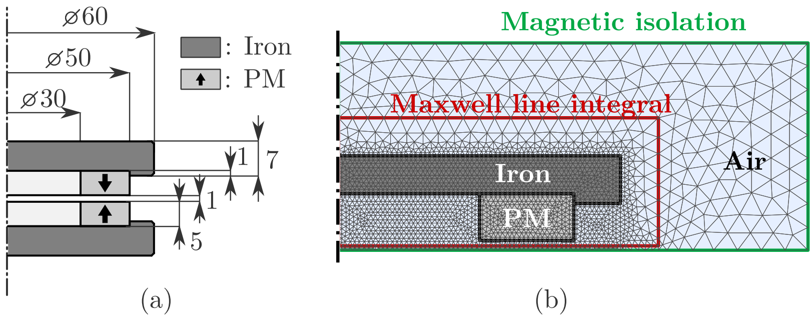

Figure 2.8: (a) Dimensions of iron core and PM rings and (b) FE model and mesh for an airgap of $g = 2.6\,mm$.

The axial force F_z is evaluated for different values of temperature and airgap thickness:

$$F_{z,ij} = function(T_i, g_j) \tag{2.4}$$

with T_i the temperature ranging from $20\,°C$ to $140\,°C$ by steps of $5\,°C$ and g_j the airgap from $0.2\,mm$ to $3.8\,mm$ by steps of $0.1\,mm$. The results are given in Fig. 2.9 for four particular airgap values. As expected, the magnetic force increases with the airgap thickness reduction and decreases with the temperature. It is observed that the magnetic force decrease abruptly for high temperature due to irreversible demagnetization effect.

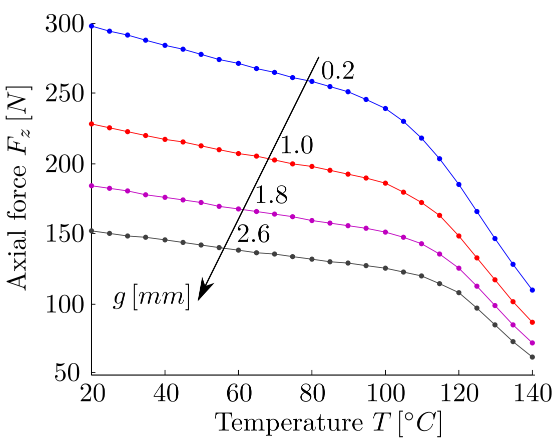

Figure 2.9: (a) Evolution of the axial force with the temperature from $20\,°C$ to $140\,°C$ by step of $5\,°C$ for different air gap g.

Based on these values of the axial force $F_{z,ij}$, a linear interpolation can be made to deduce from a temperature T' and an axial force F'_z the corresponding airgap g':

$$g' = f'(T', F'_z) \tag{2.5}$$

This function is used latter to compare the FEM with the experimental results.

2.2.4 Experimental validation

Test bench description

To validate the FE model, a test bench shown on Fig. 2.10 has been realized. The detailed cross-section view of the system is shown in Fig. 2.11. The test bench allows to observe the evolution of the distance between two identical PM rings with axial but opposite polarization with regards to the axial force F_z and the temperature T. Each ring is mounted with a soft magnetic materials on the back. One ring is fixed on the static part and the other on a shaft radially guided by air bearings. The airgap thickness is measured by a non-contact capacitive displacement sensor. The axial force remains constant for each test by applying different masses. The complete test bench is placed in a temperature controlled oven.

Figure 2.10: On the left side, the test bench and on the right side the PM rings.

The dimensions and properties of the PM rings are given in Table 2.2. The properties correspond to a N38H grade material (NdFeB). A centering diameter $\varnothing 50\,mm$ of $1\,mm$ deep is machined on the rotor and stator iron core.

The accuracy strongly depends on the temperature measurement, which can be problematic in practice because of two reasons. First, due to the temperature increase and the pressurized air injected by the air bearing, the temperature is not uniform and therefore is not the same for the two PM rings. Secondly, this temperature cannot be directly taken on the PM rings. In order to improve the quality of the measurement, different temperature sensors (thermocouple) are placed close to the rotor and stator PM rings on the iron core as shown in Fig. 2.11. The oven temperature is slowly increased to maintain the maximum temperature difference between both sensors around $5\,°C$. For the example, the measured temperature during one cycle is given in Fig. 2.12.a and the difference between the two sensors is given in Fig. 2.12.b. Moreover the air flow in the air

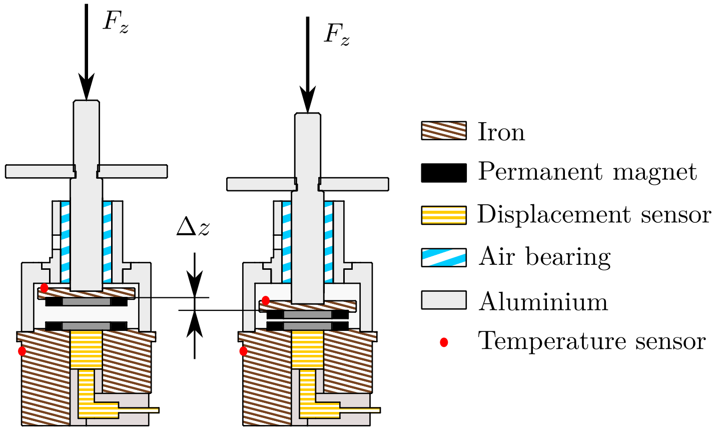

Figure 2.11: Schematic drawing of the bench test used to evaluate the axial distance z between the 2 PM rings. The axial force F_z is constant and is imposed by different masses. The bench test is placed in a oven and the temperatures vary form $20\,°C$ to $130\,°C$.

bearing is limited to the minimum required so as to minimize its impact on the PM temperature. Eventually, the PM temperature is supposed to be equal to the temperature of the rotor sensor.

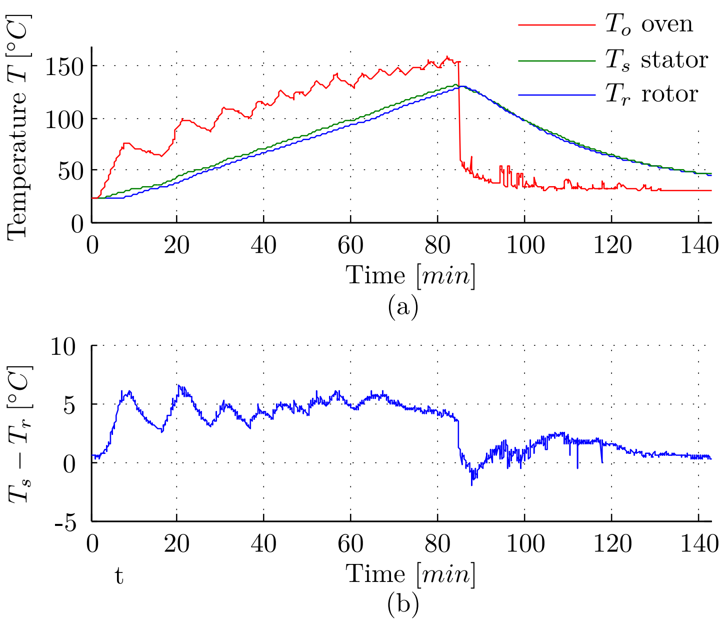

Figure 2.12: (a): Measured temperature inside the oven, on the rotor and stator iron core. (b): Difference between the rotor and stator measured temperature.

Results

Figure 2.13 shows the evolution of the axial force with the airgap thickness at room temperature ($20\,°C$) obtained from both the FE simulations and the experimental measures. As expected, the axial force decreases when the airgap thickness increases and it shows a very good agreement between FE results and experiments.

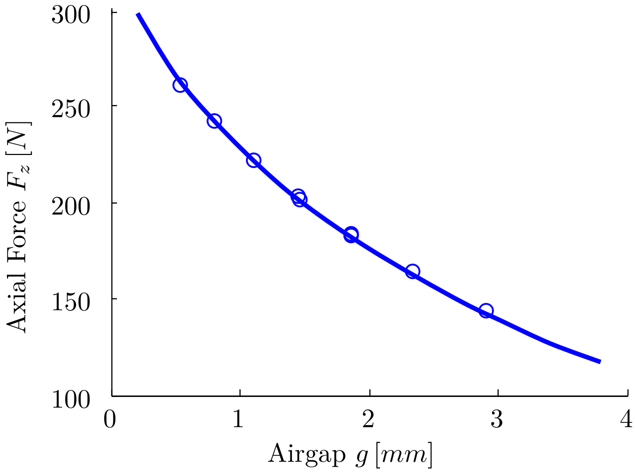

Figure 2.13: Evolution of the axial force in function of the airgap at room temperature of $20\,°C$. Solid line: FE results. Points: experimental results

The evolution of the airgap thickness with the temperature obtained from both the FE simulations and the experimental measures, is shown in Fig. 2.14, for an imposed constant axial force on the PM rings. Each curve, illustrating the behaviour for different imposed axial loads, has been measured with a new unaltered couple of identical PM rings. The experiment and the simulations give good agreement, except at the knee point when the operating point of the PM corresponds to the knee point of the $J-H$ curve. This difference is a priori due to the model of the demagnetization curve (2.2). The latter is done by piecewise linear interpolation as explained in section 2.2. This interpolation overestimates the value of the remanence in the knee point region leading in an overestimated axial force in the model, which means a higher airgap. Nevertheless, the FE results are good enough to predict the demagnetization behaviour.

Finally, an experiment is performed to show the recovery curve after different temperature cycles while keeping the same couple of PM rings. The results are presented in Fig. 2.15 and show the evolution of the airgap thickness g with the temperature T for a constant axial force of $F_z = 123\,N$. A first cycle is done in the reversible region where the maximal temperature is $T = 90\,°C$. A second cycle reaches a temperature of $T = 120\,°C$ and the recovery curve is slightly lower than the initial curve. Cycles 3 and 4 reach respectively a temperature of

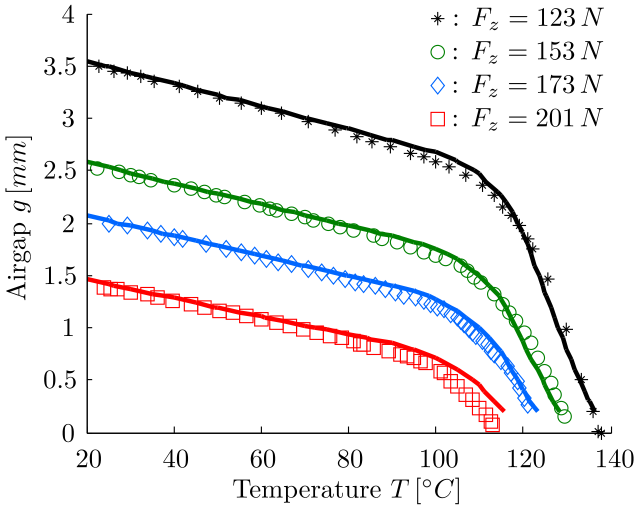

Figure 2.14: FE (solid line) and experimental (points) results of the evolution of the airgap thickness g with an increasing temperature T for different constant axial forces F_z.

$132\,°C$ and $136\,°C$.

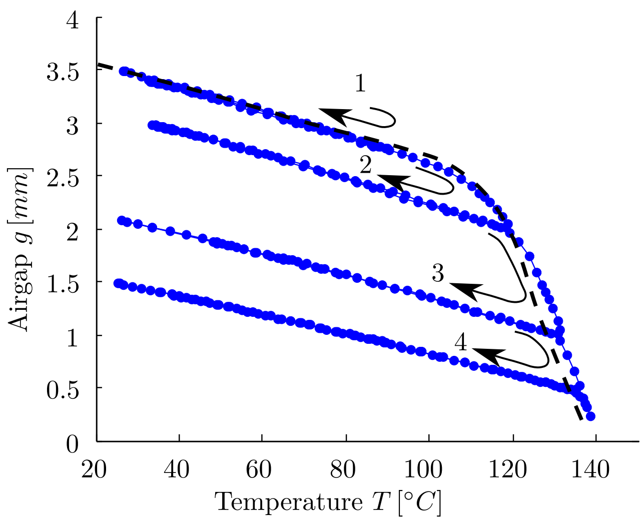

Figure 2.15: Evolution of the airgap thickness with the temperature for a constant axial force $F_z = 123\,N$. The temperature is increased and decreased in 4 different cycles. The cycle 1 stays in the reversible demagnetization region ($T < 90°C$). Cycles 2, 3 and 4 are subject to irreversible demagnetization. In dashed line, FE results.

The model presented in this section is validated for neodymium magnets and predicts correctly their demagnetization behaviour. For the next section, the same model is used for the other PM materials.

2.3 Discussion

Based on the FE model, different PM materials are compared comprising ferrite, alnico, neodymium and samarium cobalt magnet. First, the PM properties are given. Secondly, the influence of the temperature effect on the axial force is observed for the different materials. Thirdly, the risk of irreversible demagnetization in the PM material is considered. The influence of the selected topology on the risk is also studied.

2.3.1 Material properties

In Table 2.3, the properties of particular PM material used for this comparison are given. The considered PM material are ferrite (ceramic), alnico, samarium cobalt $SmCo$ and neodymium iron bore $NdFeB$ magnets. Due to the large use of rare-earth magnets ($SmCo$ and $NdFeB$) in magnetic bearings, different grades of sintered magnets are considered. The $SmCo$ has two main phases $SmCo_5$ and Sm_2Co_{17}. The latter gives higher remanence but is more expensive. The $NdFeB$ magnet is composed of a variety of grade. In order to better represent the different grades, a classic N35 grade is chosen. This grade corresponds to quite low remanence and coercivity. It is compared to grade N50 with a higher remanence but same coercivity. The addition of dysprosium element allows to increase the coercivity but decrease the remanence. This leads to N35UH grade with same remanence as N35 but higher coercivity and therefore higher maximal temperature. Finally, with the grain boundary diffusion process, either the remanence and the coercivity are increased leading in GB50UH grade.

The values given in Table 2.3 are obtained from PM manufacturers (Vacuumschmelze, Arnold Magnetic Technologies and HKCM Engineering) [64–66] and from the literature [70, 86]. Figure 2.16.b shows the BH curves of the different considered PM material. They are compared to equivalent curves obtained in Vacuumschmelze catalogue (see Fig. 2.16.a).

It is important to note that the values obtained from PM manufacturers are subject to uncertainties due to the production process. A deviation of 3% to 5% can be observed.

2.3.2 Impact of the temperature effect

The aim of this part is to discuss the influence of the temperature on the performance of the PM materials when the latter are used in PMTB. The

Table 2.3: Properties of the main PM material exrtact from different PM manufacturers [64–66] and from the litterature [70, 86].

	BH_{max} $[kJ/m^3]$	B_r $[T]$	H_k $[kA/m]$	H_{cj} $[kA/m]$	H_{cB} $[kA/m]$
Ferrite	30	0.4	250	275	265
Alnico	40	1.2	110	120	120
$SmCo_5$	160	0.9	1600	1960	700
Sm_2Co_{17}	255	1.1	1200	1700	840
$NdFeB$ (N35)	280	1.2	1100	1130	925
$NdFeB$ (N50)	400	1.42	990	1000	990
$NdFeB$+Dy (N35UH)	280	1.2	1920	2000	900
$NdFeB$+Dy (GB50UH)	390	1.4	2250	2500	1050

	α_{B_r} $[\%/°C]$	α_H $[\%/°C]$	T_{max} $[°C]$	Price (relative)
Ferrite	-0.2	+0.3	450	1
Alnico	-0.02	-0.01	500	5
$SmCo_5$	-0.04	-0.3	250	25
Sm_2Co_{17}	-0.03	-0.25	350	35
$NdFeB$ (N35)	-0.11	-0.6	80	10
$NdFeB$ (N50)	-0.11	-0.6	60	25
$NdFeB$+Dy (N35UH)	-0.11	-0.5	180	25
$NdFeB$+Dy (GB50UH)	-0.11	-0.5	180	25

reversible and irreversible demagnetization effect are considered. The dimensions of PM rings and the conditions of simulation are exactly the same than in Sections 2.2 (see Fig. 2.8).

Figure 2.17 shows the evolution of the axial force with the temperature for different airgap thicknesses. The solid-line curves represent the predicted axial force when considering irreversible demagnetization and in dashed-line, when considering the demagnetization curves without the irreversible effects. The maximal recommended working temperature is given with the vertical black line.

It is observed in Fig. 2.17 that rare-earth (RE) and classical magnet (ferrite and alnico) have different behaviours. In first observation, the force develops by the classical magnet is 10 times smaller than the force of RE magnet. This behaviour is explained by the difference of the maximal energy product BH_{max} available for each PM material. Indeed, the BH_{max} of RE magnets is around 10 times bigger than for the classical magnets. For the ferrite magnets, this difference is explained by a difference in the remanence. For the alnico magnets, their remanence is equivalent to the one of rare-earth magnet but due to low coercivity, they have their working point in the irreversible region. A

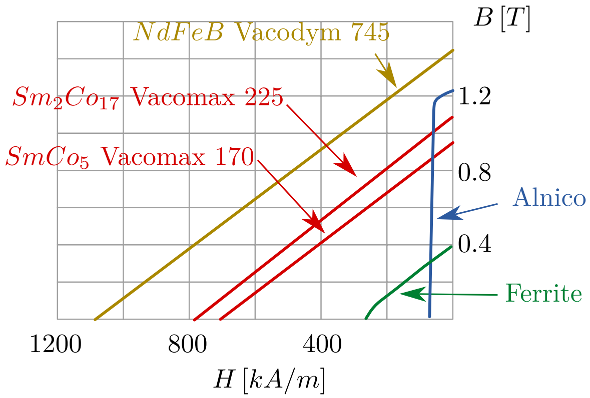

(a)

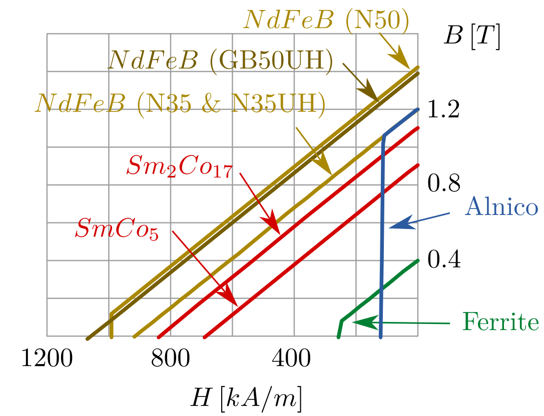

(b)

Figure 2.16: Demagnetization curves of various material (a) from Vacuumschmelze catalogue [64] and (b) from the values of Table 2.3.

second observation is that the dashed-lines do not appear for classical magnet. The ferrite magnets withstand very well the irreversible demagnetization due to temperature effect. Consequently, the solid-lines and the dashed-lines are superposed. For the alnico magnet, the axial force without irreversible demagnetization is much higher than the effective force. Indeed as explained, alnico magnet presents similar remanence as RE magnet ($B_r = 1.1\,T$) but has their working point in the non-linear region between H_{cj} and H_k leading in a large difference between the two curves (the dashed-lines are out of the figure size). Actually, using this kind of model for alnico magnet do not represent correctly the physics but is good enough for a basic comparison.

The temperature where the two curves diverge (solid and dashed lines) is called the irreversible temperature T_{irr}. Its value changes for each airgap thickness

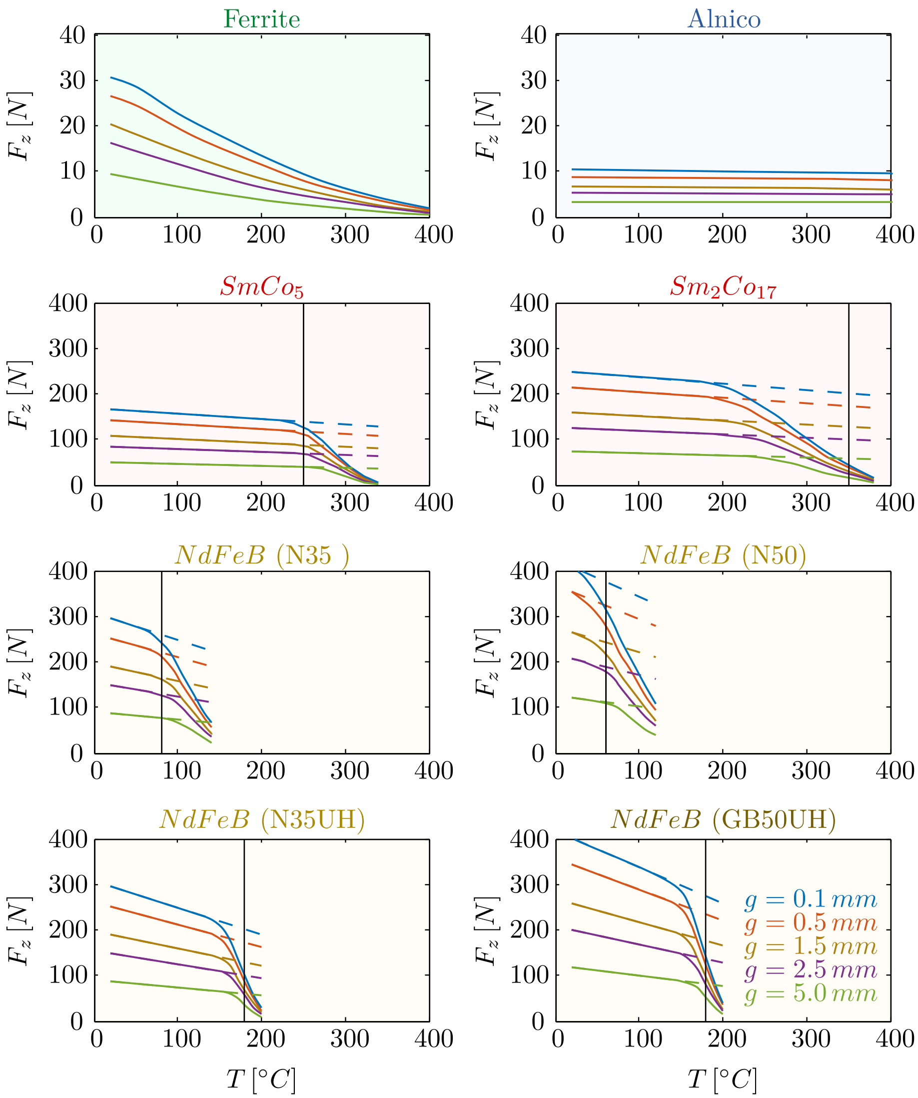

Figure 2.17: Evolution of the axial force with the temperature for 3 different airgap thicknesses $g = [0.1; 0.5; 1.5; 2.5; 5.0]\,mm$ for the different PM material. The maximal recommended working temperature is given with the vertical black line. In dashed line: curve without considering irreversible demagnetization.

and is summarized for the different PM materials in Table 2.4. At this point, the maximal value of the magnetic field of some local regions inside the PM and parallel to the polarization reaches the value of the knee point coercivity: $\max(|H_{\parallel}|) = H_k$. If the temperature is higher than T_{irr}, the PM material is subjected to irreversible demagnetization.

For the ferrite magnet, this point is never reached (represented by a ✔ in the table). For the alnico magnet, the parallel magnetic field $|H_{||}|$ exceeds the knee point H_k (represented by a ✘ in the table). As already explained, the working points of alnico magnets are located in the non-linear region. For the RE magnet, the T_{irr} temperature changes a lot with the PM grades and deserves more explanations.

Table 2.4: Temperature T_{irr} before irreversible demagnetization for different airgap thickness and for the different PM materials.

Airgap thickness	Temperature before irreversible demagnetization T_{irr} [°C]			
$g\,[mm]$	Ferrite	Alnico	$SmCo_5$	Sm_2Co_{17}
0.5	✓	✘	225	175
1.5	✓	✘	235	192
2.5	✓	✘	245	200
		$NdFeB$		
$g\,[mm]$	N35	N50	N35UH	GB50UH
0.5	65	25	140	145
1.5	70	30	145	150
2.5	75	35	150	155

Firstly, the parameters that influence the temperature T_{irr}, are studied. This temperature T_{irr} where the PM material becomes irreversibly demagnetized, depends on:

- an external applied magnetic field $H_{||}$,
- the PM properties.

In the case of PMTB, the increase of the external magnetic field $H_{||}$ happens when the airgap thickness decreases. In Table 2.4, we observed that both the temperature and the airgap thickness have an impact on the irreversible demagnetization. This means that even at low temperature, there is a risk of irreversible demagnetization and this risk is strongly dependent on the PM material and more specifically on the coercivity knee point value H_k.

Secondly, the temperature T_{irr} is compared with the maximum working temperature T_{max} suggested by the PM manufacturer. As observed, the temperature from PM manufacturers T_{max} (vertical black line) is less restrictive than the temperature T_{irr} (points where dashed-line and solid-line diverge). The difference is due to the fact that the temperature from PM manufacturers is applicable for specific conditions that can be less restrictive than in PMTB. Consequently, a model where both reversible and irreversible effects, is needed to safely design PM bearings for applications with high or variable operating temperature.

Thirdly, the comparison between the $SmCo$ and $NdFeB$ materials is done in the two regions: in the reversible regions ($T < T_{irr}$) and in the irreversible region ($T > T_{irr}$).

For the reversible region, the temperature has less impact on the $SmCo$ material than on the NdFeB. Indeed, the axial force depends on the square of the polarization [35], with $J_{\|} = B_r$ leading to:

$$\begin{aligned} F_{z,T} &= F_{z,20^\circ C}\left(1 - \alpha_{B_r}\frac{T - 20^\circ C}{100}\right)^2 \\ &\approx F_{z,20^\circ C}\left(1 - 2\,\alpha_{B_r}\frac{T - 20^\circ C}{100}\right) \end{aligned} \tag{2.6}$$

The temperature coefficient of remanence α_{B_r} for the $SmCo$ is approximatively 3 times smaller than the coefficient of the $NdFeB$. Consequently, the influence of the temperature on the force is approximatively 3 times smaller for $SmCo$ than for $NdFeB$.

For the irreversible region, we observe that $SmCo$ decreases slowly with the temperature in comparison to the $NdFeB$. Actually, the range of temperature during the irreversible demagnetization is:

- large for samarium cobalt PM: $> 100°C$,
- small for neodymium iron boron: $< 100°C$.

This is explained by the ratio H_k/H_{cj} and the temperature coefficient of coercivity α_H. $NdFeB$ have higher value of H_k/H_{cj} than $SmCo$. This means that the irreversible demagnetization is abrupt inside the $NdFeB$. Moreover, they have bad resistance to irreversible demagnetization with the temperature. The coefficient α_H is approximatively 3 times greater for $NdFeB$ than for $SmCo$. Consequently, the risk of abrupt irreversible demagnetization is important for the $NdFeB$ magnet and some care has to be taken when this kind of PM are used inside applications presenting peaks of temperature. In opposite, even if $SmCo$ are subject to irreversible effect leading in a diminution of the performance, the risk of abrupt demagnetization is lower.

Finally, to illustrate the demagnetization process, Fig. 2.18 shows the local polarization $|\vec{J}|$ obtained from the FEM for all materials with a constant airgap thickness $g = 1.5\,mm$, while increasing the ambient temperature. In the regions subjected to reversible demagnetization, represented by light grey color, the polarization is uniform and the axial force temperature dependence respects (2.6). The PM are also subject to local irreversible demagnetization, which is represented in graduated color. For this kind of PM thrust bearing, with only one couple of PM rings facing each other and presenting a back iron yoke, the irreversible demagnetization happens starting from the center of the PM, on the airgap side. The effect of the back iron yoke is also visible on the external side of the PM, next to the $1\,mm$ deep centering diameter. This corner is the last one to be subject to irreversible demagnetization.

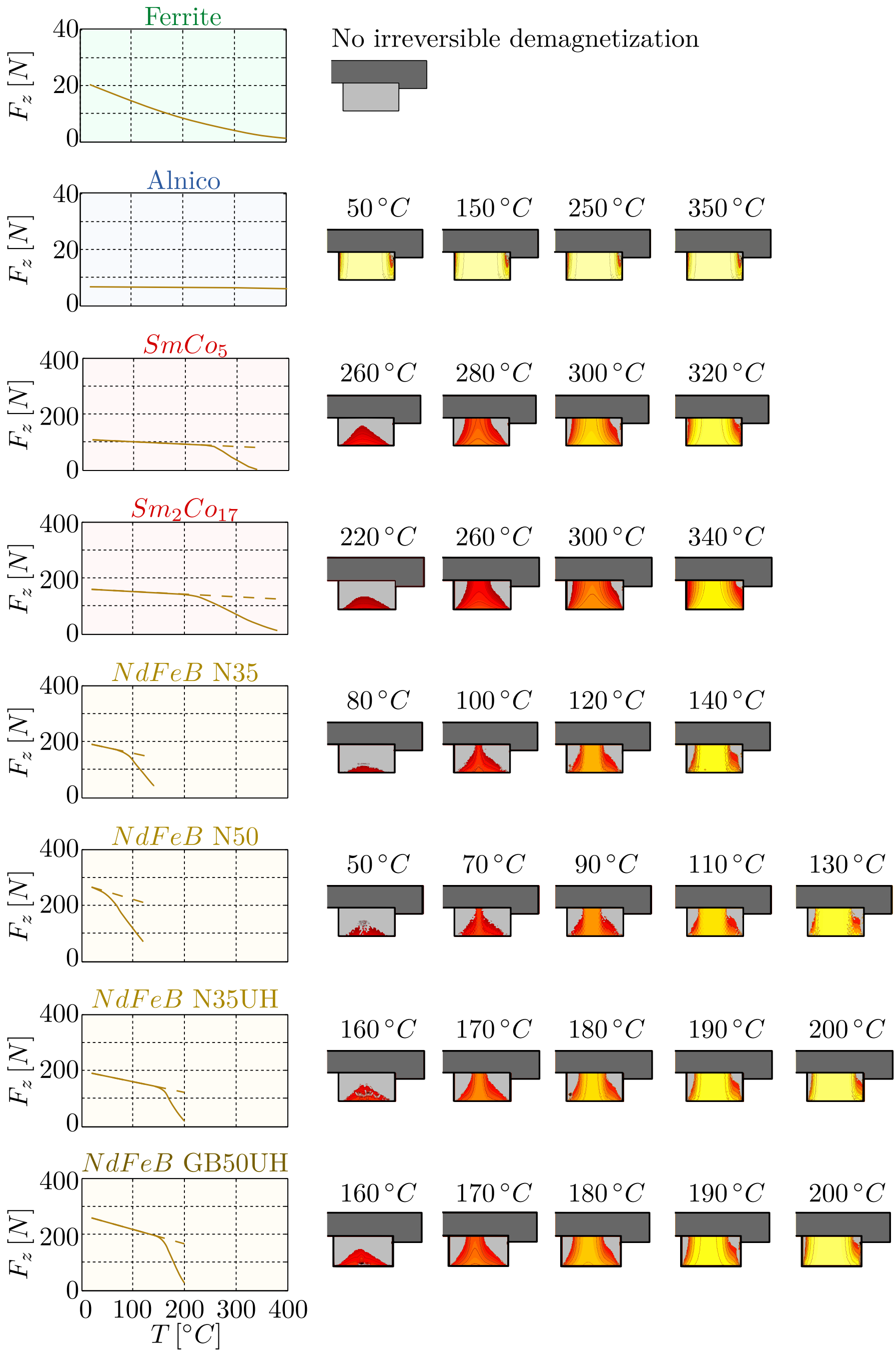

Figure 2.18: Amplitude of the local polarization $|\vec{J}|$ with reversible and irreversible demagnetization zone for different temperature T and a constant airgap tickness $g = 1.5\,mm$. The legend is given in Fig. 2.19.

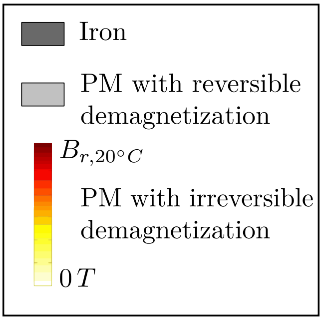

Figure 2.19: Legend of Fig. 2.18. The regions subjects to reversible demagnetization is represented by light grey color, the iron is in dark gray and the zone subject to irreversible demagnetization is in graduated color.

2.3.3 Irreversible demagnetization risk with topology consideration

The aim of this part is to discuss about the risk of irreversible demagnetization and to study the influence of the selected PMTB topology on this risk. The irreversible demagnetization in PM material depends on the external applied magnetic field $H_{\parallel}$ and on the PM properties: the knee point coercivity H_k. This is represented on the $B-H$ curve as shown in Fig. 2.20 with the load lines. The latter are dependent on the equivalent relative permeability $\mu_{r,eq}$ of the magnetic circuit seen by the PM, defined as:

$$B_{\parallel} = -\mu_0 \mu_{r,eq} H_{\parallel} \tag{2.7}$$

By comparing the value of the equivalent relative permeability to its limit value $\mu_{r,eq}^{limit}$, it is possible to predict the risk of irreversible demagnetization. For instance, point a, b and c are in the reversible region for an equivalent relative permeability of 4, 2 and 1 respectively and point d and e are in the irreversible region with $\mu_{r,eq} = 0.5$ and $\mu_{r,eq} = -0.25$ respectively.

The limit equivalent relative permeability is obtained by first, solving the PM material constitutive equation in the reversible region and the equivalent load line equation:

$$\begin{cases} B_{\parallel} = \mu_0\, \mu_{r,PM}\, H_{\parallel} + B_r \\ B_{\parallel} = \mu_0\, \mu_{r,eq}\, H_{\parallel} \end{cases} \Rightarrow \quad H_{\parallel} = -\frac{B_r}{\mu_0(\mu_{r,PM} + \mu_{r,eq})} \tag{2.8}$$

with $\mu_{r,PM}$ the relative permeability of the PM ; and then, by imposing that the reverse parallel magnetic field equal the knee point coercivity ($H_{\parallel} = -H_k$):

$$\mu_{r,eq}^{limit} = \frac{B_r}{\mu_0\, H_k} - \mu_{r,PM} \tag{2.9}$$

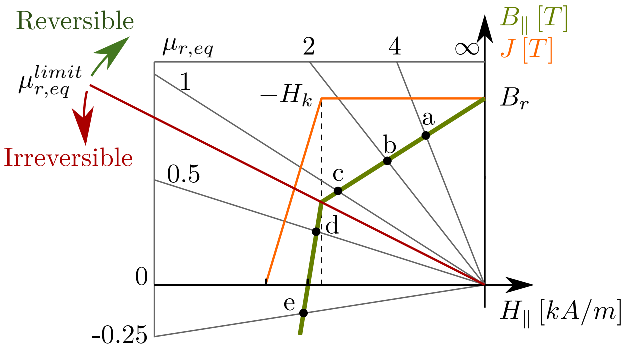

Figure 2.20: BH curve of PM material with load lines of equivalent magnetic circuits.

This result shows that the $\mu_{r,eq}^{limit}$ is only dependent on the PM properties. The condition to be in the reversible region is therefore:

$$\overbrace{\mu_{r,eq}^{limit}}^{\text{PM properties}} \leq \overbrace{\min(\mu_{r,eq})}^{\text{Magnetic circuit}} \Rightarrow \text{Reversible region} \tag{2.10}$$

where $\min(\mu_{r,eq})$ is the minimum value of the equivalent relative permeability inside the PM. This value is dependent on the magnetic circuit and is a local quantity. In order to illustrate this concept, the equivalent relative permeability defined in (2.7) is shown in Fig. 2.21 for axially stacked topology with axial polarization and without iron. The dimensions are given on the figure and the results are obtained by a 2D plane finite element model implemented in COMSOL for a rigid and uniform polarization of $1\,T$. The model takes benefit of the anti-periodicity.

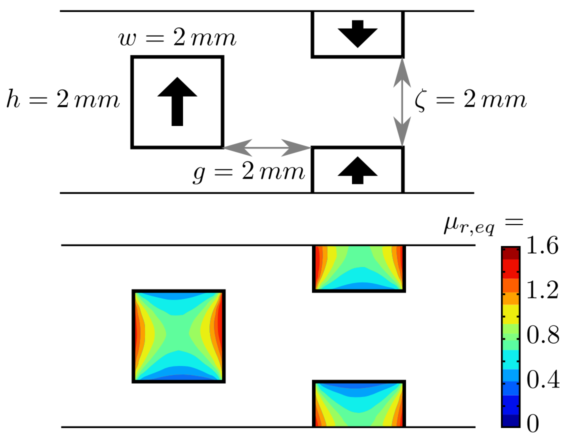

Figure 2.21: Local equivalent relative permeability for axially stacked topology with axial polarization and without iron for a rigid and uniform remanence of $B_r = 1\,T$. The minimum value is $\min(\mu_{r,eq}) = 0.28$.

Figure 2.21 shows that the $\mu_{r,eq}$ is indeed a local quantity inside the PM. The PM area the most subject to irreversible demagnetization is located in the blue region where the equivalent relative permeability is the smallest. This corresponds to the upper and lower area in the direction of the polarization where two adjacent PM are placed in opposition.

The comparison between the limit permeability $\mu_{r,eq}^{limit}$ arising from given PM material and the minimum local permeability $\min(\mu_{r,eq})$ inside a given device with a specific geometry gives a good indication of the risk of demagnetization. However this comparison necessitate a model.

When considering the case of PMTB, and if constructing the model by assuming the following hypotheses:

- the magnetic field is evaluated in a 2D plane model,
- the relative permeability of the PM $\mu_{r,PM}$ is equal to 1,
- the polarization is uniform and rigid.

the minimum equivalent relative permeability $\min(\mu_{r,eq})$ is independent on the PM properties and dependent only on the ratio between the PM dimensions i.e. height h, width w and gap between PM ζ, and the airgap thickness g:

$$\min(\mu_{r,eq}) = \hat{\mu}\left(\frac{h}{g}, \frac{w}{g}, \frac{\zeta}{g}\right) \tag{2.11}$$

where $\hat{\mu}$ is a dimensionless quantity.

To support this assumption, Fig. 2.22 shows the evolution of $\min(\mu_{r,eq})$ for different value of relative PM height $\frac{h}{g}$ and width $\frac{w}{g}$. For the convenience, the gap between the PM is equal to the section height $\frac{\zeta}{g} = \frac{h}{g}$. The topology and simulation conditions are the same than for Fig. 2.21. This evolution is shown for four different cases: with airgap thicknesses of $1\,mm$, $2\,mm$ and $4\,mm$ and a remanence B_r of $1\,T$, and for an airgap thickness of $1\,mm$ and a remanence of $1.4\,T$. As observed in Fig. 2.22, the four different cases give exactly the same solution.

As shown in Chapter 1, the optimal dimensions of PM section are also independent on the PM properties. This means that at the optimum, the minimum equivalent relative permeability is a constant regardless of the PM properties, the airgap thickness and the intended magnetic force. Based on (2.10), the risk of irreversible demagnetization in relation to the topology selection and PM material choice can be systematized:

$$\frac{B_r}{\mu_0\, H_k} - 1 \leq \hat{\mu}_{opt} \tag{2.12}$$

where $\hat{\mu}_{opt}$ is the minimum value of the equivalent relative permeability at the optimal PMTB dimensions. To take into account a variation of the operating

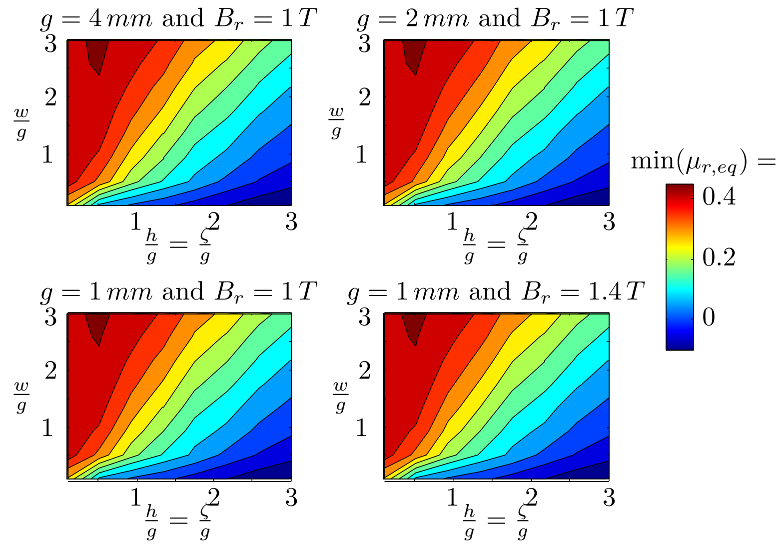

Figure 2.22: Evolution of the minimum equivalent relative permeability $\min(\mu_{r,eq})$ with ratio of the PM section dimensions on the airgap thickness: height $\frac{h}{g}$, width $\frac{w}{g}$ and gap between PM $\frac{\zeta}{g}$. The result is shown for four cases. The topology is the axial stack with axial polarization without iron.

temperature, (2.12) can be generalized as the remanence and the coercivity depend linearly on the temperature (2.3):

$$\begin{aligned} \frac{B_{r,T}}{\mu_0\, H_{k,T}} - 1 &\leq \hat{\mu}_{opt} \\ \frac{B_{r,20^\circ C}}{\mu_0\, H_{k,20^\circ C}} \left(\frac{1 - \alpha_{B_r} \frac{T-20^\circ C}{100}}{1 - \alpha_H \frac{T-20^\circ C}{100}} \right) - 1 &\leq \hat{\mu}_{opt} \end{aligned} \tag{2.13}$$

The value of equivalent relative permeability $\hat{\mu}_{r,eq}$ is shown in graduated color in Fig. 2.23 for the different topologies selected in Chapter 1 in their optimal dimensions. It is obtained by the 2D plane anti-periodicity FE model for a rigid and uniform polarization. For topology with iron, the iron is represented in gray. The magnetic field lines are in black. For radially stacked topology, the symmetry axis is shown in red line.

Figure 2.23 shows the PM zone the most susceptible to be irreversibly demagnetized (in dark blue) and the minimum value of equivalent relative permeability $\hat{\mu}_{opt}$ is given. Nevertheless due to singularities at sharp edges, Halbach array and induced pole topologies have area where $\hat{\mu}_{r,eq}$ is difficult to evaluate with extreme values. These areas are in white inside the PM on Fig. 2.23. Therefore for these topologies, the $\hat{\mu}_{opt}$ can not be evaluated. However for all the topologies, the area the most susceptible to enter in irreversible demagnetization is in dark blue.

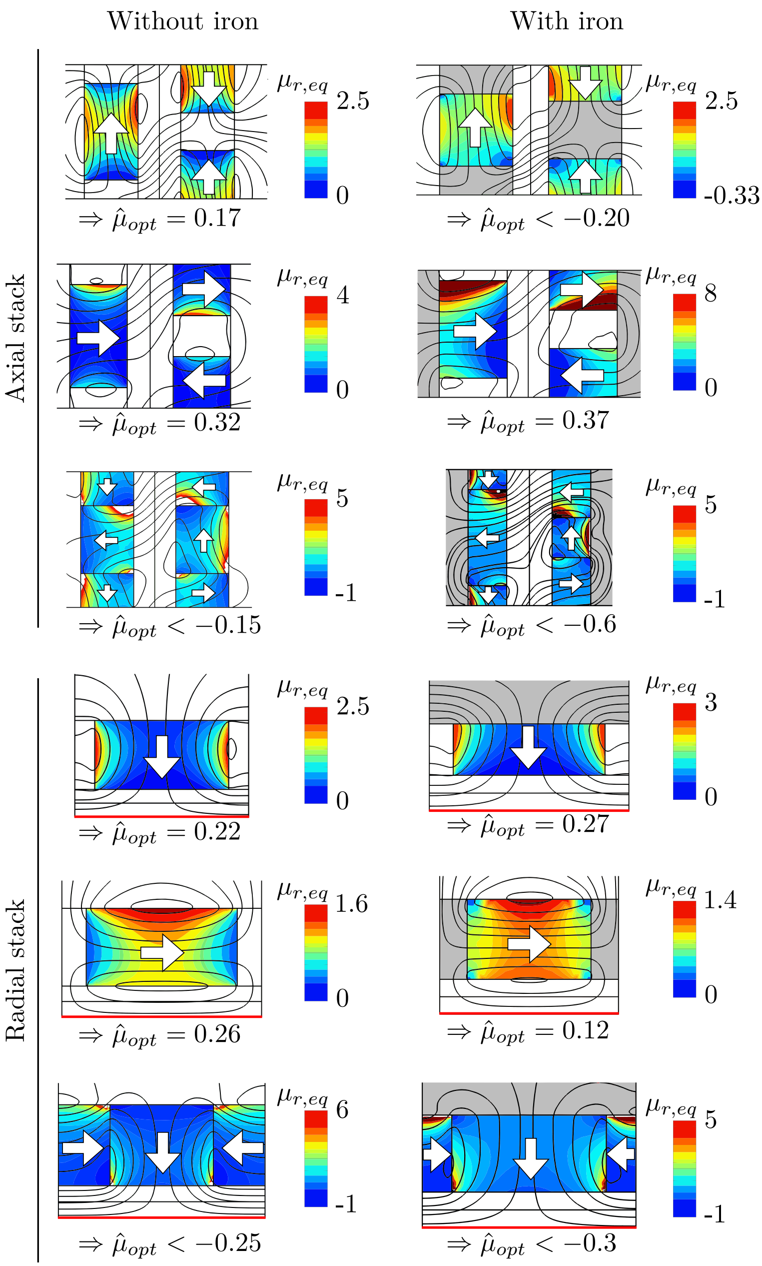

Figure 2.23: Local equivalent relative permeability of the different PMTB topologies selected in Chapter 1 in their optimal configuration. The iron is represented in gray. For the radially stacked topologies, the symmetry axis is in red. The magnetic field lines are in black. For each topology, the minimum value of $\mu_{r,eq}$ is given: $\hat{\mu}_{opt}$.

Table 2.5: Minimal value of the equivalent relative permeability $\hat{\mu}_{opt}$ for all the topologies. This information reflects the ability of a topology to resit irreversible demagnetization of PM material: high value of $\hat{\mu}_{opt}$ means good resistance and low value bad resistance. ✘: topology with singularities.

		Without iron	With back-iron	With induced-pole
Axial stack	Axial polarization	0.17		✘
	Radial polarization	0.32	0.37	
	Halbach array	✘	✘	
Radial stack	Axial polarization	0.22	0.27	
	Radial polarization	0.26		0.12
	Halbach array	✘	✘	

Table 2.5 summarizes the value of $\hat{\mu}_{opt}$ for all the topologies. This information reflects the ability of a topology to resist to irreversible demagnetization of PM material: high value of $\hat{\mu}_{opt}$ means good resistance and low value bad resistance. As observed, the axially stacked with radial polarization and with back-iron gives the most resisting topology. In opposition, all the Halbach array are the least resistant to irreversible demagnetization but the value can not be evaluated. The addition of back-iron structure increases the ability of classical polarization to resist irreversible demagnetization. For the induced-pole topologies, the addition of iron pieces decreases their resistance.

Even though this quantity is very interesting to classify PMTB topologies in terms of resistance to irreversible demagnetization, it gives only an information about local effect and not on the magnetic force. In order to evaluate the effect of irreversible demagnetization on the PMTB performance, an optimization of the selected topologies of Chapter 1 is performed where the demagnetization effect is considered. The optimization conditions are the same as the one presented in Chapter 1. The optimization is done for different values of knee point coercivity H_k.

The result of the optimization for the axially stacked topology with axial polarization and without iron is given in Fig. 2.24. It shows the evolution of the dimensionless optimal volume $\hat{V}$ defined in (1.21) with the limit equivalent relative permeability $\mu_{r,eq}^{limit}$ defined in (2.9). The value of $\hat{V}$ obtained in Chapter 1 for an optimization with rigid and uniform polarization is 14.53. This optimal dimensionless volume corresponds to value of $\mu_{r,eq}^{limit}$ smaller than the predicted $\hat{\mu}_{opt}$ of 0.17, as given in Table 2.5. If $\mu_{r,eq}^{limit}$ is larger than $\hat{\mu}_{opt}$, the dimensionless coefficient $\hat{V}$ needs to increase in order to compensate the demagnetization effect.

The influence of the ratio between the knee point coercivity and polarization coercivity $\frac{H_k}{H_{cj}}$ is given for three values: 0.5, 0.7 and 0.9. This ratio gives an information on the demagnetization curve shape: if it is close to one, the curve is very sharp, and on the opposite, if it is low, the curve is smooth. A PM material is considered good if the curve is very sharp [87]. As observed on Fig. 2.24, this ratio does not impact the point where the demagnetization effect changes the optimization result but only impacts the gradient of the curve in the demagnetization zone. The best result is for low values of the ratio $\frac{H_k}{H_{cj}}$ which is in opposition with the announced criterion. Actually most of the time, the polarization coercivity is the reference value for demagnetization information. Having a high value of $\frac{H_k}{H_{cj}}$ and in the best case close to 1, gives the highest value of H_k and therefore is consistent with the presented results.

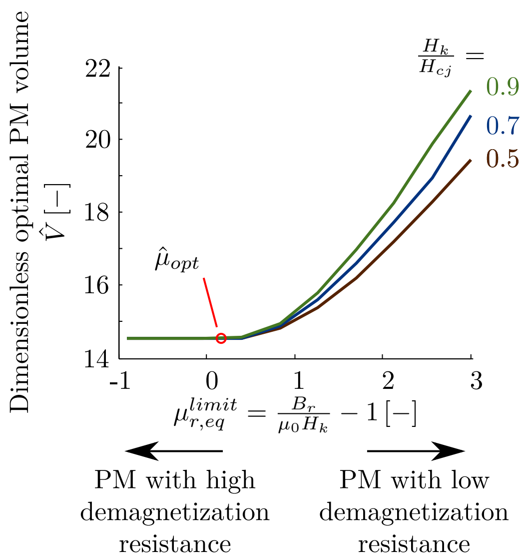

Figure 2.24: Evolution of the dimensionless optimal volume $\hat{V}$ with the limit equivalent relative permeability $\mu_{r,eq}^{limit}$. The results is shown for different values of ratio between knee point coercivity H_k and polarization coercivity H_{cj}. The prediction $\hat{\mu}_{opt}$ based on result of Table 2.5 is shown in red circle.

These results are extended to all the selected topologies of Chapter 1 and are shown in Fig 2.25. The ratio between the knee point coercivity and the polarization coercivity is imposed to $\frac{H_k}{H_{cj}} = 0.8$. The prediction $\hat{\mu}_{opt}$ of demagnetization given in Table 2.5 are represented in red circle. As observed, it predicts correctly the demagnetization effect. Based on this result, $\hat{\mu}_{opt}$ for Halbach arrays and for axially stacked induced pole topologies can be evaluated as shown in green circle. The values are summarized in Table 2.6.

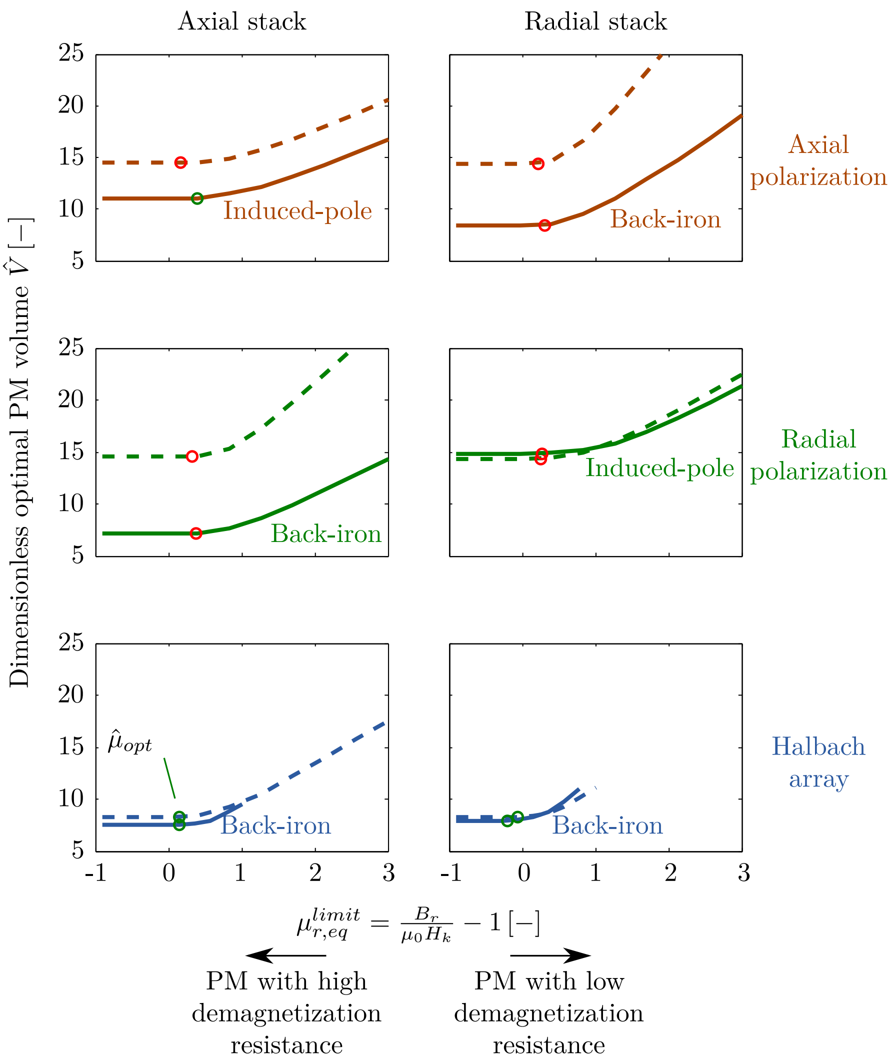

Figure 2.25: Evolution of the dimensionless optimal volume $\hat{V}$ with the limit equivalent relative permeability $\mu_{r,eq}^{limit}$ for $\frac{H_k}{H_{cj}} = 0.8$. The prediction $\hat{\mu}_{opt}$ are in red circle and for topologies with singularities, this prediction is evaluate in green circle. Dashed-line: topologies without iron and solid-line topologies with iron.

A first observation confirms that back-iron structures allows to increase the resistance to demagnetization for topologies with classical polarization. Secondly, the induced-pole topologies give similar performance in term of resistance to demagnetization as topologies without iron. Thirdly, comparing topologies without iron for small values of $\mu_{r,eq}^{limit}$ gives approximatively the same results which is consistent with result of Chapter 1. On the contrary for values of $\mu_{r,eq}^{limit}$ larger than $\hat{\mu}_{opt}$, the behaviour diverges. The topologies where two adjacent superposed PM rings are placed in opposition are more sensitive to demagnetization effect. Finally, the Halbach arrays are the weakest topologies in term of demagnetization effect. For high value of $\mu_{r,eq}^{limit}$, the optimization tends to delete one polarization direction of the Halbach array.

From these results, the minimum equivalent relative permeability $\hat{\mu}_{opt}$ inside a topology are presented in Table 2.6. These values are compared to the limit equivalent relative permeability $\mu_{r,eq}^{limit}$ of PM materials for different operating temperature given in Table 2.7. The comparison is based on (2.13). This example shows that at the optimal dimensions, the choice of PM material is dependent on the choice of topology. For instance, $NdFeB$ N50 grade at ambient temperature of $20°C$ leads to irreversible demagnetization in Halbach array and in opposition, leads to rigid magnetization in classical polarization with or without back-iron.

Table 2.6: Minimal value of the equivalent relative permeability $\hat{\mu}_{opt}$ for all the topologies corrected to take into account global effect. This result is obtained from Fig 2.25.

		Without iron	With back-iron	With induced-pole
Axial stack	Axial polarization	0.17		0.40
	Radial polarization	0.32	0.37	
	Halbach array	0.15	0.15	
Radial stack	Axial polarization	0.22	0.27	
	Radial polarization	0.26		0.12
	Halbach array	-0.06	-0.20	

Table 2.7: The limit equivalent relative permeability $\mu_{r,eq}^{limit}$ of PM materials for different operating temperature.

	$\mu_{r,eq}^{limit}$			
	$20°C$	$50°C$	$100°C$	$150°C$
Ferrite	0.27	0.10	-0.14	-0.32
Alnico	7.68	7.66	7.61	7.57
$SmCo_5$	-0.55	-0.51	-0.43	-0.30
Sm_2Co_{17}	-0.27	-0.21	-0.09	0.08
$NdFeB$ (N35)	-0.13	0.02	0.52	2.38
$NdFeB$ (N50)	0.14	0.35	1.00	3.45
$NdFeB+Dy$ (N35UH)	-0.50	-0.41	-0.13	0.94
$NdFeB+Dy$ (GB50UH)	-0.50	-0.42	-0.13	0.93

The comparison shows that $NdFeB{+}Dy$ GB50UH grade with grain boundary diffusion process leads to interesting possibility with high energy density but also able to withstand demagnetization effect. The samarium cobalt PM give good temperature effect resistance but the results highlight that $SmCo_5$ endure more temperature variation than Sm_2Co_{17}.

An additional interesting information is the ratio between the minimum parallel magnetic field $\min(H_{\|})$ and the knee point coercivity H_k. Based on (2.8), (2.9) and (2.11), this ratio is easily derived:

$$\frac{\min(H_{\|})}{H_k} = \frac{1+\mu_{r,eq}^{limit}}{1+\hat{\mu}_{opt}} \tag{2.14}$$

The demagnetization risk is therefore expressed in percentage of the knee point coercivity. Table 2.8 shows for example this percentage for the radially stacked topology with axial polarization and with back-iron, for different material at different temperature. In order to take some security to avoid irreversible demagnetization risk, a good design rule could be to maintain this ratio below 90%. The result allows to select an appropriate PM material to the topology.

Table 2.8: Percentage of the $\frac{\min(H_{\|})}{H_k}$ ratio for the radially stacked topology with axial polarization and with back-iron, for different material at different temperature.

	$\frac{\min(H_{\|})}{H_k}$			
	$20°C$	$50°C$	$100°C$	$150°C$
Ferrite	100	87	68	54
Alnico	683	682	678	675
$SmCo_5$	35	39	45	55
Sm_2Co_{17}	57	62	72	85
$NdFeB$ (N35)	69	80	120	266
$NdFeB$ (N50)	90	106	157	350
$NdFeB{+}Dy$ (N35UH)	39	46	69	153
$NdFeB{+}Dy$ (GB50UH)	39	46	69	152

An other use of the ratio $\frac{\min(H_{\|})}{H_k}$ is to compare the ability of a topology to withstand demagnetization effect. For the example, Table 2.9 shows this ratio for different topologies and for a PM material grade of $NdFeB$ (N35). As already observed, the Halbach structure is the most sensitive to irreversible demagnetization especially for radially stacked topology.

This result also shows that the capacity of topologies to withstand irreversible demagnetization effect is approximatively equivalent for all topologies except for the Halbach array regardless the topology is radially or axially stacked. This means that all classical topologies have the same behaviour regarding the risk to

Table 2.9: Percentage of the $\frac{\min(H_{\parallel})}{H_k}$ ratio for the $NdFeB$ (N35) at $50°C$ for different topologies.

		Without iron	With back-iron	With induced-pole
Axial stack	Axial polarization	87		73
	Radial polarization	77	74	
	Halbach array	89	80	
Radial stack	Axial polarization	84	80	
	Radial polarization	81		91
	Halbach array	109	128	

enter in irreversible demagnetization region. Nevertheless as shown in Fig. 2.25, the demagnetization sensibility is different depending on the topology and it is shown that axially stacked topologies are more resistant than radially stacked topologies.

2.4 Conclusion

From permanent magnet machine literature, a finite element model is adapted to permanent magnet thrust bearings. This model takes into account the reversible and irreversible demagnetization effect together with temperature effect. It is a quite simple model with some limitations especially by neglecting the influence of the magnetic field perpendicular to the polarization direction. Nevertheless, the model is experimentally validated thanks to a test bench allowing a measure of the airgap thickness evolution with the temperature for different axial forces.

Different PM materials are presented like ferrite, alnico, samarium cobalt and neodymium iron boron PM. For samarium and neodymium PM different grades are considered. Based on the developed model, the PM materials are compared.

A first comparison shows the impact of the temperature on simple permanent magnet thrust bearings. The comparison confirms the classical distinction between materials:

- Ferrite PM generate low magnetic force due to low energy density. With temperature variation, they are not subject to irreversible demagnetization but their magnetic performances drop.
- Alnico PM are very stable with the temperature but due to low energy density generate low magnetic force.
- $SmCo$ PM reach high magnetic force and are stable with temperature.
- $NdFeB$ PM have the greatest energy density. However their behaviour with the temperature is very dependent on the material grade but globally is less stable than $SmCo$ PM.

Additionally, this chapter shows that in applications where temperature or demagnetization effect are critical, sizing PM bearings only based on the maximal temperature suggested by PM manufacturers is not enough. Designers need a more complete model, such as the one presented.

A second comparison shows that the selection of PM material is dependent on the selected topology and on the operating temperature in order to avoid irreversible demagnetization inside the PM material. The criterion to make this selection is based on dimensionless quantities.

Publications related to this chapter:
[88] Van Beneden M, Kluyskens V and Dehez B. "Axial force evaluation in permanent magnet thrust bearings subject to demagnetization and temperature effects". 16th international symposium on magnetic bearings (ISMB16). Beijing, China, 2018.

Passive compensation solution for load relieving application

3

A permanent magnet thrust bearing (PMTB) used as load reliever and combined with mechanical bearing (MB) allows to increase the lifetime and reduce the losses of the global system. For good operation, the repartition of the force between the MB and the PMTB needs to remain constant. Nevertheless in practice, this repartition is sensitive to:

- the temperature,
- the aging of the PM material,
- the mechanical and magnetic tolerance.

In order to prevent a bad repartition of the axial force, a passive compensation system is developed and presented in this chapter. This passive system is based on pneumatic or hydraulic jack.

In section 3.1, the problematic of combining PMTB and MB is developed. Then, the state of the art of existing solutions is presented in section 3.2. The proposed solution is given in section 3.3. A model, described in section 3.4, is derived to evaluate the impact of the proposed passive compensation solution on the global system. These results are gathered in section 3.5.

3.1 Problematic

Permanent magnet (PM) thrust bearings (PMTB) are compact systems able to generate high axial forces. Combining mechanical bearing (MB) with magnetic bearings in applications subject to high load increases the life time and reduces the losses of the global system [89]. The function of the MB is to locate the shaft. The function of PMTB is to bear the high axial force of the system. Its contribution to guidance and to stabilizing or destabilizing aspects is insignificant, as its stiffness is much lower than the MB stiffness.

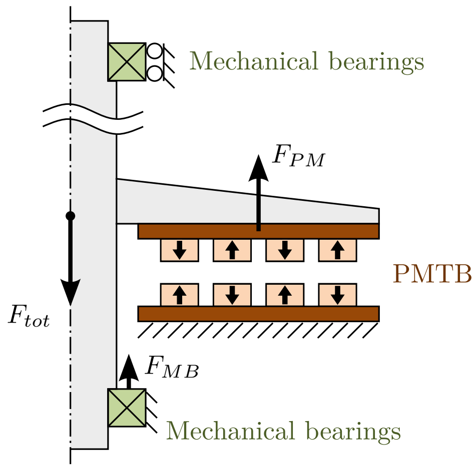

Figure 3.1: Combination of Permanent magnet thrust bearings (PMTB) and mechanical bearing (MB) for axial load repartition.

This combination system (MB & PMTB) can be used in applications with high axial load e.g. flywheel system [90], hydroelectric turbine [32] or vertical axis wind turbine [33, 34, 91]. This combination MB and PMTB can also be found in systems with smaller axial load, but where the life time needs to be very important, as in watt-hour meters [92].

In practice, non-ideal repartition of the axial force between the MB and PMTB can lead to a bad estimation of life span and friction losses. This non-ideal repartition can come from different causes described bellow.

First, the PM materials are sensitive to the temperature variation. In flywheel system for instance, the operating temperature of PMTB can reach high values due to internal losses inside those systems [93]. This increase of temperature impacts the load capacity due to the degradation of the PM properties [83].

Secondly, the PM are also subject to aging leading to a diminution of their performances [86] with time. In [94, 95], Haavisto et al. have measured the degradation of coercivity and remanence over the time. Those time-dependant degradation are function of the PM operating temperature, the permeance coefficient and the coercivity. The permeance coefficient is function of the PM dimensions and the magnetic field conditions during the operation.

Finally, the PM dimensions and properties are subject to tolerance. Weickhmann et al. show that the force can be miscalculated over more than 10% of error due to uncertainties in the PM dimensions as well as the remanence norm and the remanence orientation [76]. Even if the magnetic force is well evaluated, the integration of the PMTB in a complete mechanical device is subject to the mechanical tolerance of the system. Indeed, the magnetic force is dependent on the airgap thickness. Due to mechanical tolerance or deformation of the mechanical pieces, the airgap thickness can deviate from its theoretical value leading to a non-desired magnetic force.

From these observations, it is highlighted that there is a need for force/airgap thickness adaptation before integrating PMTB in some particular applications. In the literature, different patents are found with the aim to adapt the axial force due to load variations or temperature effect. Those solutions can either be active or passive.

3.2 State of the art

Two types of passive solutions are presented in the literature. These solutions are developed for watt-hours meter application. Indeed, in those kind of application, PMTB are used to increase the lifetime of the mechanical bearings. However, it is important to maintain the axial position of the measuring disc precisely. The combination MB-PMTB in these kind of applications results in a radial position maintained by the MB, but an axial position determined by the PMTB. So, this position depends on the axial force developed by the PMTB, and the temperature variations have to be compensated.

In US3582162 [96], authors solve the problem of temperature effect by passively adapting the airgap thickness such as to maintain a quasi-constant force. This is done by placing in series with the static part of the PMTB a thermally expandable piece as shown in Fig. 3.2 in red. In Fig 3.2.a, the support piece is a thermally expandable bimetallic piece. In Fig 3.2.b, the support piece contains a thermally expandable fluid. The main challenge of this solution is to find the good couple between shape and material properties of the thermally expandable piece such as to compensate the thermal behaviour of the magnet.

In US3810683 [97], authors solve the problem of temperature effect by adapting passively the magnetic field in the airgap. This is done by the use of a ferromagnetic material whose relative permeability is affected by the temperature i.e. the relative permeability decreases when the temperature increases and vice-versa. The ferromagnetic material is placed near the PM and short-circuits the magnetic flux out of the airgap as shown in Fig. 3.3. At room temperature e.g. $20°C$, some magnetic flux participates to the repelling axial forces, but part of the magnetic flux goes through the ferromagnetic shunt, without generating any axial force. When the temperature increases, the magnetic flux intensity decreases but is less deflected out of the airgap because of the diminution of the relative permeability of the ferromagnetic material. Consequently, the force remains quasi-constant with a temperature fluctuation. The main drawback of this solution is that the force is reduced at room temperature and thus the performances are intentionally decreased. Different patents based on the same principle can be found US4196946 [98], US3657676 [99] and US3107948 [100].

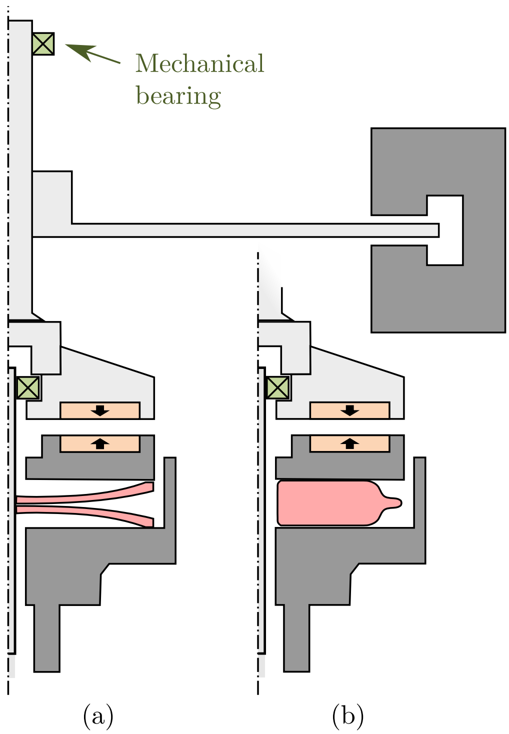

Figure 3.2: Passive compensation of the force variation due to temperature effect based on the thermal expansion of (a) bimetallic piece or (b) fluid contained in a casing (US3582162 [96]).

Both passive solutions are strongly dependent on the material properties of the PM and the thermally expandable piece for US3582162 and the ferromagnetic short-circuit piece for the US3810683. These material properties can be strongly non linear which leads to difficulties for the prediction and therefore for the good compensation. Moreover, these compensations systems are only valid for temperature compensation, but not for magnet aging nor for needed adaptations caused by mechanical or magnetic deviations from the expected properties.

In US9225222B2 [101], authors propose an active solution to change the axial load generated by a PMTB for rotating machinery, through the active adaptation of the airgap thickness. As shown in Fig. 3.4, the airgap thickness is adapted through the hydraulic cylinder. The static part of the PMTB is axially displaced by a cylinder. The position of the rotor is maintained constant because of the mechanical bearings acting as trust and centering bearing. The pressure in the cylinder is controlled through the pump and the required load is measured by a load sensor.

The problem of active solution is that it reduces the advantages of using passive

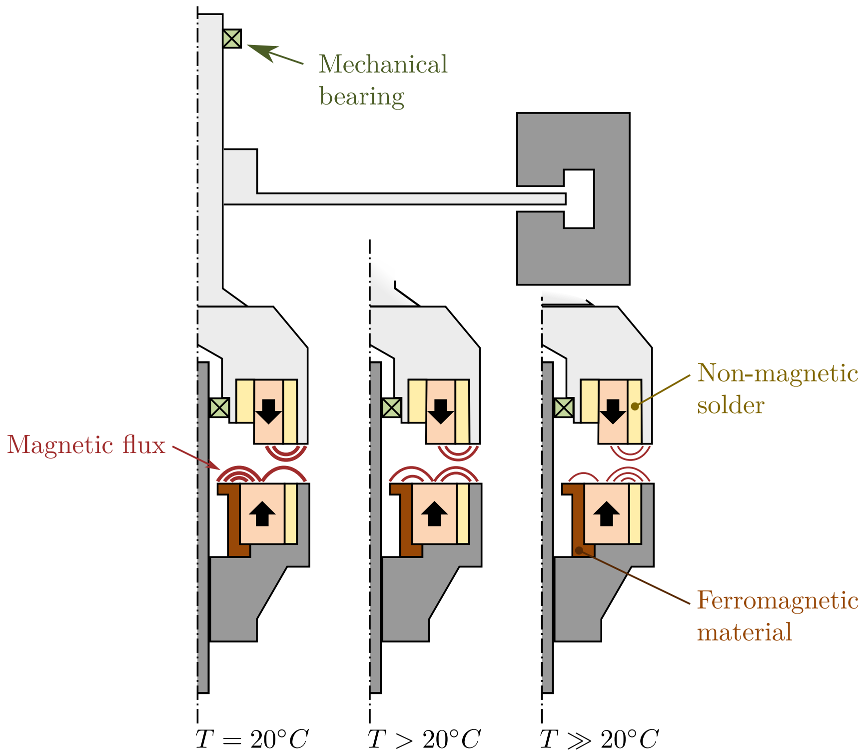

Figure 3.3: Passive compensation of the force variation due to temperature effect based on the variation of relative permeability with the temperature (US3810683 [97]).

bearing:

- working without sensors, controllers and power electronics,
- the simplicity and reliability,
- the cost,
- the compactness.

From these observations and to author's knowledge, there is a lack of passive solution to compensate effectively the negative impact of the temperature and the aging effect on the PM material as well as the mechanical and magnetic tolerance.

3.3 Compensation system principle

The proposed passive solution is based on placing in series with the static part of the PMTB a pneumatic or a hydraulic jack as shown in Fig. 3.5. Ideally, if the pressure p remains constant, the axial force in the jack F_{jack} and in the PMTB F_{PM} remains constant:

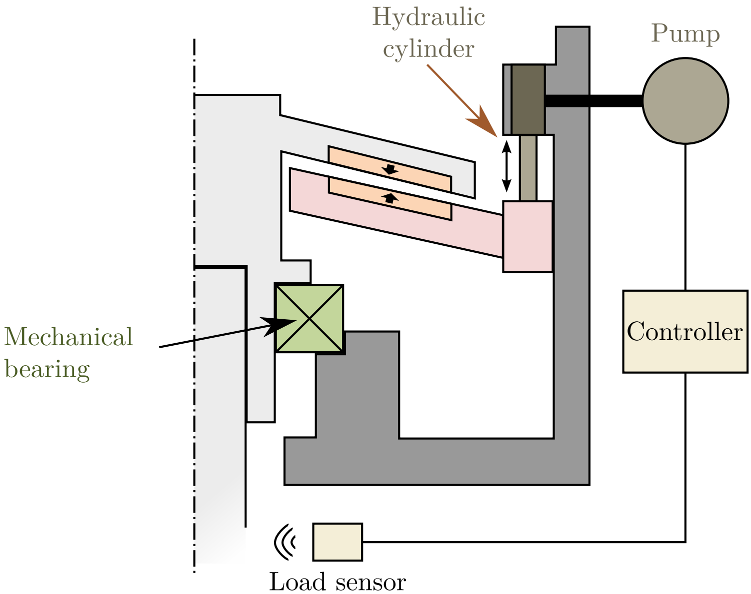

Figure 3.4: Active compensation of the force variation based on the control of a hydraulic cylinder to adapt the airgap thickness (US9225222B2 [101]).

$$F_{PM} = F_{jack} = (p - p_a)A_e \tag{3.1}$$

where p_a is the ambient pressure and A_e the effective area of the jack. The magnetic force is constant and the airgap thickness g is perfectly adapted.

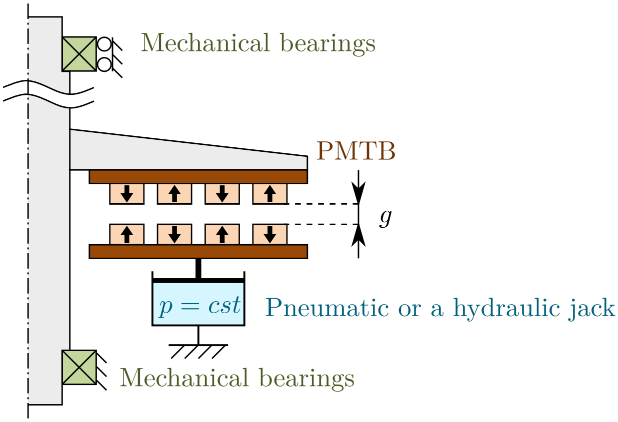

Figure 3.5: Combination of mechanical bearing with permanent thrust bearing (PMTB) and its passive ideal compensation solution.

In order to maintain a constant pressure, the jack needs to be connected to a compressor or a pump and therefore needs to be actively controlled. This leads to similar disadvantages as the active solution presented in section 3.2.

Another solution could be to allow small pressure variations with the axial position of the static part, by connecting the jack to an big enough external volume, decreasing the impact of an axial displacement on the total volume, and on the pressure. This principle is illustrated in Fig. 3.6 where the tank needs to be adapted if the fluid is a gas or a fluid.

In this situation, if the temperature inside the enclosure i.e., the PM temperature variates, the external volume allows to maintain a constant pressure. Nevertheless, this pressure is dependent on the ambient temperature corresponding to the temperature of the fluid. This ambient temperature can vary for example due to seasonal temperature variations and has an impact on the fluid pressure and the magnetic force. This effect needs to be taken into consideration in the design.

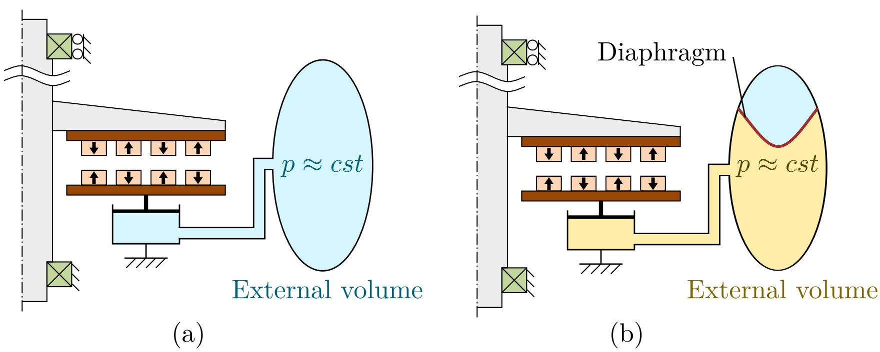

Figure 3.6: The solution connected to an additional external fluid tank. In (a), the fluid is a gas and in (b) the fluid is a liquid with a diaphragm expansion tank.

In practice employing pneumatic or hydraulic jack is a cumbersome solution and is quite expensive. However, an interesting solution could consist in using pressurized bellow as illustrated in Fig. 3.7. This implementation is really compact as it consist just in pressurizing air into the bellows.

Figure 3.7 illustrates different implementations of bellow-based air springs. In Fig. 3.7.a, a pneumatic bellow is schematically represented. Figures 3.7.b and 3.7.c show implementations based on pressurized metal bellows or diaphragm bellows respectively.

The next sections consider the impact of this jack/bellow on the load reliever system. For convenience, the jack/bellow is called "compensation system". Besides, only the compensation of the temperature effect on the PM properties is studied but the results can be extended to the other effects which would need to be compensated.

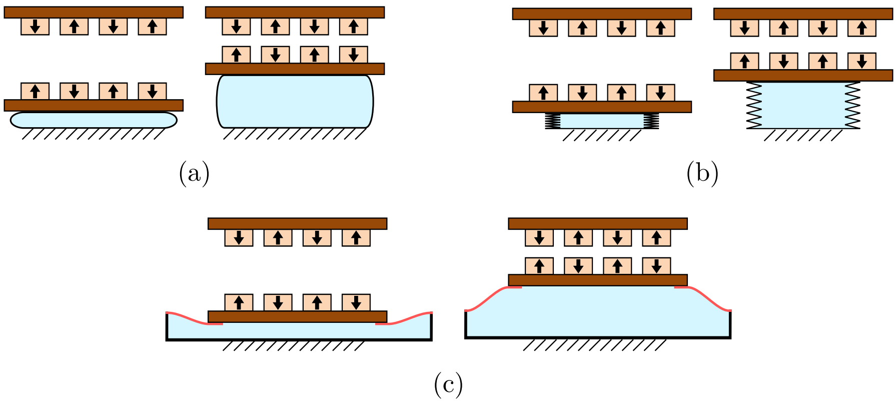

Figure 3.7: Practical implementation of pressurized air-based spring with high load capacity. (a) The pressurized pneumatic bellows, (b) the pressurized metal bellows, (c) the pressurized diaphragm bellows.

3.4 System modelling

The global system is represented in Fig. 3.8. The total axial load F_{tot} is supposed to be static. When the mechanical bearings consist in roller bearings, the PMTB does not carry the total axial load as a preload has to be maintained on the MB for good operation:

$$F_{tot} = \overbrace{F_{PM}}^{\alpha F_{tot}} + \overbrace{F_{MB}}^{(1-\alpha)F_{tot}} = \text{cst} \tag{3.2}$$

with F_{PM} and F_{MB} the axial force developed by the PMTB and the MB respectively and $0 \leq \alpha \leq 1$ the coefficient of repartition of the axial load.

The aim of this section is to show the impact of the equivalent stiffness associated to the compensation system on the global system. To evaluate this impact, an equivalent stiffness model is developed as represented in Fig. 3.8.b. The next section looks first at the equivalent stiffness model of the passive compensation solution and secondly at the equivalent stiffness model of the magnetic force. Finally, the equilibrium of the global system and the repartition of the total force are modelled.

3.4.1 Compensation system

As explained in section 3.3, ideally the compensation system is a pressurized jack with a constant pressure and therefore, the system compensates perfectly the axial force variation:

$$F_s^{ideal} = F_0 = A_e(p - p_a) \tag{3.3}$$

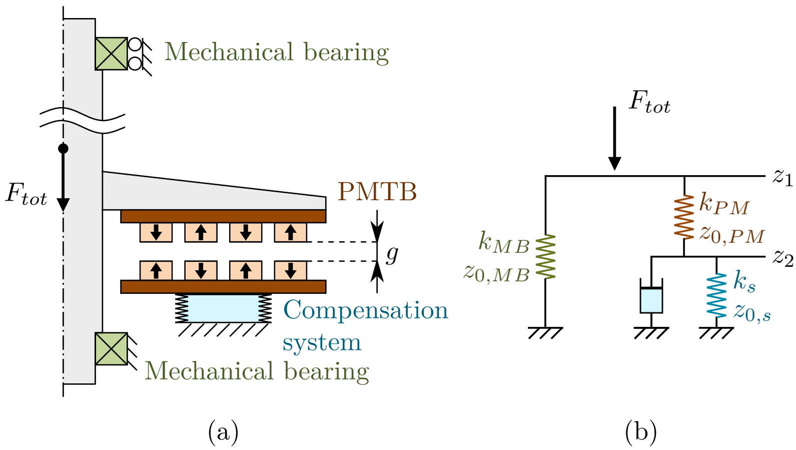

Figure 3.8: (a) Hybrid system with mechanical bearings and PM thrust bearing. the compensation system is placed in series with the PMTB to compensate the impact of the temperature effect on PM material by passively acting on the airgap thickness g. (b) The equivalent stiffness model.

with F_0 the force associate to the ideal jack, A_e the effective area of the jack, p the pressure in the jack and p_a the ambient pressure. Nevertheless in practice, the jack is implemented by bellows (see Fig. 3.7) and connected to an external volume (see Fig. 3.6). The compensation system can be modelled as the ideal jack in parallel to an equivalent spring as shown in blue in Fig. 3.8.b. The force in the jack can be evaluated by:

$$F_s = F_0 - k_s(z_2 - z_{0,s}) \tag{3.4}$$

with z_2 the axial position of the compensation system and k_s and $z_{0,s}$ the equivalent stiffness and natural length associated to the compensation system. This equivalent stiffness k_s takes into consideration the contribution of:

- the volumetric stiffness k_v linked to the variation of volume with the axial displacement,
- the area stiffness k_a linked to the variation of effective area with the axial displacement,
- the structural stiffness k_{struct} linked to the natural rigidity of the jack/bellows.

The volumetric stiffness due to the variation of the fluid volume k_v is given by [102, 103]:

$$k_v = \gamma \frac{pA_e}{V}\frac{\partial V}{\partial z} \tag{3.5}$$

with V the fluid volume and γ the Poisson constant. As the volume V is dependent on the displacement z, it is clear that this volumetric stiffness cannot be constant, especially if the jack/bellow is small. However, this equivalent stiffness is reduced by connecting the jack/bellow to an external tank so as to increase the fluid volume V without impacting the size of the jack/bellow.

The area stiffness k_a related to the deformation of the effective area is obtained by [102, 103]:

$$k_a = -(p - p_a)\frac{\partial A_e}{\partial z} \tag{3.6}$$

The equivalent stiffness of the compensation system is a combination of all these different stiffnesses:

$$k_s = k_{struct} + k_v + k_a \tag{3.7}$$

The equivalent natural length is obtained at the nominal position of the Compensation system $z_{s,n}$ corresponding to the axial position of the compensation system when the force in the latter equals the nominal force $F_s = F_0$:

$$z_{0,s} = z_{s,n} \tag{3.8}$$

3.4.2 PMTB

The axial force developed by the PMTB is obtained by a 2D axisymmetric finite element model presented in chapter 2.2. The reversible and irreversible demagnetization curves of the PM material are taken into consideration. The force is dependent on the temperature T and the airgap thickness g.

The evolution of the axial force with the temperature T for different airgap thicknesses g obtained by the FEM are given in Fig. 3.9 for the application case of section 3.5. The solid line corresponds to the demagnetization curve with reversible (before the knee point of the B-H characteristic) and irreversible effect (after the knee point of the B-H characteristic). The dashed line, extending the first part of the solid line, corresponds to the axial force predicted by the FE model when only reversible demagnetization is considered. Consequently, before the separation point, the demagnetization is reversible. The horizontal line at $F_z = 20\,kN$ corresponds to the reference load. To maintain a constant axial force when the temperature is increased, the airgap thickness has to decrease. To avoid irreversible demagnetization, the temperature may not exceed the maximal temperature $T_{irr} = 152\,°C$ for an airgap thickness of $g = 2.2\,mm$.

The axial force of the PMTB is non-linear with the airgap thickness and the temperature. The axial force $F_{PM}(g_0, T)$ at a given airgap thickness g_0 and a given temperature T is obtained by the FEM:

$$F_{PM}(g_0, T) = FEM \tag{3.9}$$

For any operating point characterized by a temperature T and an airgap thickness g, the PMTB can be modelled by an equivalent stiffness k_{PM} and natural length $z_{0,PM}$ as follows:

$$F'_{PM}(g, T) = -k_{PM}(g_0, T)\,(g - z_{0,PM}(g_0, T)) \tag{3.10}$$

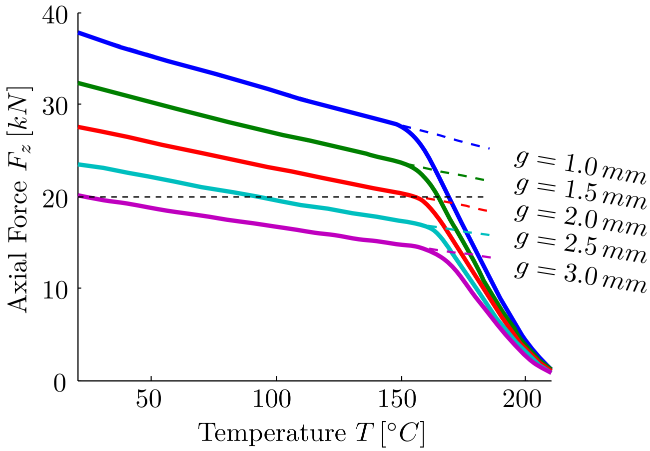

Figure 3.9: FEM results of the evolution of the axial force with the temperature for different airgap thicknesses. The solid line corresponds to demagnetization with reversible and irreversible effect and the dashed with only reversible demagnetization.

where the equivalent stiffness $k_{PM}(g_0, T)$ and the equivalent natural length $z_{0,PM}(g_0, T)$ are dependent on the reference airgap thickness g_0 and the given temperature T. Figure 3.10 shows the evolution of the axial force with the airgap thickness for 2 different couples of temperature and airgap thickness $(T = 20\,°C,\ g_0 = 3\,mm)$ and $(T = 150\,°C,\ g_0 = 1\,mm)$ for the application case of section 3.5. The solid line corresponds to the FE results and the dashed line to the equivalent linearized model.

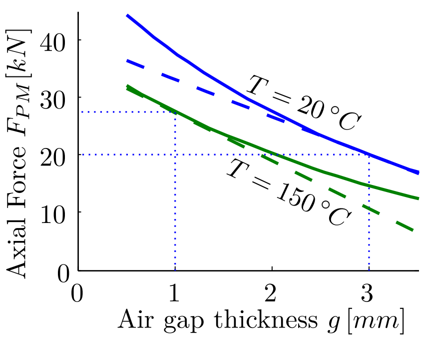

Figure 3.10: Linearization of the axial force in the PMTB at the airgap thickness/temperature of $(T = 20\,°C,\ g_0 = 3\,mm)$ and $(T = 150\,°C,\ g_0 = 1\,mm)$. Solid line: axial force from FEM F_{PM}, dashed line: the linearized axial force F'_{PM}.

The equivalent stiffness is evaluated by the numerical derivation of the axial force generated by the PMTB:

$$
\begin{aligned}
k_{PM}(g_0, T) &= -\left.\frac{\partial F_{PM}(z,T)}{\partial z}\right|_{z=g_0} \\
&\approx -\frac{F_{PM}(g_0+\delta_z, T) - F_{PM}(g_0-\delta_z, T)}{2\delta_z}
\end{aligned}
\tag{3.11}
$$

where $F_{PM}(z, T)$ is the axial force evaluated by the 2D axisymmetric FEM.

The equivalent natural length is obtained by:

$$
z_{0,PM}(g_0, T) = g_0 + \frac{F_{PM}(g_0, T)}{(k_{PM}(g_0, T)}
\tag{3.12}
$$

Finally (3.9), (3.11) and (3.12) are summarized in:

$$
(F_{PM},\, k_{PM},\, z_{0,PM}) = \mathcal{H}(g_0, T)
\tag{3.13}
$$

3.4.3 Equilibrium of the global system

The axial behaviour of the complete hybrid system, including the MB, the PMTB and the compensation system, can be modelled by an equivalent linearized (stiffness) model as shown in Fig. 3.11, with k_i the equivalent stiffness and $z_{0,i}$ the equivalent natural length of element i. The axial positions of the MB, PMTB and compensation system are given by the axial positions of the points (z_1, z_2). Referring to Fig. 3.8, the variation of the airgap thickness Δg is equal to the difference of variation of the axial positions of points z_1 and z_2:

$$
\Delta g = \Delta z_1 - \Delta z_2
\tag{3.14}
$$

The hypotheses of the equivalent model are that:

- the weight of the compensation system and PMTB are negligible compared to the axial force;
- the compensation system and the MB have a linear behaviour with the axial displacement and are independent on the temperature.

Based on the equivalent linearized model, the equilibrium of the system from Fig. 3.8 is calculated. Using theory of series and parallel springs (see appendix D), the axial position z_1 and z_2 are obtained:

$$
\begin{aligned}
z_1 &= \frac{1}{k_{MB} + k_{ser}}\left(k_{MB} z_{0,MB} + k_{ser} z_{0,ser} + \frac{k_{PM} F_0}{k_{PM} + k_s} - F_{tot}\right) \\
z_2 &= \frac{1}{k_{PM} + k_s}(k_{PM} z_1 + F_0 - k_{PM} z_{0,PM} + k_s z_{0,s})
\end{aligned}
\tag{3.15}
$$

with k_{ser} and $z_{0,ser}$ the equivalent stiffness and natural length of the PMTB and the compensation system:

$$
\begin{aligned}
k_{ser} &= \frac{k_{PM} k_s}{k_{PM} + k_s} \\
z_{0,ser} &= z_{0,PM} + z_{0,s}
\end{aligned}
\tag{3.16}
$$

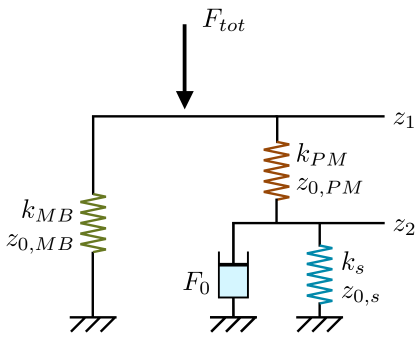

Figure 3.11: Linearized equivalent (stiffness) model of the mechanical bearing (k_{MB}, $z_{0,MB}$), the PMTB (k_{PM}, $z_{0,PM}$) and the compensation system (k_s, $z_{0,s}$) with k_i the equivalent stiffness and $z_{0,i}$ the equivalent natural length for each element.

Solving the system of two equations (3.15) and two unknown variables (z_1 and z_2) at reference temperature T_{ref} gives the "*Reference*":

- the reference position $z_{1,ref}$ and $z_{2,ref}$;
- the reference airgap thickness g_{ref};
- the reference magnetic $F_{PM,ref}$ and mechanical $F_{MB,ref}$ forces.

With a variation of temperature, i.e. $T \neq T_{ref}$, the behaviour of PMTB change. Due to the non-linearity, an iterative method has to be used. At the "*Start*", the new magnetic force is evaluated for the same axial position but for a different temperature. In the "*While loop*", the following steps are implemented:

1. Evaluation of the new axial positions z_1 and z_2.
2. Evaluation of the new airgap thickness g.
3. Evaluation of the new magnetic F_{PM} and mechanical forces F_{MB}.

The sum of the two forces $F_{PM} + F_{MB}$ is compared with the total axial load F_{tot}. The convergence is reached if the error is lower than 0.01%. At the "*End*", the new equilibrium is calculated and the new magnetic and mechanical forces, airgap thickness and axial positions are obtained. The algorithm is depicted in Fig. 3.12.

3.5 Impact of the compensation system stiffness

As explained before, ideally the compensation system should have no stiffness. But due to the practical implementation of the compensation system, it presents a non zero stiffness. This is why this section strives to analyse the impact of the equivalent stiffness on the global system for a particular application case. This application case considers a PMTB with an axial polarization, radial

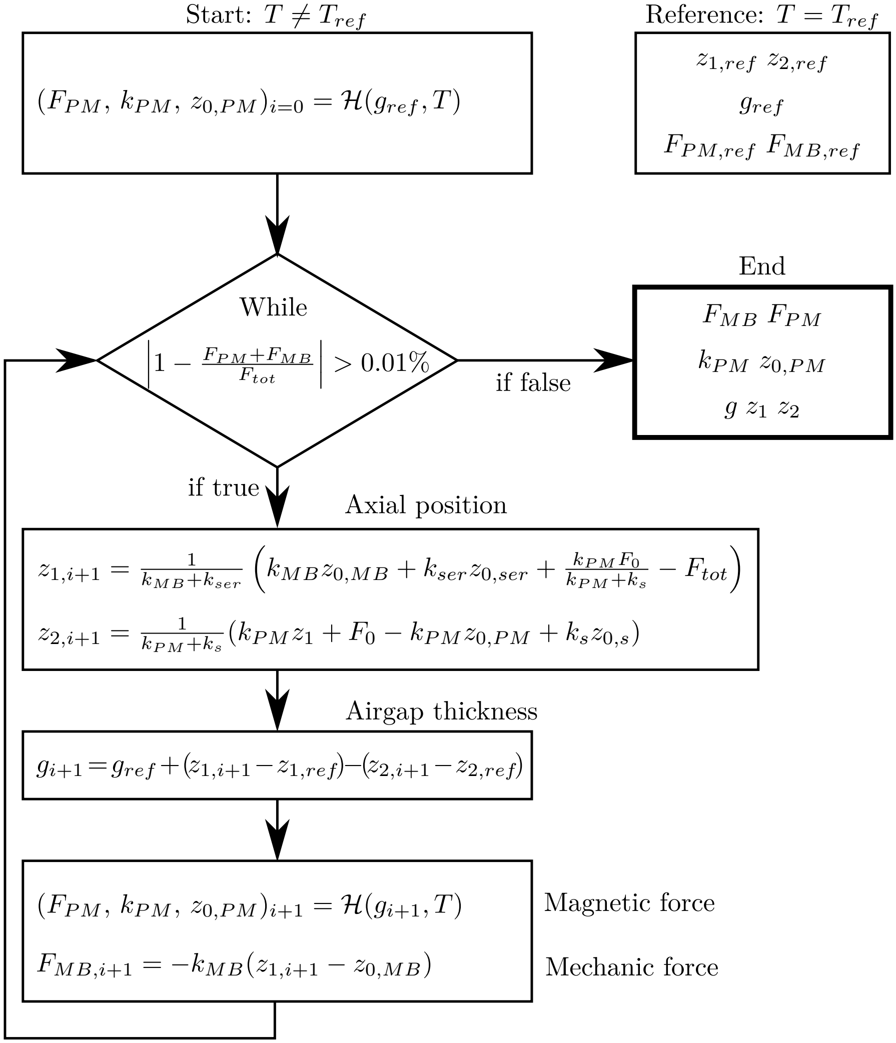

Figure 3.12: Algorithm used to evaluate the new equilibrium in the system. Due to the non-linearity of the axial force in the PMTB, an iterative method is used.

superposition, and back iron topology. The PM properties and PMTB dimensions are summarized in Table 3.1. These dimensions are obtained from scaling laws minimizing the PM volume (see chapter 1) considering an axial load $F_{PM} = 20\,kN$, an airgap thickness $g = 3\,mm$ and a remanence $B_r = 1.20\,T$. The PM materiel grade is N35UH and corresponds to the remanence at a temperature of $T_{ref} = 20\,°C$. The maximum operating temperature recommended by the PM manufacturers is $T_{max} = 180\,°C$. Nevertheless, this information is not a sufficient criterion. The maximum operating temperature has to be defined before the PM material becomes irreversible demagnetized T_{irr}. This temperature is correspond to the point where the dashed-line and the solid line diverge in Fig 3.9 and is therefore dependent on the airgap thickness.

The total axial load is $F_{tot} = 25\,kN$ and is distributed between the mechanical bearing $F_{MB,ref} = 5\,kN$ and the magnetic bearing $F_{PM,ref} = 20\,kN$. At room temperature ($20\,°C$), the equivalent stiffness of the PMTB is equal to $k_{PM,ref} = 6.52\,kN/mm$. The stiffness of the mechanical bearing is classically of a greater order. In a first study, it is considered to be very stiff in comparison of the PMTB stiffness: $k_{MB} = 1000 \times k_{PM,ref}$. The influence of the jack/bellows stiffness k_s is given in relative values in comparison with the reference PMTB stiffness $k_{PM,ref}$.

Table 3.1: Dimensions and properties of the PM rings (N35UH)

	Parameters	Value
w	PM width	$6.39\,mm$
h	PM height	$2.22\,mm$
ζ	Space between the rings	$2.01\,mm$
R_{int}	Internal radius	$186.3\,mm$
N	Number of rings	20
$B_{r,20°C}$	Remanence	$1.20\,T$
$H_{k,20°C}$	Coercivity: knee point	$1920\,kA/m$
$H_{cJ,20°C}$	Polarization coercivity	$2000\,kA/m$
$\mu_{r_{PM}}$	PM relative permeability	1.05
α_{B_r}	Temperature coefficient of remanence	$-0.11\,\%/K$
α_H	Temperature coefficient of coercivity	$-0.50\,\%/K$

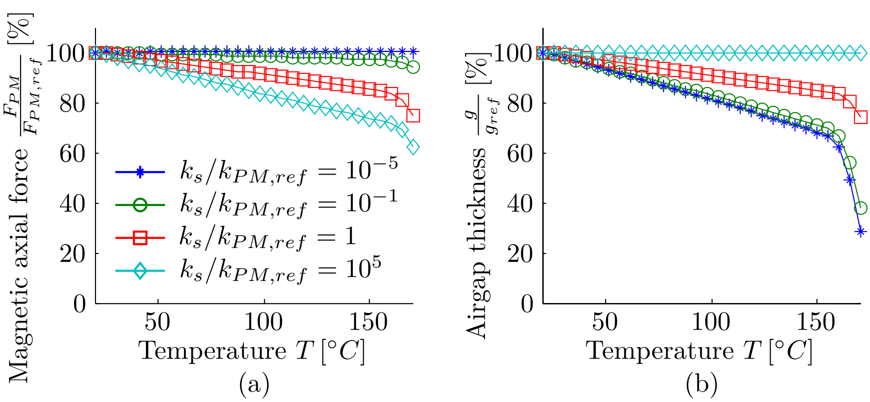

Figure 3.13: (a) Evolution of the magnetic axial force and (b) airgap thickness in percentage with the temperature for different spring stiffnesses.

In Fig. 3.13, the evolution of the force generated by the PMTB (a) and the equivalent airgap thickness (b) with the temperature is given for different relative spring stiffnesses $\frac{k_s}{k_{PM,ref}}$. Two extreme cases are presented:

- For $\frac{k_s}{k_{PM,ref}} = 10^5$, the system is strongly rigid and therefore has a behaviour similar to the system without jack/bellow. The PMTB axial force drops with the temperature and the airgap thickness remains approximatively constant. Before irreversible demagnetization effect, the axial force is at 72% of its reference value for a temperature of $160\,°C$.
- For $\frac{k_s}{k_{PM,ref}} = 10^{-5}$, the system is strongly soft. The axial force is perfectly compensated and stays quasi-constant with the temperature. The airgap thickness is passively adapted. As observed, the axial force remains quasi-constant even if the temperature exceeds the maximal temperature before irreversible demagnetization $152\,°C$. In this region, the airgap thickness drops drastically because of the PM irreversible demagnetization.

In between these extreme cases, the jack/bellow acts to compensate partially the temperature effect on the magnetic force. For instance, with a stiffness equal to the reference stiffness $\frac{k_s}{k_{PM,ref}} = 1$, the axial force drops at 84% before irreversible demagnetization at $T_{irr} = 158\,°C$. With a stiffness ten times smaller than the reference stiffness $\frac{k_s}{k_{PM,ref}} = 10^{-1}$, the axial force drops at 97% for a temperature before irreversible demagnetization of $T_{irr} = 156\,°C$. These values are summarized in Table 3.2. The temperature T_{irr} changes with the value of the equivalent stiffness because, as explained earlier, this temperature is dependent on the airgap thickness, itself dependent on the equivalent stiffness.

Table 3.2: Dimensions and properties of the PM rings (N35UH)

$\frac{k_s}{k_{PM,ref}}$	$\frac{F_{PM}}{F_{PM,ref}}$	$\frac{g}{g_{ref}}$	T_{irr}
10^5	72%	$\sim$ 100%	$160°C$
1	84%	83%	$158°C$
10^{-1}	97%	69%	$156°C$
10^{-5}	$\sim$ 100%	67%	$152°C$

The different curves represented in Fig. 3.13 show only the first increase of temperature. The hysteresis effect that could be due to an irreversible demagnetization is not taken into consideration. In case of an irreversible demagnetization occurred, the jack/bellow is still able to maintain a quasi-constant magnetic force even if the temperature decreases. In that case, however, the airgap thickness would not come back to its reference values but to a smaller value depending on the depth of the irreversible demagnetization.

In Fig. 3.14.a, the evolution of the axial force with the relative jack/bellow stiffness is given for four different temperatures: $50\,°C$, $100\,°C$ and $150\,°C$ in the reversible region and $170\,°C$ in the irreversible region. Figure 3.14.b. shows the corresponding airgap thickness. We observe that for $\frac{k_s}{k_{PM,ref}}$ higher than

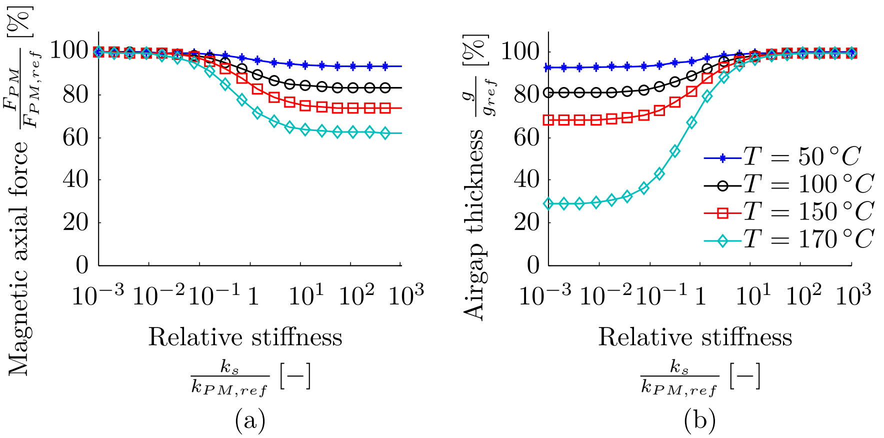

Figure 3.14: (a) Evolution of the magnetic axial force and (b) airgap thickness in percentage with the relative spring stiffness for 4 different temperatures: $50\,°C$, $100\,°C$ and $150\,°C$ in the reversible region and $170\,°C$ in the reversible region.

10, the spring does not compensate the temperature effect even partially. In opposition, with a stiffness ratio $\frac{k_s}{k_{PM,ref}}$ lower than 10^{-1}, the temperature effect is well compensated.

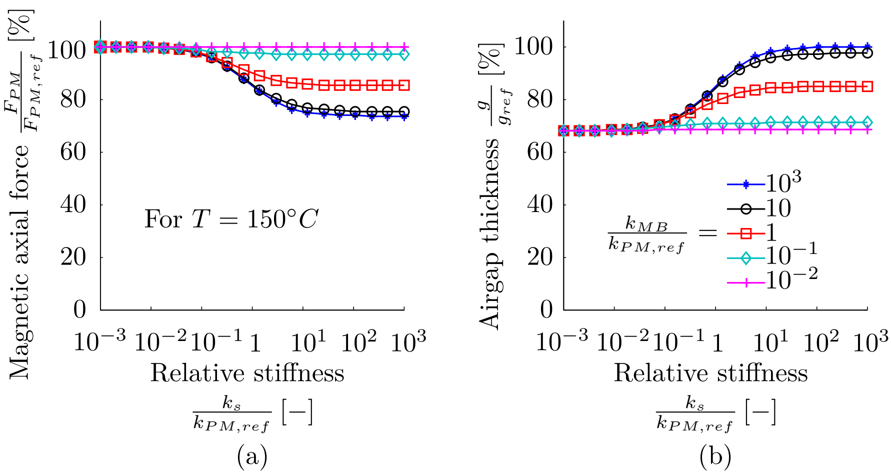

Figure 3.15: Evolution of (a) the magnetic axial force and (b) the airgap thickness in percentage with the relative spring thickness for 5 different mechanical bearing stiffnesses k_{MB} and for a PM temperature of $150°C$.

Figure 3.15 reveals the influence of the mechanical bearing stiffness on the global system for a PM temperature of $150°C$. As explained, it is classically of an order of magnitude greater than magnetic bearings but in some cases this difference could be smaller. Figure 3.15 shows the influence of the jack/bellow stiffness on the magnetic force (a) and airgap thickness (b) for 5 different values of mechanical stiffnesses. We observe that having a small mechanical stiffness in comparison to the magnetic stiffness helps to maintain a quasi-constant magnetic force.

3.6 Conclusion

Combining permanent magnet load reliever (permanent magnet thrust bearings) and mechanical bearings allows to relieve the load on the latter and therefore to reduce the losses and increase the lifetime of the system. However Due to temperature effect and aging, the performance of the permanent magnets can deteriorate. In addition, magnetic and mechanic tolerance lead to bad evaluation of the magnetic force. All these factors lead to a diminution of the system performances. This chapter shows that placing an ideal jack in series with the static part of the PM bearing is a solution for maintaining a constant magnetic force. The desired magnetic force is set by imposing the pressure during the assembly and solves the problem of mechanical and magnetic tolerances. During operation, the magnetic force is maintained constant even if there is a change in magnetic properties due to temperature or aging. Practically, the passive compensation system could be implemented with pressurized bellow.

However, due to the volumetric, the area and the structural stiffnesses, an equivalent stiffness is associated to the jack/bellow of the jack/bellow. This stiffness has an impact on the global behaviour and affects the passive compensation effect. This chapter shows that for an equivalent stiffness of the jack/bellow ten times smaller than the stiffness on the PMTB, the compensation is well performed.

The compensation solution has also an impact on the sizing of the PMTB. Indeed, the PMTB needs to be sized larger in order to generate the same axial force before and after the degradation of the PM properties. Consequently, the required PM volume will increase. For the radially stacked topologies, the PMTB needs to be sized for a larger airgap thickness than for the system without the compensation solution. This larger airgap thickness allows in case of PM properties degradation, the axial displacement of the static part.

The compensation system is suited for radially stacked topology. Nevertheless, it could be extended to axially stacked topology with some adaptations mainly due to the design rules on the equivalent stiffness. The PMTB also needs to be sized lager and for an axial offset different than the optimal one i.e., the one leading to the maximal axial force. This allows to have a positive axial stiffness and to allows the axial displacement.

From a more global point of view, Table 3.3 illustrates a comparison between the proposed solution and other solutions, used in combination with roller bearings:

1. permanent magnet thrust bearing with soft spring (proposed solution),
2. permanent magnet thrust bearing,
3. active magnetic bearing.

The comparison is based on different key factors and and takes as references a solution with only roller bearings: "+" means better than mechanical bearing alone ; "-" means worst.

As observed, the proposed solution is more expensive than PMTB alone but allows to increase the performance in term of temperature stability and in adaptability.

Table 3.3: Comparison of different bearing solutions. Legend: "+" means better than mechanical bearing alone and "-" means worse.

	Mechanical bearing &			
Key factors	PMTB with compensation system (proposed solution)	PMTB	Nothing	Active magnetic bearing
Lifetime	+	+	0	+
Investment cost	- -	-	0	- - -
Maintenance cost	+	++	0	+
Consumption	+	+	0	0
Temperature sensitivity	0	-	0	0
Reliability	0	0	0	-
Adaptability to tolerance faults	0	-	0	0

The different key factors are more or less important depending on the application in which the solution has to be implemented. Table 3.4 gives the importance of each key factor for different applications with high axial load. Cross-checking the both tables shows that the proposed solution is interesting for flywheel application as well as vertical axis wind turbine and hydroelectric turbine.

Publications related to this chapter:
[104] Van Beneden M, Kluyskens V and Dehez B. “Passive compensation of the temperature effect on permanent magnet thrust bearing in hybrid system”.

Table 3.4: Importance of the key factors for different applications. Legend: "+" means importance of the factor for the application.

	Lifetime	Investment cost	Maintenance cost	Consumption	Temperature sensitivity	Reliability
Flywheel	++	+	+	++	+	+
Vertical axis wind turbine	++	+	++	+	0	+
Horizontal axis wind turbine (yaw system)	++	+	++	0	0	+
Hydroelectric turbine	++	+	++	0	0	+
Compressor	+	+	+	0	+	+
Radar	+	+	+	0	0	+
Magnetic coupling	+	++	0	0	+	+

16th international symposium on magnetic bearings (ISMB16). Beijing, China, 2018.

Practical implementation 4

This chapter presents the practical implementation of permanent magnet thrust bearings (PMTB). In the context of the ECOPTINE project, two PMTB have been designed, assembled and characterized. One PMTB has been realized for an electrical machine and another one for the flywheel.

This chapter presents first a state of the art in the implementation of PMTB. Then, an implementation of the PMTB for the electrical machine and for a flywheel are presented in section 4.2 and section 4.3 respectively.

4.1 State of the art

Permanent magnet (PM) thrust bearings (PMTB) for rotating applications are ideally realized with the superposition of uniform and rigid polarized PM rings so as to present an axisymmetry. In this case, the magnetic force is constant without any variation as well as no magnetic torque. Moreover, there are no eddy current losses. Unfortunately, the realization of PMTB based on complete rings is most of the time complicated. This is due to different reasons. First, the dimensions of PM rings are limited because of manufacturing constraints [33, 64] and obliges the designers to move away from optimal dimensions. Secondly, PM materials are often fragile materials [105] and are difficult to manipulate due to the high magnetic force between themselves or with ferromagnetic material. Consequently, there is a risk of breaking PM during the assembly. Finally, PM rings placed on the rotating part of the PMTB are subject to high internal stresses due to centrifugal effect and their is a risk of failure during operation.

In the literature, authors suggest to segment the PM rings into smaller magnets and then, to assemble the different parts to compose the complete rings. The segments can be of different shapes e.g., rectangular or arc-shaped segment. The drawback of the segmentation is that the magnetic field is no longer uniform and therefore, torque/force ripple appears as well as eddy current losses.

The aim of this section is to highlight the different advantages and disadvantages of the different implementations proposed in the literature. In addition, comments on the production of PMTB are given to highlight the difficulties encountered by the authors.

In [106], Mystkowski et al. have designed and realized a PM centering bearing based on complete PM rings. The topology is the axial stacked structure with axial polarization and the number of superposed rings is $N = 4$ as shown in Fig 4.1. The PM material is a $NdFeB$ magnet of grade N38. The PM dimensions are summarized in Fig 4.1. As observed, the PM dimensions are limited to small diameter with a large PM section and with a large airgap thickness of $g = 4.5\,mm$ which is far from optimal dimensions. In order to reduce the airgap thickness, authors suggested to place an iron sleeve as shown in Fig 4.1. This also presents the advantage to hold the PM mechanically. Nevertheless, the iron sleeve short-circuits the magnetic field and reduces the performance.

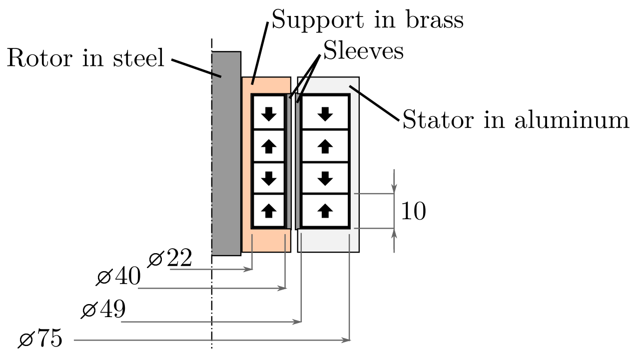

Figure 4.1: PMTB developped by Mystkowski et al. [106].

This implementation is interesting because it allows to generate force and stiffness without ripple and without eddy current losses. Nevertheless, the maximal force is limited to value of around $120\,N$ corresponding to a radial displacement of $1\,mm$. Other authors also studied PMB fabricated with unsegmented PM rings like Mystkowski et al. These PMTB are designed for applications with low loads [34, 107, 108] due to the limited size of PM rings.

In Uppsala University Sweden, Abrahamsson et al. have implemented a PMTB for a composite flywheel energy storage system [109]. The guiding system is a full magnetic levitation system with a centering active magnetic bearing and a PMTB. The PMTB is represented in Fig. 4.2 and is able to carry $1.04\,kN$. The rotating part of the PMTB is a Halbach array with segmented rings. The rings are segmented to decrease the tensile stress in the PM during the rotation. The stationary part of the PMTB is not segmented rings to minimize the induced eddy current as well as the torque/force ripple. In [110], authors evaluated the eddy current losses generated by the semi-segmented Halbach array. The eddy currents are induced by non-uniform magnetic field and two types are considered: non-uniformity of the remanence amplitude in and between magnets and non-uniformity due to non-radial magnetization of the radial ring of the halbach array. Indeed, the radially PM segments required in the Halbach array cannot be magnetised truly radially during manufacturing. Authors highlight that the non-radial magnetization was estimated to induce more than 10 times more losses than remanence variations. The total losses are located in the stator due to the semi-segmented structure and are evaluated at $9\,W$ for an airgap thickness of $6\,mm$ and a rotational speed of $30\,000\,rpm$.

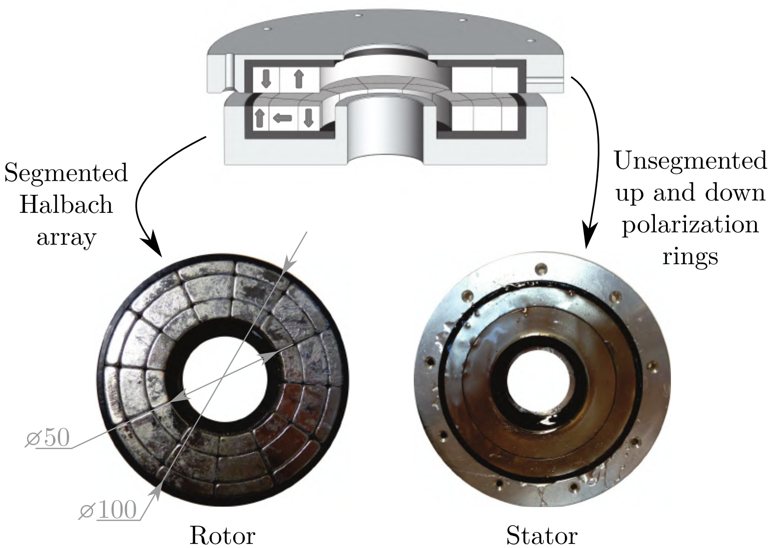

Figure 4.2: PMTB developped by Abrahamsson et al. [109] with a segmented Halbach array in the rotor and an unsegmented up and down polarization rings in the stator.

Authors pointed out the problem of assembling Halbach structure due to the unstable force between the PM segments. They develop an auxiliary tool used to assemble a triplet of segments $|\uparrow|\leftarrow|\downarrow|$ corresponding to one segment of the complete system (see Fig 4.3). First, the contacting surface of PM are roughened with abrasive paper, cleaned with alcohol and placed in the auxiliary tool. The triplets are glued one by one in a plastic and the complete system is covered of epoxy. Based on this process, the segments of the different superposed rings are aligned and therefore, it increases the torque/force ripples in comparison of a randomly distribution.

In Uppsala University Sweden, Pérez-Loya et al. [111] have designed and built a PMTB for a synchronous generator. Authors achieved the guiding system by combining an electromagnetic thrust bearing, a PMTB and mechanical bearings. The selected topology is a radially stacked Halbach array with back iron designed to carry $2000\,kg$. The rotating part of the PMTB is shown in Fig 4.4.a. The PM rings are segmented and the shape of the segments are cubes of $12\,mm$ side. The PM material is NdFeB N48. The shape, size and material were selected to meet the following criteria:

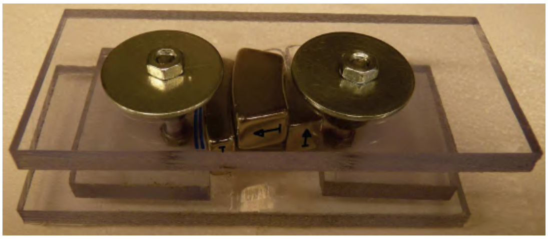

Figure 4.3: Auxiliary tool developed by Abrahamsson et al. [109] to assemble one triplet of PM segments.

- to be handled by hand,
- to have low price since the volume of ordered PM was high and in standard size.

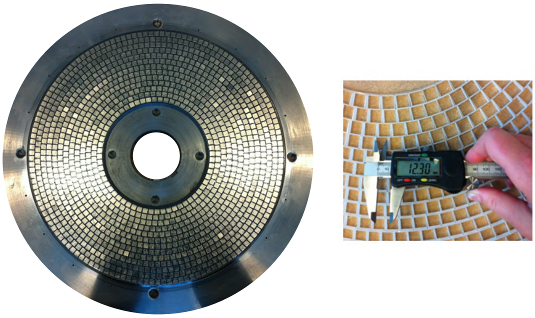

(a) (b)

Figure 4.4: PMTB designed in Uppsala University [111]. (a) the rotating part of the PMTB and (b) the polycarbonate mesh for cubic magnet positioning .

Authors point out that having a ferromagnetic material in the plates was useful during the assembly process. In order to keep the PM in place and to facilitate the assembly process, a mesh made of polycarbonate was built and is shown in Fig 4.4.b. The PM cube are positioned randomly in the tangential direction such as to reduce the eddy current losses and the torque/force ripple. Moreover, authors do not placed the same number of segments on the rotor than on the stator for the same reasons.

Despite the back iron structure, the PM cubes in a Halbach array are unstable in their nominal position and each PM needs to be glue. The drawback of using glue is that the mounting time is drastically increased. After the mounting of all PM, the rotating and static parts were covered with epoxy.

During the final step of the assembly, the rotating part was placed in front of the static part. Due to the negative radial stiffness, some precautions had to be taken. Pérez-Loya et al. placed 4 centering pin to guide the rotating part as shown in Fig.4.5. To avoid undesirable and dangerous contact between the

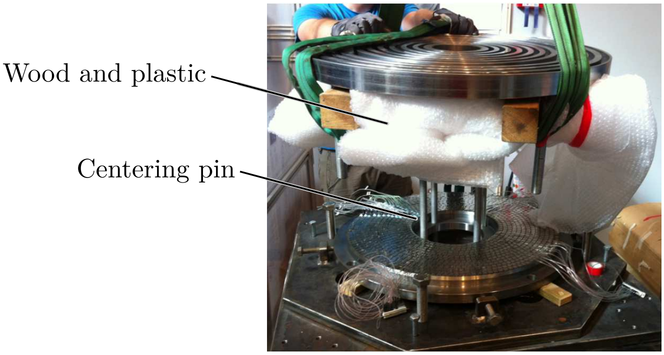

Figure 4.5: Final step of the assembly of the PMTB in Uppsala University [111] with centering pins and non-magnetic protection.

PM and ferromagnetic material during the transport, non-magnetic protection needed to be added.

Pérez-Loya et al. performed some test on the produced PMTB [32]. They showed that the axial force ripple of $60\,N$ peak-to-peak is negligible in comparison of the average force of $12.56\,kN$.

In [33], Kumbernuss et al. have realized a PMTB for a vertical axis wind turbine. The topology corresponds to the radial stack (with $N = 2$) with axial polarization. The PM rings are segmented and the shape of the segments are rectangular ($5.5 \times 3 \times 7.3$). The PM material is a Y8T ferrite magnet. Authors placed a soft magnetic plates in the airgap and linked to the rotor as shown in Fig.4.6. The aim is to smooth the magnetic field in the airgap and therefore to reduce the force and torque ripple. In addition, author do not placed the same number of segment between the inner ring and outer ring with 36 and 42 respectively. This solution has however some drawbacks. As for [106], the soft magnetic plate short-circuits the magnetic flux of the rotor and therefore reduces the average force. In addition, eddy current losses are generated in the soft magnetic material during rotation corresponding to an average friction torque.

For an airgap thickness of $5\,mm$, the results without soft magnetic plates give an average axial force of $16\,N$ and a variation peak-to-peak of $10\,N$. With the soft magnetic plates, the average force is reduced to $11\,N$ but with oscillations lower than $0.1\,N$.

In [112], Mukhopadhyay et al. have designed a PMTB based on two opposite aluminium disk with rings made of cylindrical PM as shown in Fig. 4.7. To reduce costs, the authors used a ferrite PM. The fabrication is very simple but leads to very bad performances. Nevertheless, authors assume that due to aging and demagnetization effect, the performance of PMB can decrease [107] with time and it is preferable to produce low cost PMTB which can be easily replaced.

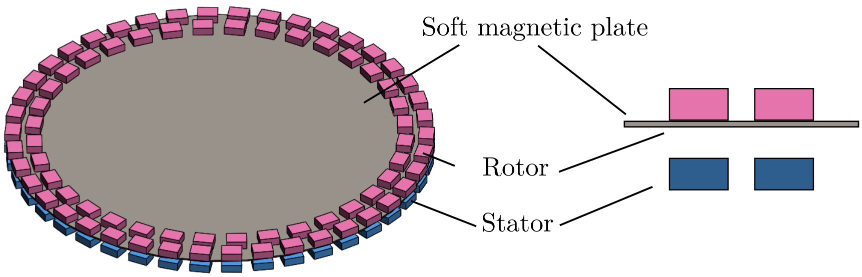

Figure 4.6: The PMTB developped by Kumbernuss et al. [33] with soft magnetic plate placed on to the rotor to reduce the ripple.

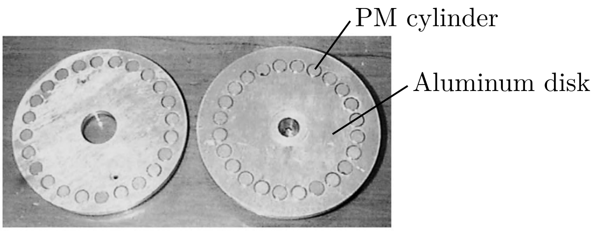

Figure 4.7: The PMTB developped by Mukhopadhyay et al. [112] with rings segmented in PM cylinders.

To summarize, the different problems faced by the authors are:

- Reducing force and torque ripple by randomly distributing the PM segments.
- During the assembly, precautions must be taken to prevent shocks on magnets which can lead to breakage due to their fragile characteristic. To help the manipulator, non-magnetic tools can be used.
- After the full assembly of the PM segments on the rotating and static parts, the magnetic force can be very high and can lead to dangerous situation. Some care need to be taken during the storage and the transport for example by adding non-magnetic protections. During the mounting of the rotating part on the static part of the PMTB, guiding elements need to be used to counteract the effect of the negative radial stiffness.
- During operation, the rotating part can suffer from internal stress due to the centrifugal effect. Therefore, the PM segments must be held mechanically.
- PM material have globally bad resistance to corrosion especially neodymium magnet. The PM segments need to be coated e.g. with Ni & Cu-coating. In addition, the PM can be protected with epoxy [113].

4.2 Study case 1 - Electrical machine

A permanent magnet thrust bearing (PMTB) working as load reliever has been designed for a vertical axis electrical machine. The guiding system i.e. the thrust and centering functions are achieved by the electrical machine ball bearings. The selected topology of PMTB is the radial stack with axial polarization and with back-iron structure as shown in Fig. 4.8.

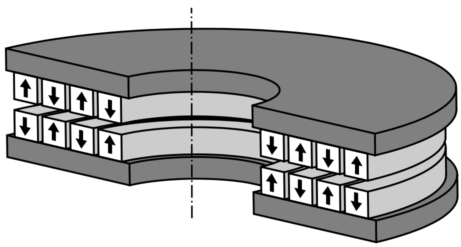

Figure 4.8: Sectional view of the 3D representation of the radial stack topology with axial polarization and with back-iron support.

The PMTB is placed at the top of the electrical machine as represented in Fig. 4.9. The rotating part is fixed on the shaft through a spacer by a bolt. The airgap thickness g between the rotating and stationery parts can be adapted by changing the thickness of the spacer. This allows to have an adaptation of the magnetic force during the assembly.

The aim of this section is to give the specifications of the PMTB, its design, its assembly and some experimental characterizations.

4.2.1 Specifications

The PMTB is designed to relieve the rotor mass of the electrical machine corresponding to an axial force of $F_z = 9.32\,kN$. For mechanical reasons, the minimum admissible airgap thickness is equal to $g = 1\,mm$. Furthermore to avoid PM rings with too small sections, an additional constraint is imposed during the optimization process: the height and the width of the PM rings section have to remain greater or equal to 5 mm. The same optimization process is used than the one presented in chapter 1 with this additional constraint on the PM dimensions.

In practice, a pre-load needs to be maintained on the ball bearings of the electrical machine for good operation. Therefore the operating axial force generated by the PMTB is equal to $6.18\,kN$ corresponding to 66.3% of the rotor mass.

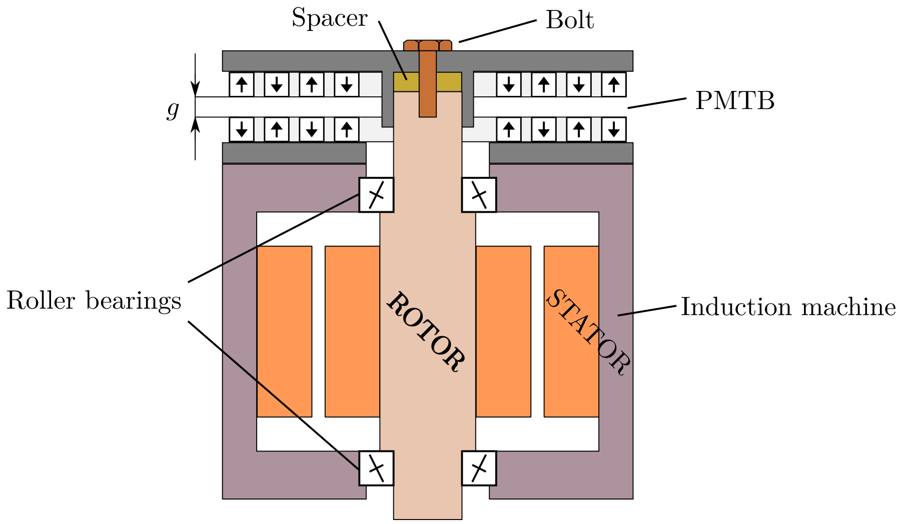

Figure 4.9: PMTB on a vertical shaft electrical machine. The rotating part of the PMTB is fixed on the shaft by the bolt. A spacer is used to adapt the airgap thickness.

4.2.2 Design

The design of a PMTB is a trade-off between the magnetic performance and mechanical constraints. The method proposed in this thesis consists to first find the optimal PM dimensions corresponding to the specifications and then, to slightly adapt the design, mainly the back-iron structure, to increase the mechanical resistance and to help the manipulations during the assembly.

At the end of the first phase, the specifications and the optimization process lead to the PM dimensions given in Table 4.1 for a number of rings $N = 4$. The PM material corresponds to a neodymium iron boron $NdFeB$ material (N35 grade).

Table 4.1: Dimensions and properties of the PM rings (N35).

	Parameters	Value
w	PM width	$7.1\,mm$
h	PM height	$5\,mm$
ζ	Space between the rings	$1.5\,mm$
R_{int}	Internal radius	$155.4\,mm$
N	Number of rings	4
B_r	Remanence	$1.17\,T$
$\mu_{r_{PM}}$	PM relative permeability	1.015

To respect these dimensions, the PM rings can not be made in one piece but have to be segmented. The segments are arc-shaped segments and this allows to have low torque/force ripple and low magnetic losses. The rings are segmented in 18 segments of 20°. The dimensions of the PM ring segments are summarized in Table 4.2. To protect the $NdFeB$ magnet against corrosion, the PM are nickel coated ($\geq 0.01 mm$ Ni+Cu+Ni).

Table 4.2: Dimensions of PM ring segments for the electrical machine PMTB.

Angle $\alpha\,[°]$	Height $h\,[mm]$	Internal radius $R_{int}\,[mm]$	External radius $R_{ext}\,[mm]$
20	5.0	155.4	162.5
20	5.0	164.0	171.1
20	5.0	172.6	179.7
20	5.0	181.2	188.3

The back-iron (BI) structures are constituted of ferromagnetic material e.g. structural steel S235. The dimensions of the back-iron support are given in Fig. 4.10. Circular grooves of $1\,mm$ deep are made in the iron piece to guide and place correctly the PM segments during the assembly. A mechanical clearance of $0.3\,mm$ on the external radius of each groove is made for a good adaptation to PM tolerances. Additionally, iron rims are placed on the edge of the back-iron structure. The impact of the grooves and the iron rim are discussed and the results are summarized in Table 4.3.

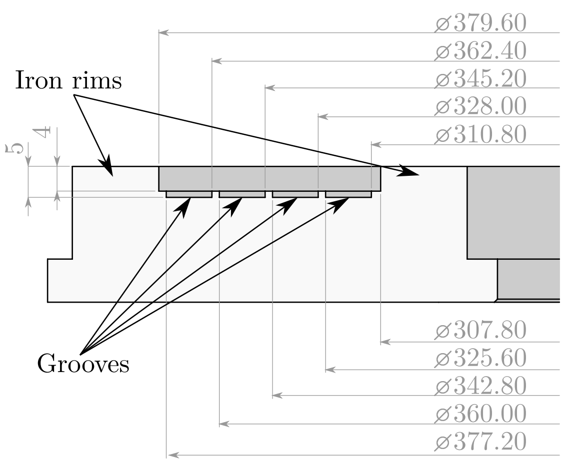

Figure 4.10: Local sectional view of the back-iron support with the main dimensions.

It is observed that the grooves decrease the magnetic force because they tend to short-circuit the magnetic field between the PM rings. This diminution is negligible (<1%) but is strongly dependent on the depth of the grooves. Figure 4.11 shows the evolution of the axial force with the relative depth of the grooves. The latter is therefore a trade-off between manufacturing / assembly complexity and good magnetic performance. In our case, the grooves have a depth of $1\,mm$ corresponding to 20% of the PM height. Table 4.3 shows also the influence of the iron rims. The latter increases the performance of around 5%.

Table 4.3: Impact of the grooves and iron rims on the axial force.

	Axial force F_z $[kN]$	In %
Grooves and rims	9.62	100
Rims (no groove)	9.70	100.8
Grooves (no rim)	9.18	95.4
Nothing (only BI)	9.27	96.3

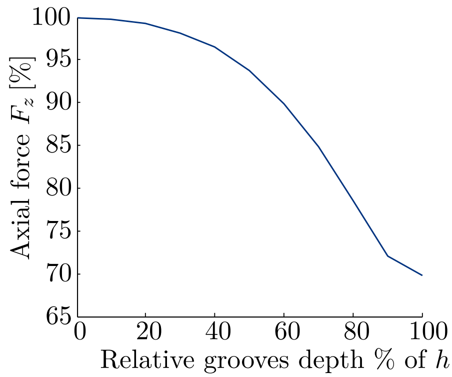

Figure 4.11: Impact of the relative grooves depth in % of the PM height h on the axial force F_z expressed in % with $F_{z,100\%} = 9.70\,kN$ corresponding to the case without groove, for an airgap thickness of $g = 1\,mm$.

From an mechanical point of view, the grooves and the iron rims support the PM ring segments during rotation. In addition, an epoxy resin is added between the PM rings to increase the rigidity and to decrease the stresses during operation.

4.2.3 Assembly

The assembly of the PMTB is illustrated in Fig. 4.12. During the assembly, the polarity of each PM segment is checked with a reference PM. The segments are placed on the iron piece by means of non magnetic tools. Shocks between PM segments and the iron piece need to be avoided due to the fragile characteristic of PM. Despite the risks of breakage due to shocks, the iron structure provides an assistance in the assembly. Indeed once they are placed, the PM segments remain at the correct position and are stable. The assembly is made ring by ring from inside to outside. In addition, an epoxy resin is injected between the PM rings with a syringe as shown in Fig 4.13. For a good repartition, the overflow of epoxy is scraped with a rubber piece.

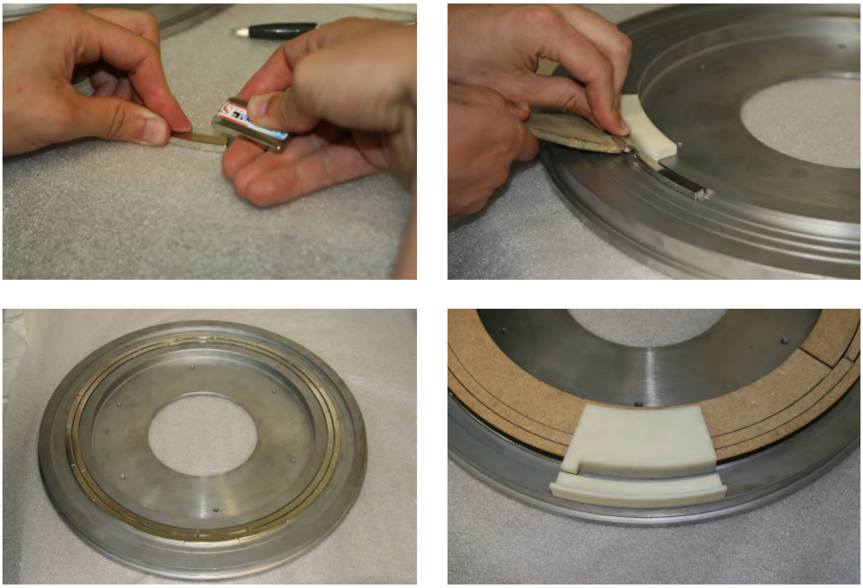

Figure 4.12: Assembly of the PM ring segments on the back-iron support.

Figure 4.13: Injection of epoxy between the PM rings.

4.2.4 Experimental characterization

In order to characterize the produced PMTB, different tests are performed first on a test bench and next directly on the electrical machine.

Characterization on test bench

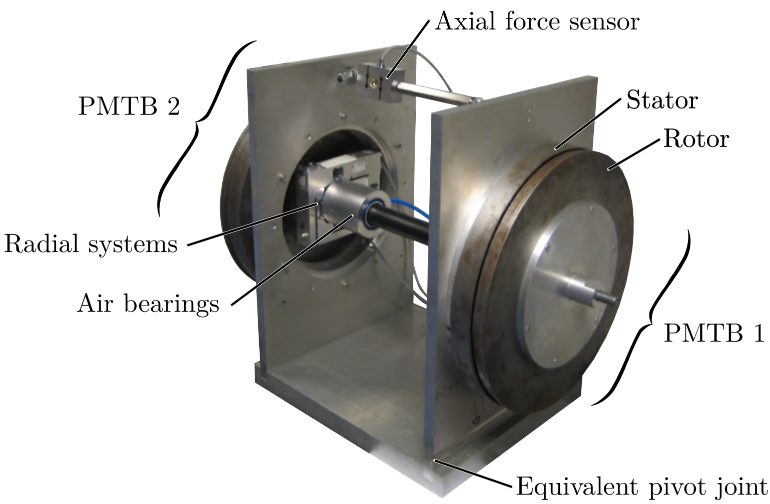

Figure 4.14: The test bench with two opposite PMTB on the same horizontal shaft. It allows to measure the axial and radial force for different axial and radial position.

The test bench is shown in Fig.4.14. It consist in two PMTB placed in opposite direction on the same horizontal shaft as shown in Fig. 4.15. This allows to get rid of heavy an cumbersome weights. The shaft is radially guided by two journal air bearings and axially free of movement at its both ends. The airgap thickness of both PMTB can be adapted by screwing or unscrewing the rotating part of the PMTB on the shaft. The air bearings are each connected to a "Radial system". This system allows for both measuring the radial force and for imposing a radial displacement. Both "Radial systems" are connected to static frames (in grey) clamped on the table. One of the two frames is weakened at its base and consequently, works as an equivalent pivot joint. A rod is placed on the top of the frames (in red) and is connected in series with an axial force sensor. The axial force measured is the force in the PMTB shaft. In order to evaluate the proportionality factor, a calibration of the axial sensor is needed. The "Radial system" are described in Fig. 4.16. They allow the measure of the radial forces while also imposing a radial displacement. They consist in 2 strain gauge force sensors placed in series as shown on Fig. 4.16.b and c. The displacement system is placed in series with the force sensors. It is made of a deformation piece as shown in Fig. 4.16.d. The deformation is imposed by pressure screws. The air bearing is clamped in the inner bore of the $\hat{e}_x$ and $\hat{e}_y$

displacement system.

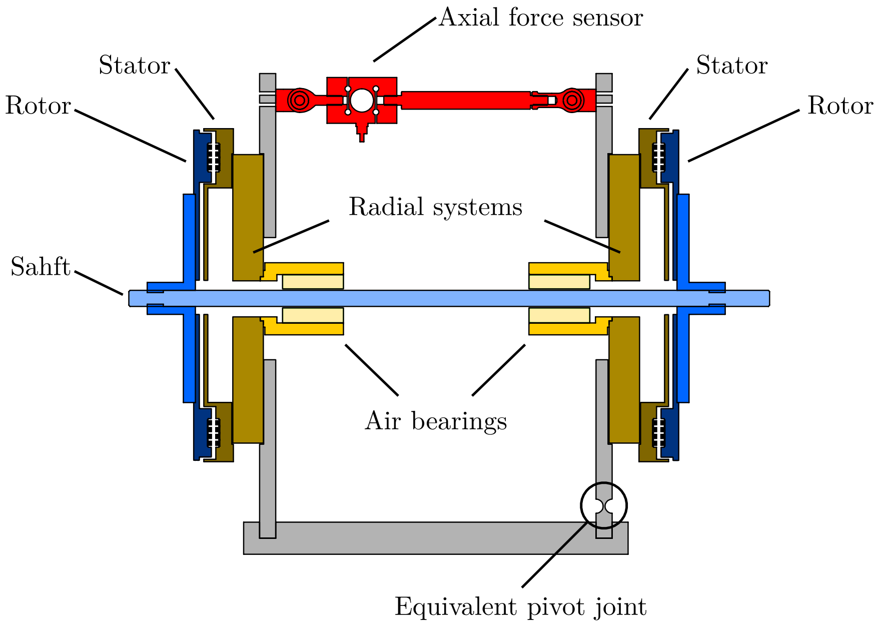

Figure 4.15: Two PMTB placed in opposite direction on the same shaft. The shaft is radially guided by the air bearings and axially free. The rotating parts of the PMTB are screwed on the shaft and their axial positions can be adapted. The axial force is measured by the combination of the equivalent pivot joint and the axial force sensor. The radial displacement and radial measurement are done by the "Radial system".

The calibration of the axial force measurement is done by placing the test bench in vertical position with only one PMTB. Different calibrated weights are placed on the shaft and the axial force. The results of the calibration are summarized in Fig. 4.17. The calibration was made two times. Small variations between the 2 calibrations are observed, and can be explained by manipulation of the test bench between the 2 calibrations. The proportionality constant gives $0.2036\,kg/N$. Considering the mean value of this proportionality constant gives an estimated error of less than 2%. The offset on the force/weight relation is due to mechanical constraint inside the test bench. When the test bench is in the horizontal shaft configuration, the y-intercept has not to be considered but the axial sensor needs to be tared without magnetic force.

During the test, undesirable problems appear. These problems are mainly due to undesired deformations of some parts of the test bench. These latter limit the maximal axial force to $3.5\,kN$.

The results obtained with this test bench are summarized in Fig 4.18 and Fig 4.19

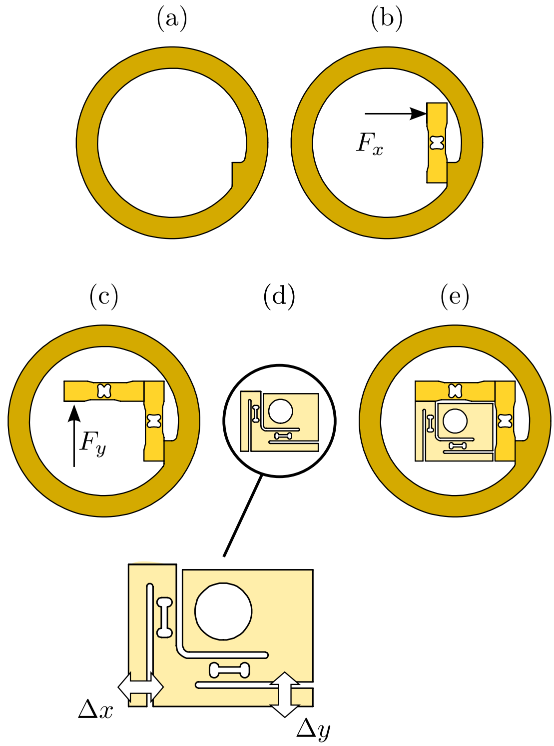

Figure 4.16: Description of the radial measurement and displacement system with (a): the static part ; (b)=(a) + the $\hat{e}_x$ force sensor ; (c)=(b) + the $\hat{e}_y$ force sensor ; (d): the $\hat{e}_x$ and $\hat{e}_y$ displacement system ; (e): the complete system.

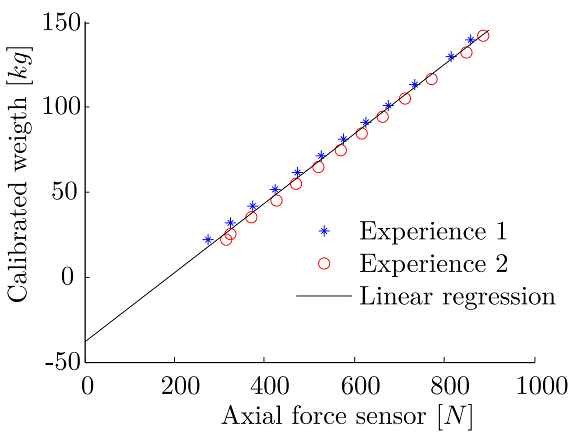

Figure 4.17: Calibration of the axial force sensor where the axial force is imposed by different calibrated weight.

for the axial force and radial force respectively. The experimental results are compared with finite element (FE) results. The FE model is a 2D axisymmetric magnetostatic model. It takes into account the relative permeability of the PM material, the ferromagnetic saturation and the exact shape of the ferromagnetic yoke i.e. grooves and rims as shown in Fig. 4.10.

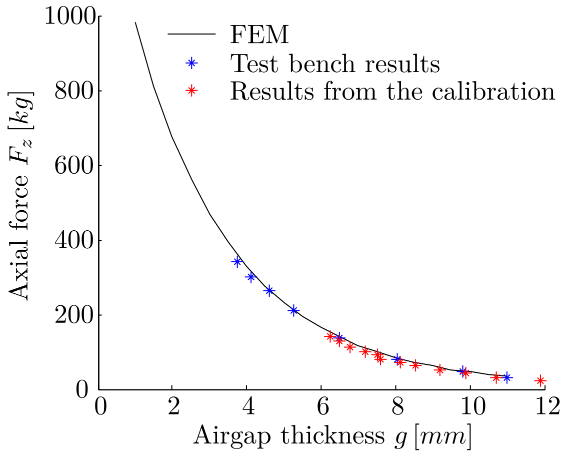

Figure 4.18: Evolution of the axial force F_z with the airgap thickness g when the static part and the rotating part of the PMTB are concentric.

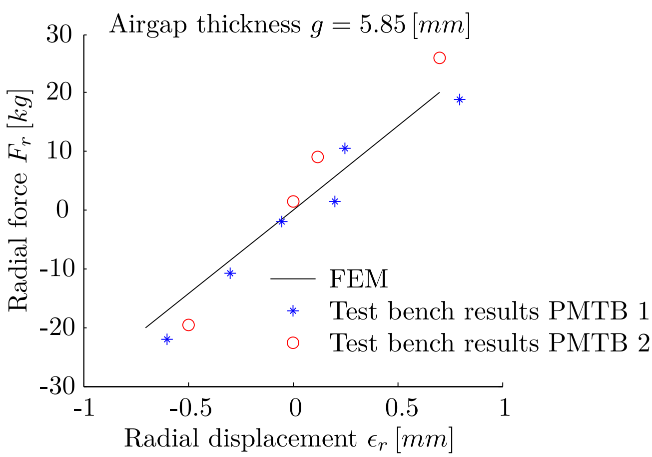

Figure 4.19: Evolution of the radial force with the radial displacement ϵ when the airgap thickness is $g = 5.85\,[mm]$.

Characterization on the electrical machine

The system used for measuring the force vs airgap characteristic of the PMTB is described in Fig. 4.20. The electrical machine is positioned vertically.

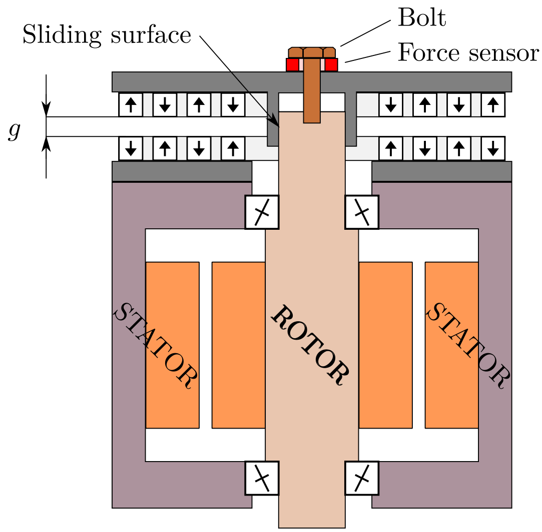

Figure 4.20: The magnetic axial force measurement system on the electrical machine. The force is measured by the annular load cell (in red). The airgap thickness g is adjusted by the bolt. The rotating part of the PMTB is guided on the sliding surface.

The axial position of the rotating part of the electrical machine is fixed by the ball bearings but its weight is supported by both the latter and the PMTB. By reducing the airgap thickness, the magnetic force increases. The axial position of the rotating part of the PMTB is imposed by tightening and loosening the bolt. The axial force is measured by a washer load cell. The rotating part of the PMTB slides along the cylindrical surface of the main shaft. The airgap thickness is measured manually with a calliper.

The results for the axial forces are given in Fig. 4.21. It shows very good agreement between the FE results and the experimental results.

4.3 Study case 2: Flywheel

A permanent magnet thrust bearing working as load reliever is designed for the flywheel. The guiding system i.e. the thrust and centering function is achieved by the ball bearings. The selected topology of PMTB is the radial stack with axial polarization and with back-iron structure as shown in Fig. 4.8.

As illustrated on Fig. 1.22, the PMTB is placed inside the vacuum enclosure in order to take full advantage of the (lower) surface of the flywheel to attach the rotating part of the PMTB.

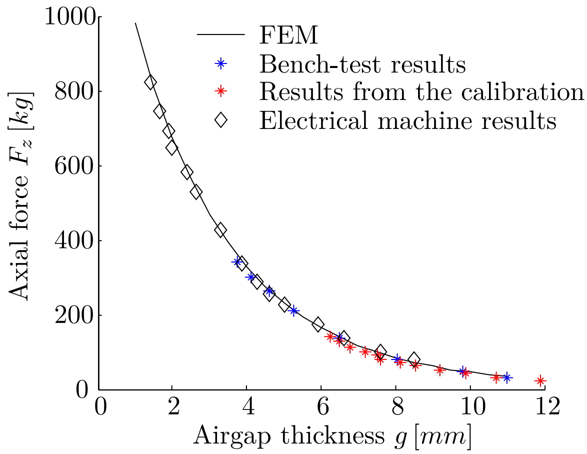

Figure 4.21: Evolution of the axial force F_z with the airgap thickness g when the static part and the rotating part of the PMTB are concentric.

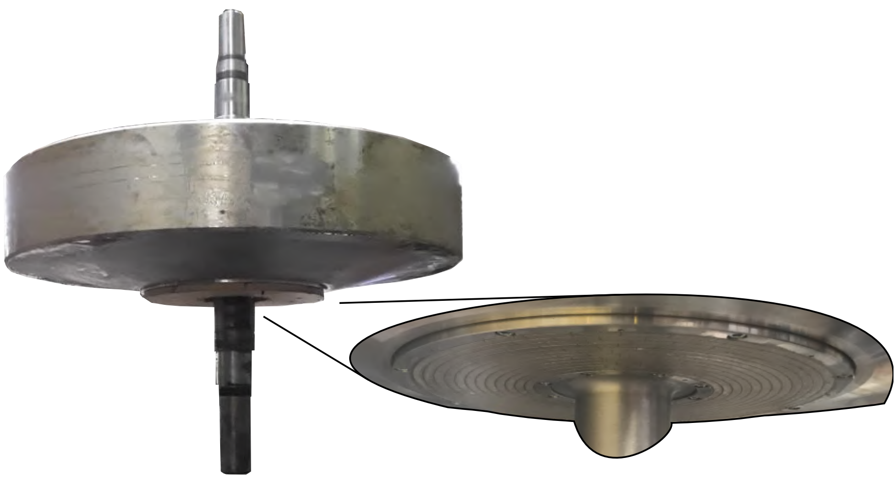

Figure 4.22: Rotating part of the PMTB placed on the flywheel system.

As shown by Kluyskens et al. [93], the operating temperature inside the flywheel housing can increase due to mechanical bearing losses and the windage losses. This has an impact on the PM properties and therefore on the PMTB performances as explained in Chapter 2. This influence needs to be considered in the design by considering passive compensation solution for load relieving application presented in Chapter 3.

4.3.1 Specifications

The PMTB is designed to relieve 100% of the flywheel weight $(52\,kN)$ even if the operating force is at 80%. For mechanical reasons, the minimum admissible airgap thickness is equal to $g = 1.6\,mm$. Furthermore to avoid PM rings to reach too large diameter values, an additional constraint is imposed on the optimization parameters. This constraint corresponds to force the maximum external diameter of the PM ring to be smaller or equal to $600\,mm$. The same optimization process is used than the one presented in chapter 1 with this additional constraint on the PM dimensions.

4.3.2 Design

These specifications lead to the dimensions of PM rings given in Table 4.4. The PM rings are segmented in 36 arc-shaped parts whose dimensions are given. The PM material considered for this applications is a samarium cobalt magnet $SmCo$. This choice is done because $SmCo$ magnet are more suitable for application with high temperature variation.

The ferromagnetic yoke/back-iron structure is similar to the one presented for the induction machine of section 4.2. It has grooves for the placement of PM segments. Internal and external iron rim are included. An epoxy resin is used to protect and strengthen the PM rings.

Table 4.4: Dimensions and properties of the PM rings Sm_2Co_{17} (YXG32)

	Parameters	Value
w	PM width	$12.3\,mm$
h	PM height	$6.3\,mm$
ζ	Space between the rings	$1.5\,mm$
R_{int}	Internal radius	$135.3\,mm$
R_{ext}	External radius	$300\,mm$
N	Number of rings	12
B_r	Remanence	$1.12\,T$
$\mu_{r_{PM}}$	PM relative permeability	1.05

Despite the use of $SmCo$ magnet, the magnetic force varies with the temperature as illustrated in Fig. 4.23. This result has been obtained by a 2D axisymmetric magnetostatic FE model. This latter takes into consideration the shape of the back-iron structure and also the demagnetization curve of the PM material and the variation of the PM properties with the temperature, as presented in chapter 2.

To compensate the temperature variation, the passive compensation solution presented in chapter 3 is used. This solution consists in placing pressurized bellows in series with the static part of the PMTB. In practice, 5 metal bellows are fixed on the back of the static part of the PMTB as shown in Fig. 4.24.

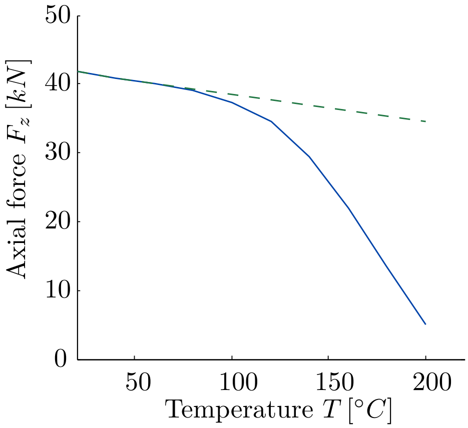

Figure 4.23: Evolution of the axial force with the temperature for an airgap thickness of $g = 2.3\,mm$. In dashed-line, the results without irreversible demagnetization.

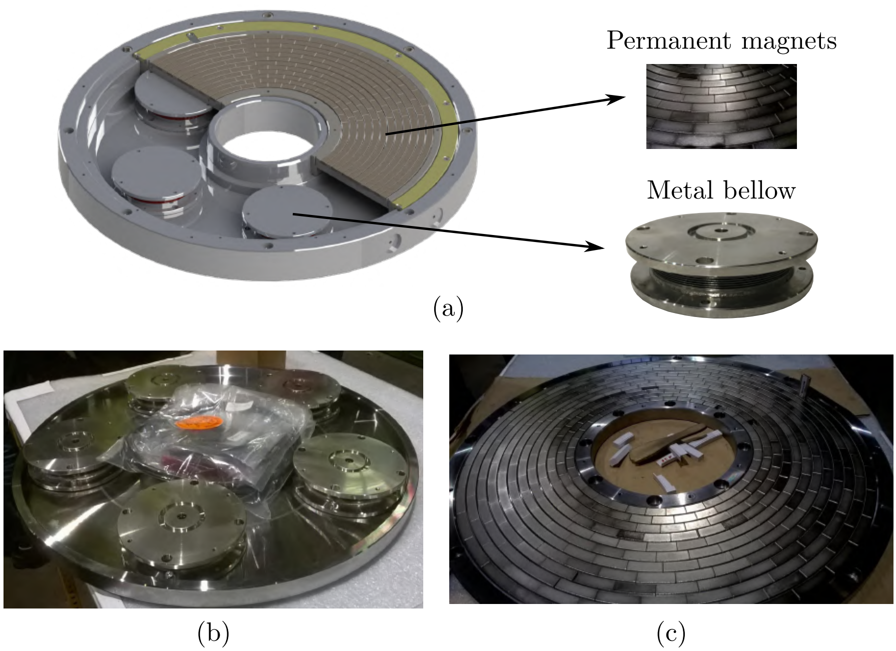

Figure 4.24: (a) Sectional view of the static part of the PMTB with 5 pressurized bellows. (b) The back of the static parts of the PMTB with the 5 pressurized bellows. (c) The static part of the PMTB with segmented PM rings.

Figure 4.25 shows a sectional view of the passive compensation system. The static part of the PMTB (in orange) can slide along a guiding surface. An upper and lower mechanical stop are considered to avoid too much deformation of the bellows and to avoid contact with the rotating part of the PMTB. The pressurized air is distributed between the bellows with the help of a groove in the casing and o-rings are used for sealing. An exploded view of the system is shown in Fig. 4.26.

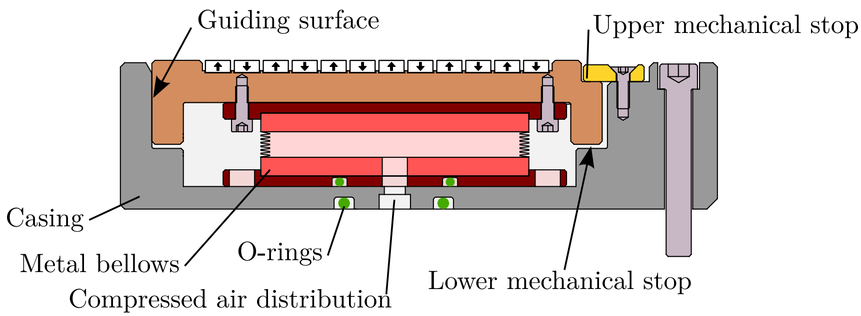

Figure 4.25: Local sectional view of the practical implantation of the compensation solution presented in chapter 3

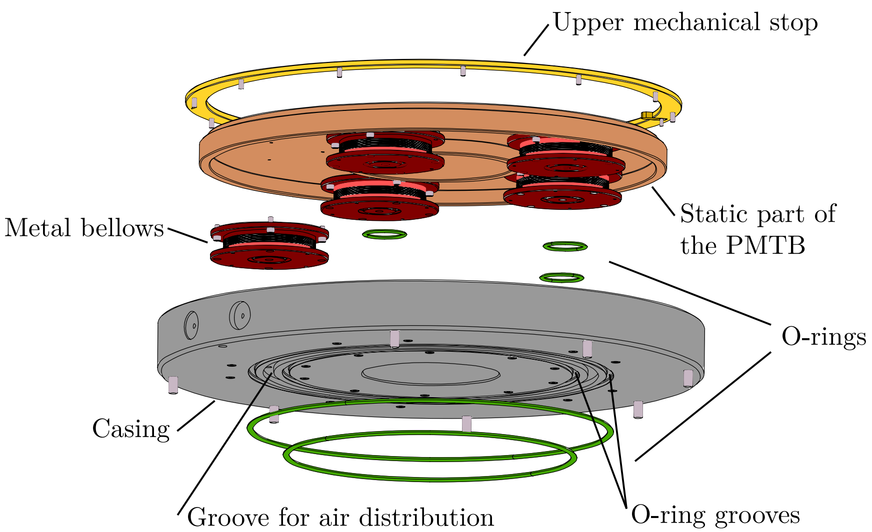

Figure 4.26: Exploded view of the practical implantation of the compensation solution presented in chapter 3.

As explained in chapter 3, the passive compensation system can be associated to an equivalent stiffness k_s. For good operation, this equivalent stiffness needs to be 10 times smaller than the stiffness of the PMTB. The latter is evaluated by numerical derivation of the force and is equal to $k_{PM} = 9.2\,kN/mm$.

As described in chapter 3, the equivalent stiffness of the passive compensation system is obtained by the combination of the structural stiffness k_{struct} linked to the bellows rigidity, the area stiffness k_a linked to the deformation of the effective area and the volumetric stiffness k_v linked to the variation of air volume. This stiffness is evaluated as follow for the particular implementation made of 5 metal bellows.

The structural stiffness of one corrugation of the bellow is equal to $0.76\,kN/mm$. This data is obtained from bellows manufacturer [114]. Five bellows are placed in parallel and seven corrugations are placed in series. The structural stiffness is then equal to $k_{struct} = \frac{5}{7} \times 0.76 = 0.54\,kN/mm$.

In the case of metal bellows, the area stiffness k_a is negligible because there is no deformation of the effective area.

The volumetric stiffness is obtained from (3.6). The effective area of one bellow is equal to $A_e = 128.7\,cm^2$. To carry the axial load of $41.6\,kN$, the pressure inside the bellows is evaluated by $p = \frac{41.6\,kN}{5 \times 128.7\,cm^2} = 6.46\,bar$[1]. The volume of air V is the sum of the volume of the air in the bellows and in the external tank V_{tank}. The volume of bellows is obtained by $V_{bellows} = 5A_e h_b$ with h_b the height of the bellows equal to $h_b = 12\,mm$. The variation of volume dV is proportional to the variation of the axial position: $dV = 5A_e dz$. The volumetric stiffness is obtained by:

$$\begin{aligned} k_v = 5 \times \frac{\gamma p A_e}{V}\frac{\partial V}{\partial z} &= \frac{25\gamma p A_e^2}{5A_e h_b + V_{tank}} \\ &= \underbrace{5\,\gamma p \frac{A_e}{h_b}}_{k_{1b}} \frac{1}{1 + \frac{V_{tank}}{V_{bellows}}} \end{aligned} \tag{4.1}$$

where k_{1b} is the volumetric stiffness of one bellow and γ the Poisson constant equal to 1.4 for air. As observed, the global volumetric stiffness is dependent on the ratio between the external tank volume and the bellows volume with $V_{bellows} = 0.77\,L$. Different external volumes are considered and the result is summarized in Table 4.5. As observed without external tank, the volumetric stiffness is not 10 times lower than the one of the PMTB $k_{PM} = 9.2\,kN/mm$. Nevertheless, a relative small external tank is required to respect this condition. For instance with an tank of $15.4\,L$, the volumetric stiffness k_v is worth $k_v = 0.24\,kN/mm$.

Table 4.5: Impact of the external tank volume on the volumetric stiffness.

Ratio $\frac{V_{tank}}{V_{bellows}}$ $[-]$	External tank volume V_{tank} $[L]$	Volumetric stiffness k_v $[kN/mm]$
0	0	4.86
1	0.77	2.42
10	7.7	0.45
20	15.4	0.24

[1]The pressure here is the absolute pressure because the flywheel system is placed in a vacuum enclosure.

In summary, the equivalent stiffness of the passive solution k_s is the sum of each contribution and is equal to $1.0\,kN/mm$. This value respects the condition for good passive compensation.

The impact of seasonal temperature variation on the air inside the tank needs also to be considered. This kind of variation can be associated to very "slow" phenomena. This means that if the fluid can be considered as an ideal gas, the pressure is directly dependent on the temperature by the ideal gas law:

$$p = \frac{n\,RT}{V} \tag{4.2}$$

with V the volume considered constant, n the number of moles of gas, R the ideal gas constant and T the temperature of the fluid. If the temperature is varying form its reference temperature $T = T_{ref} + \Delta T$, the magnetic force is varying:

$$\begin{aligned} F_z &= 5A_e p = 5A_e \frac{p_{ref}}{T_{ref}} T \\ &= 5A_e p_{ref} \left(1 + \frac{1}{T_{ref}} \Delta T\right) \end{aligned} \tag{4.3}$$

with the reference force $F_{z,ref} = 5A_e p_{ref}$. This evolution of the force with the temperature can be compared to the evolution of the magnetic force with the temperature due to the PM properties (2.6):

$$\begin{aligned} F_z &= F_{z,ref} \left(1 + \frac{100}{T_{ref}} \frac{\Delta T}{100}\right) \\ &\approx F_{z,ref} \left(1 - 2\,\alpha \frac{\Delta T}{100}\right) \end{aligned} \tag{4.4}$$

with T_{ref} expressed in Kelvin (K) and α the equivalent of the remanence temperature coefficient. By identification, this coeficient is obtained:

$$\alpha = -\frac{100}{2T_{ref}} \tag{4.5}$$

For a reference temperature of $T_{ref} = 20\,°C = 293.15\,K$, this coefficient is equal to $\alpha = -0.17\,\%/°C$ and can be compared to the remanence coefficient of neodymium and samarium magnet of $0.11\,\%/°C$ and $0.04\,\%/°C$ respectively (see chapter 2).

From this result, it can be observed that a seasonal temperature change, will impact the axial force inside the compensation system by increasing the axial force of 0.17%, while it will impact the axial force inside PMTB by decreasing the axial force of 0.04%. Therefore during the design process, it is important to compare the seasonal temperature variation to the variation of the operating temperature inside the enclosure. Otherwise, some solutions need to be considered in order to maintain a quasi-constant pressure.

4.3.3 Experimental characterization

The evolution of the axial force with the airgap thickness obtained at room temperature are given in Fig. 4.27. The solid line shows the results from the finite element model. The points ($\diamond$) shows the results from experimental measurement on the system. The position of the rotor is measured by a linear variable differential transformer (LVDT) placed in the bellows casing. The axial force is deduced from the pressure in the bellows[2] which is measured with a manometer.

We observe that distance between the upper and lower mechanical stop corresponds to their expected values of $2\,mm$. Nevertheless, the absolute value of the airgap, deduced from the linear position sensor is not precisely because of the fabrication tolerances and the assembly process. By matching the mechanical stop values to their theoretical values i.e., corresponding to an airgap thickness of $1.6\,mm$ and $3.6\,mm$, we observed in Fig. 4.27 that the FE results fit correctly with the experimental results.

Unfortunately, the passive solution has not been tested during operation due to a breakage of the flywheel probably caused by a wrong mounting of the ball bearing system.

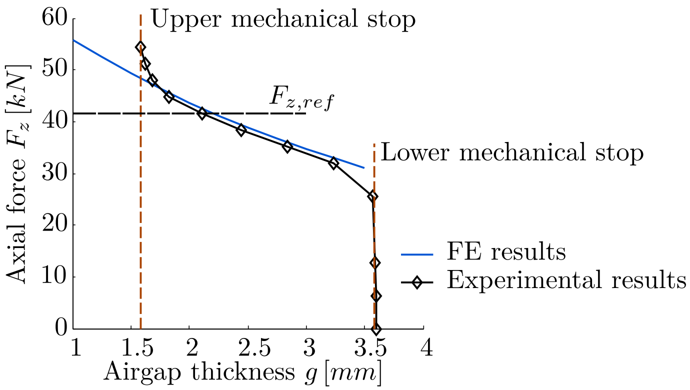

Figure 4.27: Evolution of the axial force with the airgap thickness at room temperature $20°C$. During the experiment, the axial force is controlled by adapting the pressure in the bellows. Solid line: FE results ; Points: experimental results ; Dashed-line: upper and lower mechanical stop.

The combination of the PMTB and the compensation system is however poorly sized. Indeed, the intended magnetic force is supposed to be $F_{z,ref} = 41.6\,kN$.

[2]The magnetic force is actually a combination of the force linked to the pressure inside the bellows and the force linked to the equivalent stiffness k_s. By considering that the bellows is deformed at its maximum of around $\Delta z = 2\,mm$, the contribution of the equivalent stiffness can be neglected: $k_s\,\Delta z = 2.0\,kN \ll 42\,kN$.

At room temperature $20°C$, this force corresponds to an airgap thickness of $2.1\,mm$. The compensation system is consequently only able to compensate the degradation of PM properties for an airgap thickness variation of $0.5\,mm$. This problem comes from a reduction of the value of the upper mechanical stop initially intended to be equal to $1\,mm$. This problem could be solved either by increasing the PM volume and therefore allow to reach the intended force $F_{z,ref}$ for a bigger airgap thickness e.g., $3\,mm$; or by admitting a smaller value of the upper mechanical stop.

Nevertheless, we can conclude from these results that the practical implementation of the passive compensation gives optimistic perspectives. The results show that adapting the pressure inside the bellows, changes the airgap thickness and therefore the magnetic force.

4.4 Conclusion

Two permanent magnet thrust bearings (PMTB) working as load relievers are built and combined with ball bearings. These PMTB have a radially stacked topology with axial polarization and with back-iron. The PM rings are made of arc-shaped segments. The back-iron structures include grooves, to help for the placement of the PM segments, and iron rims to increase the performance. Additionally, epoxy is placed between the PM rings. The combination of epoxy, grooves and iron rims increases the rigidity in order to hold the PM segments in place and to decrease the stresses during rotation.

One PMTB has been designed for an electrical machine with a magnetic force of $6.18\,kN$ for an airgap thickness of $2.1\,mm$. The PMTB has been characterized on a test bench and directly on the electrical machine. The magnetic force on the electrical machine can be adapted during the mounting with the help of mechanical spacer. The experimental results show very good agreement with the expected values of the finite element model.

The other PMTB has been designed for the flywheel with a magnetic force of $41.6\,kN$ for an airgap thickness of of $2.2\,mm$. Due to temperature variation inside the flywheel enclosure, the passive compensation system presented in Chapter 3 has been implemented.

Conclusion

Content overview

This thesis focuses on the design of permanent magnet thrust bearing (PMTB) for high axially loaded application and more explicitly for low-speed flywheel system. Specifically, the PMTB are combined with mechanical bearings in order to relieve the axial load on the mechanical bearings. This leads to two main advantages: the total losses are reduced and the lifetime of the system is increased. This concept can be extended to other applications with high axial load e.g., in hydroelectric turbine or in vertical axis wind turbine.

The first chapter compares PMTB topologies. In accordance with observation from the literature, the Halbach arrays are the best solution for topologies without iron. Nevertheless, the addition of back-iron allows for classical topologies to equal or even to out-perform Halbach-arrays. Induced-pole topologies give interesting performances.

The first chapter also presents a fast design procedure that allows to size optimal and realizable PMTB for practical applications. This procedure is well suited for application where a large area in the structure can be allocated to the PMTB e.g., in flywheel system. It does not allow to design PMTB that needs to be maintained in a controlled volume with imposed overall dimensions like for instance, to replace mechanical bearing in existing device. Nevertheless, the procedure gives quickly a first estimation of the minimal amount of PM volume and the corresponding dimensions of the PM rings.

The design procedure includes scaling laws that gives optimal dimensions that minimize the permanent magnet (PM) volume to generate a given axial load for an imposed airgap thickness and magnetic remanence. In order to limit the number of superposed PM rings, correction functions adapt these dimensions that allow to have the minimum PM volume for a given number of rings. At this stage, the dimensions of the PMTB can be quite complicated for the realization. A second set of correction functions can be used to design more realizable PMTB.

It has been proved than the precision of the correction functions is good enough, however they are not physics based and are selected to fit numerically with precalculated values. Therefore, they are validated only for a range of values. A more advanced study could be made with the aim to generalize this principle. The range of values considered is, however, quite sufficient for applications with a high axial load as considered in this study.

The second chapter compares permanent magnet materials that can be used in PMTB. This comparison is based on their ability to withstand demagnetization and temperature effects. To this end, a model that considers these effects is adapted from the electrical machine literature. The model is also validated experimentally.

The comparison shows that alnico magnets are not really suited for PMTB as their working point is in the irreversible demagnetization region. Their main advantage is their stability with temperature variations. Ferrite magnets give bad performance in term of force density due to their low energy density. However, their advantages are low price and a good resistance to demagnetization. The drawback is bad stability with the temperature variations. Samarium cobalt magnets have very good resistance to irreversible demagnetization risk ans are stable with temperature variation. Neodymium iron boron magnets have the highest force density. They are declined in different grades and the selection of this grade is clearly dependent on the application, on the selected topology and on the operating temperature. A bad selection can lead to irreversible demagnetization of the PM material and at the end, to decrease the PMTB performance. The neodymium magnet with grain boundary diffusion process, seems to give quite promising performances in terms of force density, demagnetization resistance and temperature stability.

All these remarks are in accordance with observations available in the literature or on PM manufacturers website. Nevertheless, the chapter highlights that the prediction of irreversible demagnetization risk is not easy and deserves more attention. In this aim, some design tips are proposed based on dimensionless quantity that allows to compare a PM material at its operating temperature, to the selected topology in the optimal configuration.

From this principle, it is highlighted that the Halbach arrays are the topologies the most sensitive to demagnetization risk and in opposite, classical polarization topologies better resit to demagnetization. Additionally, the use of back-iron structure reduces this risk for classical topologies.

These observations give only a starting point in the detection of demagnetization risk as they are obtained for PMTB in their optimal dimensions. The validity is not verified for non-optimal PMTB but this could be easily done by following the proposed methodology.

The third chapter introduces a passive compensation solution that maintains a quasi-constant magnetic force even if the PM performances are degraded. This degradation can be due to PM aging or to temperature variation. The solution is based on placing a pressurized jack in series with the static part of the PMTB. By this means, the magnetic force is directly dependent on the pressure inside the jack. Therefore, the magnetic force can be adjusted by the setting of the pressure. If this pressure is maintained constant or quasi-constant, the magnetic force is too. The main problem of this solution is therefore to maintain a constant pressure inside the jack even if this jack undergoes axial displacement. This can be achieved by connecting the jack to an external large fluid volume. However, this volume can be subject to temperature variation and alternative solution must be addressed.

In practice, the pressurized jack is a cumbersome solution and can be replaced by pressurized bellows. The latter present an equivalent stiffness that perturbs the compensation system. In order to maintain a good compensation, the equivalent stiffness of the bellows needs to be 10 times smaller than the equivalent stiffness of the PMTB.

The last chapter proposes two practical implementations of PMTB, one produced for the electrical machine that drives the flywheel, and the other one, for the flywheel. The selected topology is the radial stack with axial polarization and with back-iron. The PM rings are segmented in arc-shaped segments in order to reduce torque and force ripple, and Eddy current losses. This topology is chosen because it has the advantage of having:

- one of the best magnetic performance,
- an easy assembly of PM segments
- an easy global mounting.

The back-iron structures are machined to present grooves for the placing of the PM segments and iron rims to increase the magnetic performance. An epoxy resin is placed between the PM rings in order to increase the rigidity.

The electrical machine PMTB is characterized on a test bench and on the machine. The results show very good correspondence with the model predictions. The other PMTB is implemented with the passive compensation solution. The global system is characterized without rotation of the machine but first results show promising possibilities.

Original contributions

In summary, the main original contributions of this work are:

- Scaling laws and correction functions

  The literature presents dimensionless quantities called normalized force, that offers the advantage to compare and to size easily permanent magnet bearings. Based on this principle, this thesis proposes scaling laws able to design optimal permanent magnet thrust bearings (PMTB). In this optimal configuration, the PMTB are designed without constraint on the PM dimensions and with an ideal infinite superposition of PM rings. In order to design realisable PMTB, correction functions are derived in order to balance the non-idealities.

- Systematic comparison of PMTB topologies based on magnetic force density

  The literature proposed different comparison of PM bearings principally based on the radial stiffness density. Moreover, this comparison is most of the time made only for a few number of topologies and no systematic approach is followed. Based on the scaling laws derived in this thesis, a systematic comparison is performed allowing to classify on an objective basis the different topologies and allowing to study the impact of the ferromagnetic material.

- Prediction of the demagnetization risk based on dimensionless quantities

  Permanent magnet material placed inside the PMTB can be subject to reversible or irreversible demagnetization effects. These effects can be worsen by temperature increase. This thesis proposes to evaluate this risk based on dimensionless equivalent relative permeability and gives a simple methodology to evaluate these values.

- Passive compensation of the temperature or demagnetization effect

  The performance of the PMTB is dependent on the PM properties that can suffer from aging or temperature variation. In order to maintain a (quasi-) constant force, a passive compensation solution based on pressurized jack is presented. The latter is placed in series with the static part of the PMTB. By this means, the magnetic force is piloted by the pressure inside the jack and is maintained quasi-constant.

Broader considerations

The present work focuses on permanent magnet bearing working as axial load reliever i.e. on axial force generation. The methodology developed to compare topologies, to size optimal load reliever and to evaluate the risk of irreversible demagnetization, could be extended to centering and thrust permanent magnet bearings i.e. on the radial and axial stiffness respectively.

Moreover, the thesis aims to help designers making decision in order to integrate PMB in high axially loaded system. Based on the presented results, a more global optimization tool could be implemented. This tool could include for example:

- the comparison of the topologies,
- the comparison of the PM materials,
- the manufacturing and assembly issues.

Based on these different comparisons, the optimization algorithm could give directly the choice of topology and PM material as well as PM ring dimensions and the size of segments. Other aspects as the back-iron structure shapes, the mechanical resistance of the PM during operation or the need of axial stiffness could also be integrated.

The main advantage of this tool is that it gives directly the best solution for a given application. The drawback is that it does not allow a good understanding of the PMB behaviour with the different constraints.

The topic of this thesis is to introduce permanent magnet bearing in high axially loaded system as in flywheel systems. Its main function is to reduce the axial load on the mechanical bearing. Nevertheless, flywheel system presents other challenges that could be solved by a small adaptation of the PMTB.

One challenge is linked to maintain a vacuum environment inside the enclosure. If the whole system is not confined inside the enclosure e.g., the electrical machine or the mechanical bearings, rotating seals must be used. The latter increase the complexity of the device. One solution could consists in using ferrofluid seals in combination with the permanent magnet load reliever as shown in Fig. 4.28. Ferrofluid material is a liquid that becomes magnetized in presence of a magnetic field and has a natural tendency to locate itself where the magnetic field is the strongest. The superposition of PM rings can therefore be used as a superposition of small ferrofluid seals with a distribution of the retained pressure.

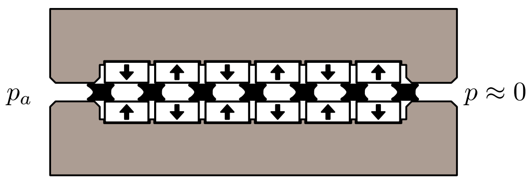

Figure 4.28: Principle of the ferrofluid seals. The ferrofluid material is in black and each layer supports a part of the pressure from the atmosphere to the vacuum.

The other challenge is linked to stability issues. Indeed as the flywheel system is subject to vibration phenomenon. In order to stabilize these vibration, a damping system needs to be introduced for example by placing visco-elastic material between the mechanical bearing and the enclosure. An other solution could consist in using Eddy current damper as shown in Fig. 4.29. The latter could be implemented by fasting a copper sheet on the non-rotating PM rings in front of the rotating one. The vibration of the rotating PM rings introduces Eddy currents in the copper sheet that generate magnetic damping.

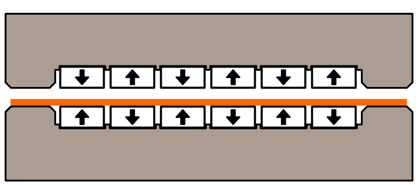

Figure 4.29: Principle of the eddy current damper. The copper sheet is in orange and Eddy currents are induced if their is vibration.

Bibliography

[1] McLarnon FR and Cairns EJ. Energy Storage. *Annual Review of Energy*, vol. 14, no. 1, 1989, pp. 241–271.

[2] Ibrahim H, Ilinca A and Perron J. Energy storage systems—Characteristics and comparisons. *Renewable and Sustainable Energy Reviews*, vol. 12, no. 5, 2008, pp. 1221–1250.

[3] Chen H, Cong TN, Yang W, Tan C, Li Y and Ding Y. Progress in electrical energy storage system: A critical review. *Progress in Natural Science*, vol. 19, no. 3, 2009, pp. 291–312.

[4] Luo X, Wang J, Dooner M and Clarke J. Overview of current development in electrical energy storage technologies and the application potential in power system operation. *Applied Energy*, vol. 137, 2015, pp. 511–536.

[5] IEC. *White Paper > Electrical Energy Storage*. 2010.

[6] Ragone DV. *Review of battery systems for electrically powered vehicles.* Tech. rep. SAE Technical Paper, 1968.

[7] Ribeiro PF, Johnson BK, Crow ML, Arsoy A and Liu Y. Energy storage systems for advanced power applications. *Proceedings of the IEEE*, vol. 89, no. 12, 2001, pp. 1744–1756.

[8] Christen T and Ohler C. Optimizing energy storage devices using Ragone plots. *Journal of Power Sources*, vol. 110, no. 1, 2002, pp. 107–116.

[9] Kousksou T, Bruel P, Jamil A, El Rhafiki T and Zeraouli Y. Energy storage: Applications and challenges. *Solar Energy Materials and Solar Cells*, vol. 120, 2014, pp. 59–80.

[10] Jiang Y, Liu J, Tian W, Shahidehpour M and Krishnamurthy M. Energy Harvesting for the Electrification of Railway Stations: Getting a charge from the regenerative braking of trains. A. *IEEE Electrification Magazine*, vol. 2, no. 3, 2014, pp. 39–48.

[11] Steeley W. Functional requirements for electric energy storage applications on the power system grid. *EPRI Technical Report 1022544*, 2011.

[12] Iglesias IJ, Martinez JC, Tobajas C, Lafoz M, Garcia-Tabarés LG and Vazquez C. “A kinetic energy storage system for railways applications”. *Proc. Eighth World Congress on Railway Research, Coex, Seoul, Korea.* 2008, pp. 18–22.

[13] Garcia-Tabares L, Iglesias J, Lafoz M, Martinez JC, Vazquez C, Tobajas C, Gomez-Alors A, Echeandia A, Lucas J and Zuazo C. “Development and testing of a 200 MJ/350 kW kinetic energy storage system for railways applications”. *Proceedings of the 9th World Congress on Railway Research, Lille, France.* 2011, pp. 22–26.

[14] Emadi A, Nasiri A and Bekiarov SB. *Uninterruptible Power Supplies and Active Filters | Ali Emadi, Abdolhosein Nasiri, Stoyan B. Bekiarov | download.* CRC Press LLC, 2005.

[15] Yamauchi Y, Uchiyama N, Suzuki E, Kubota M, Fujii M and Ohsaki H. “Development of 50kWh-class superconducting flywheel energy storage system”. *International Symposium on Power Electronics, Electrical Drives, Automation and Motion, 2006. SPEEDAM 2006.* IEEE, 2006, pp. 484–486.

[16] Tzeng J, Emerson R and Moy P. Composite flywheels for energy storage. *Composites Science and Technology*, Special Issue in Honour of Professor C.T. Sun vol. 66, no. 14, 2006, pp. 2520–2527.

[17] Pena-Alzola R, Sebastián R, Quesada J and Colmenar A. “Review of flywheel based energy storage systems”. *2011 International Conference on Power Engineering, Energy and Electrical Drives.* IEEE, 2011, pp. 1–6.

[18] Genta G. “Kinetic energy storage: An ideal application for magnetic bearings”. *Proceedings of the 14th International Symposium on Magnetic Bearings, Linz, Austria.* 2014, pp. 11–14.

[19] Earnshaw S. On the nature of the molecular forces which regulate the constitution of the luminiferous ether. *Trans. Camb. Phil. Soc*, vol. 7, 1842, pp. 97–112.

[20] Braunbek W. Freischwebende Körper im elektrischen und magnetischen Feld. *Zeitschrift für Physik*, vol. 112, no. 11-12, 1939, pp. 753–763.

[21] Braunbek W. Freies schweben diamagnetischer körper im magnetfeld. *Zeitschrift für Physik*, vol. 112, no. 11-12, 1939, pp. 764–769.

[22] Schaeffler. *Rolling bearings, Schaeffler catalogue.* 2014.

[23] SKF. *SKF spherical roller thrust bearings, catalogue.*

[24] Upadhyay RK, Kumaraswamidhas LA and Azam MS. Rolling element bearing failure analysis: A case study. *Case Studies in Engineering Failure Analysis*, vol. 1, no. 1, 2013, pp. 15–17.

[25] Williams T, Ribadeneira X, Billington S and Kurfess T. Rolling Element Bearing Diagnostics In Run-To-Failure Lifetime Testing. *Mechanical Systems and Signal Processing*, vol. 15, no. 5, 2001, pp. 979–993.

[26] Baiborodov YI, Tereshchenko AV, Aleksandrov AE, Shchetkin VS, Pokrovskii IB, Tukmakov VP and Gurbanov IS. Results of full-scale tests of the thrust bearing with elastic metal-plastic segments for the turbine-generator unit at the Bratsk hydroelectric station. *Hydrotechnical Construction*, vol. 16, no. 6, 1982, pp. 348–353.

[27] Iliev H. Failure analysis of hydro-generator thrust bearing. *Wear*, vol. 225-229, 1999, pp. 913–917.

[28] Liming Z, Yongyao L, Zhengwei W, Xin L and Yexiang X. A review on the large tilting pad thrust bearings in the hydropower units. *Renewable and Sustainable Energy Reviews*, vol. 69, 2017, pp. 1182–1198.

[29] Ferguson J. "GE hydro thrust bearings-applying development work to upgrading existing bearings". *Electric Machines and Drives, 1999. International Conference IEMD'99.* IEEE, 1999, pp. 809–811.

[30] Wang Q, Ma H, Cao S and Chen B. *Structure Optimal Design of Electromagnetic Levitation Load Reduction Device for Hydroturbine Generator Set.* Research article. 2015.

[31] Ma HZ, Wang B and Ju P. Design and modeling of hybrid magnetic levitation rotor weight support systems for hydraulic turbine generator units. *Journal of Hohai University: Natural Sciences*, vol. 38, no. 3, 2010, pp. 342–346.

[32] Pérez-Loya JJ, Abrahamsson CJD, Evestedt F and Lundin U. Performance Tests of a Permanent Magnet Thrust Bearing for a Hydropower Synchronous Generator Test-Rig. *Applied Computational Electromagnetics Society Journal*, vol. 32, no. 8, 2017.

[33] Kumbernuss J, Jian C, Wang J, Yang HX and Fu WN. A novel magnetic levitated bearing system for Vertical Axis Wind Turbines (VAWT). *Applied Energy*, Energy Solutions for a Sustainable World, Special Issue of International Conference of Applied Energy, ICA2010, April 21-23, 2010, Singapore vol. 90, no. 1, 2012, pp. 148–153.

[34] Premkumar T, Thangaraj M and Seralathan S. Design and Analysis of a Permanent Magnetic Bearing for Vertical Axis Small Wind Turbine. *Energy Procedia*, vol. 117, 2017, pp. 291–298.

[35] Yonnet J-P. Permanent magnet bearings and couplings. *IEEE Transactions on Magnetics*, vol. 17, no. 1, 1981, pp. 1169–1173.

[36] Delamare J, Rulliere E and Yonnet JP. Classification and synthesis of permanent magnet bearing configurations. *IEEE Transactions on Magnetics*, vol. 31, no. 6, 1995, pp. 4190–4192.

[37] Yonnet J-P, Lemarquand G, Hemmerlin S and Olivier-Rulliere E. Stacked structures of passive magnetic bearings. *Journal of Applied Physics*, vol. 70, no. 10, 1991, p. 6633.

[38] Halbach K. Design of permanent multipole magnets with oriented rare earth cobalt material. *Nuclear instruments and methods*, vol. 169, no. 1, 1980, pp. 1–10.

[39] Halbach K. Design of focussing and guide structures for charged particle beams using rare earth cobalt permanent magnets, 1981.

[40] Mansson D. On the optimization of Halbach arrays as energy storage media. *Progress in Electromagnetics Research B*, vol. 62, no. 1, 2015, pp. 277–288.

[41] Paden B, Groom N and Antaki JF. Design formulas for permanent-magnet bearings. *Journal of Mechanical Design*, vol. 125, no. 4, 2003, pp. 734–738.

[42] Moser R and Bleuler H. Optimization of repulsive passive magnetic bearings. *Magnetics, IEEE Transactions on*, vol. 42, no. 8, 2006, pp. 2038–2042.

[43] Lijesh K, Doddamani M, Bekinal S and Muzakkir S. Multi-objective optimization of stacked radial passive magnetic bearing. *Proceedings of the Institution of Mechanical Engineers, Part J: Journal of Engineering Tribology*, 2017, p. 1350650117733374.

[44] Lijesh KP, Doddamani M and Bekinal SI. A Pragmatic Optimization of Axial Stack-Radial Passive Magnetic Bearings. *Journal of Tribology*, vol. 140, no. 2, 2018, p. 021901.

[45] Bekinal SI, Anil TR, Jana S and Peerzade MI. Optimization of halbach magnetized permanent magnet axial bearing. *IJEIT*, vol. 2, no. 1, 2012, p. 5.

[46] Yoo S-Y, Kim W-Y, Kim S-J, Lee W-R, Bae Y-C and Noh M. Optimal design of non-contact thrust bearing using permanent magnet rings. *International Journal of Precision Engineering and Manufacturing*, vol. 12, no. 6, 2011, pp. 1009–1014.

[47] Lang M and Fremerey J. "Optimization of permanent-magnet bearings". *6th International Symposium on Magnetic Suspension Technology.* Politecnico di Turino, Turin, Italy, 2001.

[48] Marth E, Jungmayr G, Panholzer M and Amrhein W. "Optimization of stiffness per magnet volume ratio of discrete and continuous Halbach type permanent magnetic bearings". *13th international symposium on magnetic bearings (ISMB13).* 2012.

[49] Marth E, Jungmayr G and Amrhein W. A 2-D-Based Analytical Method for Calculating Permanent Magnetic Ring Bearings With Arbitrary Magnetization and Its Application to Optimal Bearing Design. *IEEE Transactions on Magnetics*, vol. 50, no. 5, 2014, pp. 1–8.

[50] Jungmayr G, Marth E, Amrhein W, Berroth H-J and Jeske F. Analytical stiffness calculation for permanent magnetic bearings with soft magnetic materials. *IEEE Transactions on Magnetics*, vol. 50, no. 8, 2014, pp. 1–8.

[51] Marth E, Jungmayr G, Panholzer M and Amrhein W. Optimization and realization of a multi-pole permanent magnetic bearing with rotating magnetization. *Proceedings of the Institution of Mechanical Engineers, Part I: Journal of Systems and Control Engineering*, vol. 230, no. 4, 2016, pp. 320–329.

[52] Safaeian R and Heydari H. Comprehensive comparison of different structures of passive permanent magnet bearings. *IET Electric Power Applications*, 2017.

[53] Yonnet J-P. Passive magnetic bearings with permanent magnets. *IEEE Transactions on Magnetics*, vol. 14, no. 5, 1978, pp. 803–805.

[54] Yang H, Zhao R-x and Yang S-y. New analytical solution for the analysis and design of permanent magnet thrust bearings. *Journal of Zhejiang University-SCIENCE A*, vol. 10, no. 8, 2009, pp. 1199–1204.

[55] Ravaud R, Lemarquand G and Lemarquand V. Halbach structures for permanent magnets bearings. *Progress In Electromagnetics Research M*, vol. 14, 2010, pp. 263–277.

[56] Sotelo GG, de Andrade Jr R and Ferreira AC. Magnetic bearing sets for a flywheel system. *IEEE Transactions on Applied Superconductivity*, vol. 17, no. 2, 2007, pp. 2150–2153.

[57] De Medeiros LH, Reyne G and Meunier G. Comparison of global force calculations on permanent magnets. *IEEE Transactions on magnetics*, vol. 34, no. 5, 1998, pp. 3560–3563.

[58] Ravaud R, Lemarquand G and Lemarquand V. Force and stiffness of passive magnetic bearings using permanent magnets. Part 1: Axial magnetization. *IEEE Transactions on Magnetics*, vol. 45, no. 7, 2009, pp. 2996–3002.

[59] ROBERT PLONSEY R. *PRINCIPLES AND APPLICATIONS OF Electromagnetic Fields*. 1961.

[60] Van Beneden M, Kluyskens V and Dehez B. Optimal sizing and comparison of permanent magnet thrust bearings. *IEEE Transactions on Magnetics*, vol. 53, no. 2, 2017, pp. 1–10.

[61] Van Beneden M, Kluyskens V and Dehez B. Comparison between optimized topologies of permanent magnet thrust bearings with back-iron. *Mechanical Engineering Journal*, vol. 4, no. 5, 2017, pp. 17–00061–17–00061.

[62] Constantinides S. “The demand for rare earth materials in permanent magnets”. *51st Annual Conference of Metallurgists*. 2012.

[63] Skokov KP and Gutfleisch O. Heavy rare earth free, free rare earth and rare earth free magnets - Vision and reality. *Scripta Materialia*, vol. 154, 2018, pp. 289–294.

[64] *Rare-earth Permanent magnet - VACOdym • VACOmax - VACUUM-SCHMELZE GmbH & Co. KG.*

[65] *Permanent magnet manufacturer*. HKCM Engineering e.K.

[66] *Product Catalogs and Literature*. Arnold Magnetic Technologies.

[67] Dobrzański LA, Drak M and Ziębowicz B. Materials with specific magnetic properties. *Journal of Achievements in Materials and Manufacturing Engineering*, vol. 17, no. 1-2, 2006, pp. 37–40.

[68] *Permanent Magnet Division | Arnold Magnetic Technologies.*

[69] *Magnet Materials Comparison Guide | Dura Magnetics USA.*

[70] Tumanski S. *Magnetic Materials*. Routledge Handbooks Online, 2011.

[71] Gutfleisch O, Willard MA, Brück E, Chen CH, Sankar SG and Liu JP. Magnetic materials and devices for the 21st century: stronger, lighter, and more energy efficient. *Advanced materials*, vol. 23, no. 7, 2011, pp. 821–842.

[72] Cui J, Kramer M, Zhou L, Liu F, Gabay A, Hadjipanayis G, Balasubramanian B and Sellmyer D. Current progress and future challenges in rare-earth-free permanent magnets. *Acta Materialia*, vol. 158, 2018, pp. 118–137.

[73] Hirota K, Nakamura H, Minowa T and Honshima M. Coercivity enhancement by the grain boundary diffusion process to Nd–Fe–B sintered magnets. *IEEE transactions on magnetics*, vol. 42, no. 10, 2006, pp. 2909–2911.

[74] Chen L, Hopkinson D, Wang J, Cockburn A, Sparkes M and O'Neill W. Reduced dysprosium permanent magnets and their applications in electric vehicle traction motors. *IEEE Transactions on Magnetics*, vol. 51, no. 11, 2015, pp. 1–4.

[75] Oono N, Sagawa M, Kasada R, Matsui H and Kimura A. Production of thick high-performance sintered neodymium magnets by grain boundary diffusion treatment with dysprosium–nickel–aluminum alloy. *Journal of Magnetism and Magnetic Materials*, vol. 323, no. 3, 2011, pp. 297–300.

[76] Weickhmann M, Katter M and Schleede B. "Nd-Fe-B permanent magnets for passive and hybrid magnetic bearings with extended application temperature range". *14th international symposium on magnetic bearings (ISMB14)*. 2014.

[77] Pérez-Loya JJ and Lundin U. Optimization of force between cylindrical permanent magnets. *IEEE Magnetics Letters*, vol. 5, 2014, pp. 1–4.

[78] Chen M, Chau KT, Li W and Liu C. Cost-effectiveness comparison of coaxial magnetic gears with different magnet materials. *IEEE transactions on magnetics*, vol. 50, no. 2, 2014, pp. 821–824.

[79] Sjökvist S and Eriksson S. Study of demagnetization risk for a 12 kW direct driven permanent magnet synchronous generator for wind power. *Energy Science & Engineering*, vol. 1, no. 3, 2013, pp. 128–134.

[80] Ruoho S and Arkkio A. Partial demagnetization of permanent magnets in electrical machines caused by an inclined field. *IEEE Transactions on Magnetics*, vol. 44, no. 7, 2008, pp. 1773–1778.

[81] Katter M. Angular dependence of the demagnetization stability of sintered Nd-Fe-B magnets. *IEEE Transactions on magnetics*, vol. 41, no. 10, 2005, pp. 3853–3855.

[82] Ruoho S, Dlala E and Arkkio A. Comparison of demagnetization models for finite-element analysis of permanent-magnet synchronous machines. *IEEE Transactions on Magnetics*, vol. 43, no. 11, 2007, pp. 3964–3968.

[83] Zhou P, Lin D, Xiao Y, Lambert N and Rahman MA. Temperature-dependent demagnetization model of permanent magnets for finite element analysis. *IEEE Transactions on Magnetics*, vol. 48, no. 2, 2012, pp. 1031–1034.

[84] Chavanne J, Chubar O, Elleaume P and Van Vaerenbergh P. “Nonlinear numerical simulation of permanent magnets”. *Proceedings of EPAC*. 2000, pp. 2316–2318.

[85] Calin M-D and Helerea E. “Temperature influence on magnetic characteristics of NdFeB permanent magnets”. *Advanced Topics in Electrical Engineering (ATEE), 2011 7th International Symposium on*. IEEE, 2011, pp. 1–6.

[86] Friebe J and Zacharias P. Review of Magnetic Material Degradation Characteristics for the Design of Premagnetized Inductors. *IEEE Transactions on Magnetics*, vol. 50, no. 3, 2014, pp. 40–48.

[87] Skomski R and Coey JMD. Magnetic anisotropy—How much is enough for a permanent magnet? *Scripta Materialia*, vol. 112, 2016, pp. 3–8.

[88] Van Beneden M, Kluyskens V and Dehez B. “Axial force evaluation in permanent magnet thrust bearings subject to demagnetization and temperature effects”. *16th international symposium on magnetic bearings (ISMB16)*. Beijing, China, 2018.

[89] Recheis M, Buchroithner A, Andrasec I, Gallien T, Schweighofer B, Bader M and Wegleiter H. “Improving kinetic energy storage for vehicles through the combination of rolling element and active magnetic bearings”. *Industrial Electronics Society, IECON 2013-39th Annual Conference of the IEEE*. IEEE, 2013, pp. 4641–4646.

[90] Toh CS and Chen SL. “Design and control of a ring-type flywheel battery system with hybrid halbach magnetic bearings”. *Advanced Intelligent Mechatronics (AIM), 2014 IEEE/ASME International Conference on*. IEEE, 2014, pp. 1558–1562.

[91] Jun Z, Dandan S, QiaoLi H, Shaolong L, Jinmei W, Guanghuai L and Di C. Multi objective optimization on suspension characteristics of vertical axis wind turbine. *International Journal of Applied Electromagnetics and Mechanics*, no. Preprint, 2018, pp. 1–11.

[92] Trekell HF, Mendelsohn LI and Wright JH. Magnetic suspension of the watt-hour meter rotor. *Transactions of the American Institute of Electrical Engineers*, vol. 67, no. 2, 1948, pp. 1180–1185.

[93] Kluyskens V, Van Beneden M and Dehez B. “Thermal model for a low-speed flywheel in low vacuum”. 2016.

[94] Haavisto M and Paju M. Temperature Stability and Flux Losses Over Time in Sintered Nd–Fe–B Permanent Magnets. *IEEE Transactions on Magnetics*, vol. 45, no. 12, 2009, pp. 5277–5280.

[95] Haavisto M, Kankaanpaa H and Paju M. Estimation of Time-Dependent Polarization Losses in Sintered Nd-Fe-B Permanent Magnets. *IEEE Transactions on Magnetics*, vol. 47, no. 1, 2011, pp. 170–174.

[96] Baermann M. “Temperature compensated permanent magnet bearing”. Pat. US3582162A. 1971.

[97] Keever J and Zisa W. “Temperature compensated magnetic bearing assembly for an induction meter”. Pat. US3810683A. 1974.

[98] Lipscomb GW. “Temperature compensated magnetic bearing system for a watthour meter”. Pat. US4196946A. 1980.

[99] Milligan JW. “Temperature-compensated magnetic bearings”. Pat. US 3657676A. 1972.

[100] Joseph LH. “Magnetic suspension bearing”. Pat. US3107948A. 1963.

[101] Hashish E and Lang NG. “Magnetic bearing apparatus and method for varying shaft thrust load support in induction motors and other rotating machinery”. Pat. US9225222B2. 2015.

[102] Docquier N, Fisette P and Jeanmart H. Multiphysic modelling of railway vehicles equipped with pneumatic suspensions. *Vehicle System Dynamics*, vol. 45, no. 6, 2007, pp. 505–524.

[103] Docquier N, Fisette P and Jeanmart H. Model-based evaluation of railway pneumatic suspensions. *Vehicle System Dynamics*, vol. 46, no. S1, 2008, pp. 481–493.

[104] Van Beneden M, Kluyskens V and Dehez B. “Passive compensation of the temperature effect on permanent magnet thrust bearing in hybrid system”. *16th international symposium on magnetic bearings (ISMB16)*. Beijing, China, 2018.

[105] Smith DJB, Mecrow BC, Atkinson GJ, Jack AG and Mehna AAA. “Shear stress concentrations in permanent magnet rotor sleeves”. *The XIX International Conference on Electrical Machines-ICEM 2010*. IEEE, 2010, pp. 1–6.

[106] Mystkowski A and Ambroziak L. Investigation of Passive Magnetic Bearing with Halbach-array. *Acta mechanica et automatica*, vol. 4, no. 4, 2010, pp. 78–82.

[107] Ohji T, Mukhopadhyay SC, Iwahara M and Yamada S. Performance of repulsive type magnetic bearing system under nonuniform magnetization of permanent magnet. *IEEE Transactions on Magnetics*, vol. 36, no. 5, 2000, pp. 3696–3698.

[108] Ohji T, Mukhopadhyay SC, Iwahara M and Yamada S. Permanent magnet bearings for horizontal-and vertical-shaft machines: A comparative study. *Journal of Applied Physics*, vol. 85, no. 8, 1999, pp. 4648–4650.

[109] Abrahamsson J. *Kinetic Energy Storage and Magnetic Bearings: for Vehicular Applications*. PhD Thesis. Acta Universitatis Upsaliensis, 2014.

[110] Hedlund M, Abrahamsson J, Pérez-Loya JJ, Lundin J and Bernhoff H. "Passive axial thrust bearing for a flywheel energy storage system". *The 1st Brazilian Workshop on Magnetic Bearings*. 2013.

[111] Pérez-Loya JJ, de Santiago J and Lundin U. "Construction of a Permanent Magnet Thrust Bearing for a Hydropower Generator Test Setup". *1st Brazilian Workshop on Magnetic Bearings, BWMB 2013*. 2013.

[112] Mukhopadhyay SC, Donaldson J, Sengupta G, Yamada S, Chakraborty C and Kacprzak D. Fabrication of a repulsive-type magnetic bearing using a novel arrangement of permanent magnets for vertical-rotor suspension. *IEEE transactions on magnetics*, vol. 39, no. 5, 2003, pp. 3220–3222.

[113] Siebert M, Ebihara B, Jansen R, Fusaro RL, Kascak A and Kenny A. "A passive magnetic bearing flywheel". *Intersociety Energy Conversion Engineering Conference*. Vol. 1. SAE; 1999, 2001, pp. 125–132.

[114] Witzenmann. *Brochures*. Manual of metal bellows. 2019.

A Correction function coefficient of the number of rings

Correction functions are used to take into account the influence of the number of rings on the optimal PM dimensions, such that:

$$\begin{aligned} h_{opt}^N &= h_{opt} f_h(N) \\ w_{opt}^N &= w_{opt} f_w(N) \\ \zeta_{opt}^N &= \zeta_{opt} f_\zeta(N) \\ L_{opt}^N &= L_{opt} f_L(N) \\ \Delta z_{opt}^N &= \Delta z_{opt} f_{\Delta z}(N) \end{aligned} \tag{A.1}$$

where h_{opt}^N, w_{opt}^N, ζ_{opt}^N, L_{opt}^N and Δz_{opt}^N are the optimal magnet dimensions for a given number of rings N and $f_h(N)$, $f_w(N)$, $f_\zeta(N)$, $f_L(N)$ and $f_{\Delta z}(N)$ are the corrections functions to take into account the influence of the number of rings:

$$f_i(N) = 1 + \alpha_i \frac{1}{N} + \beta_i \frac{1}{N^2}, \tag{A.2}$$

with $i = h$, w, ζ or L.

The value of the coefficient α_i and β_i are given in Table A.1 and A.2 for topology without iron and with back-iron respectively.

The optimal results for the case of an axial load $F_{z,ref} = 50\,kN$, an airgap thickness $g = 1\,mm$ and the remanence $Br = 1\,T$ are given in Table A.3 and A.3 for topology without iron and with back-iron respectively.

The coefficient for the axial offset are given in Table A.5.

Table A.1: Coefficients of the correction functions $f_i(N)$ for topology without iron.

	Axial stack				Radial stack			
	Ax	Rad	Perp	Hal	Ax	Rad	Perp	Hal
α_h	-0.0635	-0.0635	-0.1799	-0.3421	0.0530	0.0530	0.0278	0.0748
β_h	-0.0670	-0.0670	0.0139	1.1680	0.0106	0.0106	0.0282	0.1883
α_w	0.0282	0.0282	0.0512	0.0692	-0.1784	-0.1784	-0.0632	-0.1754
β_w	0.0278	0.0278	0.0189	0.0780	0.0070	0.0070	-0.0671	0.3846
α_ζ	-0.1583	-0.1583	0.0124	0	0.0121	0.0121	-0.1644	0
β_ζ	-0.3197	-0.3197	-0.2137	0	-0.2136	-0.2136	-0.3406	0
α_L	0.5160	0.5160	0.4191	1.3295	0.4150	0.4150	0.5165	0.7227
β_L	0.3419	0.3419	0.1472	0.4563	0.1649	0.1649	0.3413	0.4927
RMSE	0.1	0.1	0.3	1.9	0.3	0.3	0.1	2.4

Table A.2: Coefficients of the correction functions $f_i(N)$ for topology with back-iron.

	Axial stack				Radial stack			
	Ax	Rad	Perp	Hal	Ax	Rad	Perp	Hal
α_h	-0.0549	-0.0717	-0.1663	$h_{rad}: -0.1176$ $h_{ax}: -0.1331$	0.0883	0.1078	0.1924	-0.0478
β_h	-0.0824	-0.0762	0.0011	$h_{rad}: 0.1219$ $h_{ax}: -0.1331$	0.0730	0.0906	0.0214	-0.4499
α_w	0.0624	0.0411	0.0912	-0.3217	-0.1462	-0.1470	-0.0672	$w_{ax}: -0.3914$ $w_{rad}: 0.3619$
β_w	0.0852	0.0318	0.0427	-0.9501	-0.0314	-0.0289	-0.0646	$w_{ax}: 0.2904$ $w_{rad}: -1.8926$
α_ζ	-0.1460	-0.1841	0.0636	0	0.0945	0.1579	-0.0190	0
β_ζ	-0.2042	-0.2204	-0.2898	0	-0.5317	-0.6631	-0.5867	0
α_L	0.5378	0.5298	0.4280	0.7754	0.4571	0.4617	0.5063	0.4323
β_L	0.3073	0.3547	0.0846	0.8063	0.0987	0.0337	0.2685	1.1709
RMSE	0.05	0.07	0.12	1.85	0.13	0.22	0.29	1.03

Table A.3: Optimal result for topology without iron for $F_{z,ref} = 50\,kN$, $g = 1\,mm$ and $B_r = 1\,T$.

	Axial stack				Radial stack			
	Ax	Rad	Perp	Hal	Ax	Rad	Perp	Hal
$V_{opt}\,[dm^3]$	1.82	1.82	1.81	1.04	1.81	1.81	1.82	1.04
$h_{opt}\,[mm]$	2.26	2.26	2.46	1.60	1.27	1.27	1.26	1.26
$w_{opt}\,[mm]$	1.26	1.26	1.27	1.26	2.46	2.46	2.26	1.59
$\zeta_{opt}\,[mm]$	0.875	0.875	0.733	0	0.733	0.733	0.875	0
$L_{opt}\,[m]$	643.5	643.5	581.5	514.2	581.5	581.5	643.5	517.2

Table A.4: Optimal result for topology with back-iron for $F_{z,ref} = 50\,kN$, $g = 1\,mm$ and $B_r = 1\,T$.

	Axial stack				Radial stack			
	Ax.	Rad.	Perp.	Hal.	Ax.	Rad.	Perp.	Hal.
$V_{opt}\,[dm^3]$	2.60	0.92	1.93	0.95	1.07	2.60	2.00	1.00
$h_{opt}\,[mm]$	2.27	2.22	2.44	2.13^{rad} 0.87^{ax}	0.72	2.38	1.62	1.09
$w_{opt}\,[mm]$	2.33	0.64	1.54	0.90	2.10	2.41	2.21	2.19^{ax} 0.84^{rad}
$\zeta_{opt}\,[mm]$	0.86	0.86	0.74	0	0.66	0.75	0.84	0
$L_{opt}\,[mm]$	492	653	514	700	707	454	462	605

Table A.5: Coefficients of the correction functions $f_{\Delta z}(N)$ for topologies with axial stack.

	Polarization	$\alpha_{\Delta z}$	$\beta_{\Delta z}$	RMSE
Topology without iron	Ax.	-0.0451	0.0696	0.01
	Rad.	-0.0451	0.0696	0.01
	Hal.	-0.1509	-0.5362	0.06
Topology with back-iron	Ax.	-0.0545	0.1042	0.12
	Rad.	-0.0476	0.0791	0.08
	Hal.	-0.1234	0.1337	0.16

B Correction function coefficient of the limited PM length

Correction functions are used to take into account the influence of the limited PM length on the optimal PM dimensions, such that:

$$\begin{aligned} h_{opt}^{L} =& g_h\left(\frac{L}{L_{opt}}\right) \times h_{opt} \\ w_{opt}^{L} =& g_w\left(\frac{L}{L_{opt}}\right) \times w_{opt} \\ \zeta_{opt}^{L} =& g_\zeta\left(\frac{L}{L_{opt}}\right) \times \zeta_{opt}, \end{aligned} \tag{B.1}$$

where h_{opt}^{L}, w_{opt}^{L}, ζ_{opt}^{L} are the optimal dimensions of the PM for a limited total PM length L and $g_h\left(\frac{L}{L_{opt}}\right)$, $g_w\left(\frac{L}{L_{opt}}\right)$ and $g_\zeta\left(\frac{L}{L_{opt}}\right)$ are correction functions. This relation is approximated by non physic based functions:

$$g_i(x) = A_i + B_i x^{-0.5} + C_i x^{-0.75} + D_i x^{-1} \tag{B.2}$$

for i equal to h, w and ζ. The value of the constant coefficients A_i, B_i, C_i and D_i (with $i = h$, w, or ζ) are calculated by the same RMSE method than the one presented for the correction function for a limited number of ring.

The value of the coefficients and the RMSE are given in Table B.1, Table B.2, Table B.3 and Table B.4.

Table B.1: Coefficient of the correction function that limited the PM length for topologies without iron.

	Axial stack with polarization:			Radial stack with polarization:		
	Ax./Rad.	Perp.	Halb.	Ax./Rad.	Perp.	Hal.
A_h	0.2115	0.2132	0.3338	0.0446	0.0441	-0.0024
B_h	1.0994	0.8209	0.7579	0.9819	0.9831	0.9648
C_h	-0.6668	-0.2986	-0.3707	-0.3366	-0.3376	-0.3964
D_h	0.3559	0.2644	0.2790	0.3101	0.3104	0.4338
A_w	0.0168	0.0442	-0.0043	0.2126	0.2129	0.3325
B_w	1.1120	0.9826	0.9746	0.8227	0.8220	0.7570
C_w	-0.6691	-0.3370	-0.4119	-0.3003	-0.2995	-0.3663
D_w	0.5402	0.3102	0.4416	0.2649	0.2646	0.2770
A_ζ	0.7273	1.0108	0	1.0114	1.0119	0
B_ζ	0.1680	-0.0252	0	-0.0273	-0.0294	0
C_ζ	-0.0941	0.0193	0	0.0214	0.0236	0
D_ζ	0.1988	-0.0049	0	-0.0054	-0.0061	0
RMSE	0.2	0.5	0.3	0.5	0.4	0.4

Table B.2: Coefficient of the correction function that limited the PM length for axially stacked topologies with back-iron.

	Axial stack with polarization:				
	Ax.	Rad.	Perp.	Halb.	
				Axial direction	Radial direction
A_h	-0.2787	-0.7504	0.1304	-3.0959	5.8506
B_h	2.3452	4.7720	0.7814	13.4658	-20.4850
C_h	-1.8655	-4.5246	-0.2104	-13.0241	21.8265
D_h	0.8098	1.5190	0.2712	3.6558	-6.1491
A_w	0.6181	0.6589	0.1761	-1.2927	
B_w	-0.4018	-1.0506	0.8698	7.0868	
C_w	0.6115	1.4268	-0.3178	-7.7631	
D_w	0.1680	-0.0468	0.3030	2.9526	
A_ζ	-0.2787	-0.7504	0.1304	0	
B_ζ	2.3452	4.7720	0.7814	0	
C_ζ	-1.8655	-4.5246	-0.2104	0	
D_ζ	0.8098	1.5190	0.2712	0	
RMSE	0.24	0.23	0.14	0.84	

Table B.3: Coefficient of the correction function that limited the PM length for radially stacked topologies with back-iron.

	Axial stack with polarization: Ax.	Rad.	Perp.	Halb. Axial direction	Halb. Radial direction
A_h	0.1666	0.5649	0.0296	-0.5929	
B_h	0.6083	-0.2755	1.6983	3.1509	
C_h	-0.0287	0.6258	-1.4626	-2.7301	
D_h	0.2587	0.0849	0.7463	1.1724	
A_w	0.1470	-0.2986	0.2318	-1.5152	2.3005
B_w	1.0047	2.0992	0.6266	9.0352	-6.6591
C_w	-0.4238	-1.3570	-0.2149	-10.0164	7.6513
D_w	0.2698	0.5592	0.3467	3.5371	-2.3217
A_ζ	3.2666	2.7409	2.5123	0	
B_ζ	-7.1711	-4.9988	-5.0387	0	
C_ζ	6.7878	4.3301	5.0042	0	
D_ζ	-1.8267	-1.0906	-1.4362	0	
RMSE	0.12	0.13	0.31	0.92	

Table B.4: Coefficient of the correction function that limited the PM length for topologies with induced pole.

	Axial stack with axial polarization	Radial stack with radial polarization
A_h	-4.9402	0.6635
B_h	24.0405	-0.1145
C_h	-26.5951	0.3611
D_h	8.5062	0.1740
A_w	2.9557	-0.2367
B_w	-10.9938	1.5227
C_w	12.3345	-0.6910
D_w	-3.2903	0.3342
A_ζ	10.3724	3.8973
B_ζ	-39.4891	-7.8704
C_ζ	43.2919	6.7366
D_ζ	-13.2547	-1.6745
RMSE	0.80	0.24

Scaling laws of simpler topology

C

The topologies presented in Section 1.2 allows:

- for classical topology: to have a gap between the rings ζ,
- for Halbach array: to adapt the PM section in function of the polarization direction.

In order to evaluate the impact of these adaptations on optimal PMTB, the scaling laws of simpler topology, without these adaptations, are evaluated. The procedure is the same than the one presented in Section 1.4.

The objective function is to minimize the ratio of the PM volume on the axial force. The optimization parameters are the PM section height h and width w. The optimization is performed for an airgap thickness g of $2\,mm$ and a remanence B_r of $1\,T$. The optimization can be expressed:

$$\min_{h,w} \left(\frac{V}{F_z} \right) \Bigg|_{g=2\,mm, B_r=1\,T,\, N=\infty} \tag{C.1}$$

The ratio between the PM volume and the axial force is evaluated by a 2D plane FE model. The model profits of the anty-periodicity of the magnetic field and therefore corresponds to evaluate the force for topology with an infinite number of rings. The ratio $\frac{V}{F_z}$ is obtained for all the topologies:

$$\frac{V}{F_z} = \frac{2hw}{f_z} \tag{C.2}$$

Table 1.6 and Table 1.7 summarized the scaling law coefficients obtained by the optimization of each topology. The scaling law coefficients are derived by the optimization of only one set of airgap thickness $g = 2\,mm$ and remanence $B_r = 1\,T$ and for the number of rings $N = \infty$. The coefficient are deduced using (1.21), (1.23) and (1.25).

Comparing the values of Table C.2 of simpler topology with the value of Table 1.6 of adapted topology, allows to highlight the impact of the adaptation.

Table C.1: Scaling law coefficients $\hat{V}_{opt}$ of the optimal PM volume for topology without iron (WhoI), with back-iron (BI) and with induced pole (IP).

	Axial stack with polarization:				Radial stack with polarization:			
	Axial	Radial	Perp.	Hal.	Axial	Radial	Perp.	Hal.
	PM Volume $\hat{V}_{opt}$							
WhoI	16.92	16.92	15.98	8.24	15.95	15.95	16.88	8.22
BI	24.09	8.37	17.08	8.23	9.43	23.10	18.47	8.62

Table C.2: Scaling law coefficients of the optimal PM dimensions for the simpler topology without iron (WhoI) and with back-iron (BI).

	Axial stack with polarization:				Radial stack with polarization:			
	Axial	Radial	Perp.	Hal.	Axial	Radial	Perp.	Hal.
	PM section height $\hat{h}_{opt}$							
WhoI	3.01	3.00	3.39	1.58	1.29	1.29	1.23	1.26
BI	3.05	3.05	3.29	1.61	0.73	2.46	1.57	1.39
	PM section width $\hat{w}_{opt}$							
WhoI	1.23	1.23	1.30	1.27	3.36	3.36	2.99	1.58
BI	2.30	0.61	1.56	1.26	2.91	3.29	2.94	1.51
	Total length of PM rings $\hat{L}_{opt}$							
WhoI	4.56	4.59	3.61	4.08	3.67	3.68	4.59	4.14
BI	3.43	4.51	3.32	4.06	4.41	2.86	3.99	4.11

The comparison is based on the relative variation of PM volume inspired of comparison presented in Section 1.7:

$$\frac{\hat{V}_{opt,i}^{adapt} - \hat{V}_{opt,i}^{simpler}}{\hat{V}_{opt,i}^{adapt}} \, [\%] \tag{C.3}$$

with i the different presented topologies without iron and with back-iron. The results are summarized in Table C.3. It is observed that:

- for classical topologies, the gain is of 16% for topology with shift (see Section 1.5), and of 11.5% for topology without shift,
- for Halbach array, their is no gain for topology without iron as in this case, the optimal results do not adapt the section in function of the polarization direction, and is of 9% for Halbach array with back-iron.

Table C.3: Impact of the adaptation on the PMTB performance. The adaptation is for classical topology based on the gap between PM ζ ; and for Halbach array, based on the PM section adaptation in function of the polarization direction.

	Axial stack with polarization:				Radial stack with polarization:			
	Axial	Radial	Perp.	Hal.	Axial	Radial	Perp.	Hal.
	Relative gain in PM volume $\frac{\hat{V}_{opt,i}^{adapt} - \hat{V}_{opt,i}^{simpler}}{\hat{V}_{opt,i}^{adapt}}$ [%]							
WhoI	-16	-16	-11	0	-11	-11	-16	0
BI	-16	-16	-11	-9.5	-12	-11.5	-16	-9

Theory on series and parallel springs D

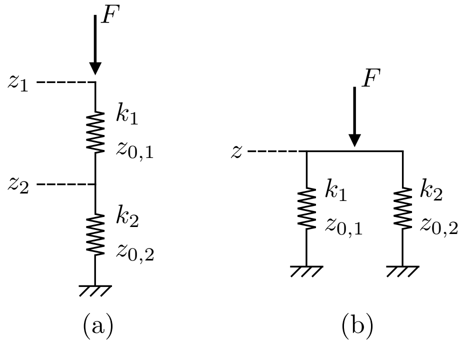

Figure D.1: (a) Two series springs, (b) Two parallel springs.

The equivalent model of two series springs (Fig. D.1.a) is:

$$F = \frac{k_1 k_2}{k_1 + k_2} \left(z_1 - \left(z_{0,1} + z_{0,2} \right) \right) \tag{D.1}$$

with the position of the middle point z_2:

$$z_2 = \frac{k_1}{k_1 + k_2} z_1 - \frac{k_1 z_{0,1} - k_2 z_{0,2}}{k_1 + k_2} \tag{D.2}$$

The equivalent model of two parallel springs (Fig. D.1.b) is:

$$F = -(k_1 + k_2) \left(z - \left(\frac{k_1 z_{0,1} + k_2 z_{0,2}}{k_1 + k_2} \right) \right) \tag{D.3}$$